PRINTED METALLISATION OF PHOSPHORUS DOPED SILICON SURFACES FOR SOLAR CELL APPLICATIONS

Vinodh SHANMUGAM

NATIONAL UNIVERSITY OF SINGAPORE

2016

PRINTED METALLISATION OF PHOSPHORUS DOPED SILICON SURFACES FOR SOLAR CELL APPLICATIONS

Vinodh SHANMUGAM

(*M.Sc., National University of Singapore,*
Singapore)

(*B.E., PSG College of Technology,*
Anna University, India)

A THESIS SUBMITTED

FOR THE DEGREE OF DOCTOR OF PHILOSOPHY

DEPARTMENT OF ELECTRICAL AND COMPUTER ENGINEERING

NATIONAL UNIVERSITY OF SINGAPORE

2016

DECLARATION

I hereby declare that the thesis is my original work and it has been written by me in its entirety. I have duly acknowledged all the sources of information which have been used in this thesis.

This thesis has also not been submitted for any degree in any university previously.

Vinodh SHANMUGAM

Date: 11th February 2016

எண்ணித் துணிக கருமம்; துணிந்தபின்
எண்ணுவம் என்பது இழுக்கு.
- திருவள்ளுவர் , 30 B.C.

(Pronunciation)
Ennith thunika karumam thunindhapin
ennuvam enpadhu izhukku

(Meaning)
Embark upon an action after careful thought.
It is foolishness to say, “let us begin the task now and think about it later”.
Thiruvalluvar, 30 B.C.

Acknowledgements

This PhD was made a reality due to the selfless support from many people. And I would like to show my gratitude and take this opportunity to thank several people and organisations who have helped me during this PhD candidature.

First and foremost, I am grateful to my supervisor Prof. Armin Gerhard ABERLE, for giving me the freedom and support to continue with my work and concurrently do my PhD studies at the Solar Energy Research Institute of Singapore (SERIS) at NUS. Despite being extremely busy, he has always managed to find time to give me all the guidance and support that I needed.

I am profoundly grateful to my co-supervisor, Dr. Thomas MUELLER for the unlimited support and advices he gave me through the past years. Thanks for showing and teaching me how to always stay calm, irrespective of the situation. Thank you Thomas, for giving me full freedom and for funding my research activities. I would like to acknowledge funding for the research provided by the National Research Foundation, Prime Minister's office, Singapore under its Clean Energy Research Programme (CERP Award No. NRF2010EWT-CERP001-022).

I would also like to thank my Masters (M.Sc.) supervisors, Prof. HONG Minghui and Prof. TAN Leng Seow from the Electrical and Computer Engineering Department in National University of Singapore, for introducing me to research activities and guiding me during the early stages of my scientific career and stay in Singapore.

I am thankful to Dr. Matthew Benjamin BORLEAND for developing the engineering aspects in me and introducing me to the world of screen printing and helping me in understanding the machines and their operations in a better way. Thanks to Dr. Bram HOEX and Dr. Prabir Kanti BASU for their contributions

to my work, and helping me understand the fabrication of silicon wafer solar cells, and for several enlightening discussions.

Special thanks to two important people, Dr. Ziv HAMEIRI and Dr. Johnson WONG for helping me understand about the characterisation of silicon wafer solar cells: Ziv for making me understand photoluminescence imaging and showing how to stay humble and Johnson for introducing me to advanced solar cell modelling using Griddler and for always being a go-to person to discuss any technical queries regarding silicon wafer solar cells.

I would like to thank the entire team at SERIS, especially the Silicon Materials and Cells Cluster, for their support during this work. Special thanks to Dr. Ankit KHANNA, Dr. Shubham DUTTAGUPTA, Kishan DEVAPPA SHETTY, Naomi NANDAKUMAR, Dr. Ge JIA, Ranjani SRIDHARAN, Jessen CUNNUSAMY, Samuel RAJ, Edwin CARMONA, and Dr. Debajyoti SARANGI, for their help in processing and characterisation of silicon wafer solar cells at SERIS. Thanks to Ann ROBERTS for her help with all administrative work at SERIS. Huge thanks to two very important people: Shubham and Kishan for making the stay at SERIS extremely pleasant. The ‘three musketeers’ days during the early stages of our career will remain fresh in my memories for a long time. Thanks for all the support, for the countless coffees that we had, and for helping me unconditionally throughout.

Special thanks to industry partners from DEK (Jessen CUNNUSAMY, Michael ZAHN, Dr. Xiao CHEN), DUPONT (Scott IGGO, Justin LIN, Amy SU), HERAEUS (Dr. ZHANG Yi, Dr. CHEN Chilong, Dr. Arno STASSEN and Peter HORAN), BTU (Jeffrey TAN, Andrew, Gaik CHIP), DESPATCH (Pierre, Jon BOGGARD), ASAHI CHEMICALS (Kai Hwa CHEW and SC Tan), and METALOR (Priscilla HONG, Steve BURLING, Stewart HEMSLEY) for the support and guidance throughout this PhD.

I want to thank my family, especially to my wonderful parents for their endless love and support. I am indebted to my parents for inculcating in me the dedication and discipline to do whatever I undertake well. Thanks to my brother and his family for their affection and support. Thanks to Adithya VINODH, Shwetha

KARTHIK and Nivedha KARTHIK, for being wonderful and making our lives special. Last but not the least, heartfelt thanks to my wife Mahalakshmi for being so special and for the sacrifices she had to make during my PhD studies. Thank you for your understanding and encouragement.

Vinodh SHANMUGAM,

1 February 2016, Singapore.

Table of Contents

Abstract

This thesis focuses on the development and characterization of printed metallisation of phosphorus doped silicon surfaces for solar cell applications. Metallisation of phosphorus doped surfaces using screen-printed silver pastes is a well-established process. The contacts to phosphorus doped surfaces ('emitters') are made by firing screen-printed thick film silver pastes through the passivating silicon nitride film. However, its performance is limited by several fundamental factors. Its inability to reliably print fine metal lines on the front surface results in significant shading losses. And the requirement for a heavily doped phosphorus surface to ensure a low-resistance ohmic contact results in increased Auger recombination losses in the phosphorus doped emitter surface layer.

Reducing the screen-printed metal line width helps in reducing the shading losses, but it also increases the line resistance due to the non-uniformity of the printed metal line profile. Of the various available printed metallisation methods, stencil printing promises to be the potential alternative to replace screen printing for fine-line metallisation. The well-defined line openings in stencils help in printing fine lines with uniform finger profile. This work compares two high-throughput printing technologies, namely printing by screens *vs.* stencils. The main focus of this work is to report on the effects of the topography of the printed silver metal lines on their conductance and also its impact on the current-voltage characteristics of the fabricated solar cells. Uniform print line definition and optimised silver paste utilisation makes stencil printing the appropriate choice for fine line metallisation.

In Si wafer solar cells, forming good contact between the phosphorus emitter and the screen-printed Ag paste is essential to achieve high photovoltaic (PV) efficiency. The emitter diffusion profile can greatly influence the solar cell characteristics such as junction shunting, contact resistance, open-circuit voltage and short-wavelength response. Theoretically, emitters with lower surface doping concentration are

preferable due to reduced emitter saturation current density, which results in higher open-circuit voltage and short-circuit current density. However these benefits can only be reaped if the metal paste is able to contact the more lightly doped phosphorus surface. This work analyses the contact formation process of two commercially available silver pastes on phosphorus emitters with varying doping profiles. The influence of surface concentration of the phosphorus emitters on both the electrical properties and the contact formation process are investigated. Microstructural analysis of the contact formation process reveal that a high density of silver crystallites with a very thin interfacial glass layer is required for contacting phosphorus emitters with low surface doping concentration.

Metal contacts introduce significant recombination via the high interface defect density and the emitter damage caused by the high-temperature firing step. Both the metal contact recombination as well as the electrical resistance of the contacts are important factors in the optimization problem of the phosphorus diffused emitter profile. Aside from the issue of contact quality, shallow emitters are more prone to junction shunting and increased recombination losses introduced by the metallisation process than emitters with deeper junction. Hence the optimal diffused emitter for an industrial silicon wafer solar cell has a significantly heavier diffusion and lower sheet resistance than one which minimizes the emitter saturation current density (J_{0e}), although the recent vast improvements in silver paste technology are enabling a trend towards higher emitter sheet resistance.

A photoluminescence imaging based method is used in this work for the extraction of recombination parameters at the metal-silicon interface. Newly developed test structures and measurement methods are presented to accurately determine the metal contact recombination parameters. This requires measurements on both a finished solar cell and on a wafer printed with the special test pattern. The added advantage related to analysis by photoluminescence imaging is that it is a contactless technique, so that automation of the test routine can be accomplished without having to design a dedicated jig with alignment probes.

The various losses associated with the screen-printed front side metallisation of phosphorus emitter surfaces (such as optical losses due to shading, electrical losses due to series and shunt resistance, and metallisation induced recombination losses) are discussed in this work. Methods to overcome these losses and new methods to characterize these losses are proposed in this thesis. In conclusion, this thesis presents significant progress in the development and characterization of front-side silver contacts to the phosphorus diffused emitters of silicon wafer solar cells, using industrial processing conditions. The price of silver is expected to remain high and hence it is important to lower the silver consumption per cell as a means of achieving further cost reductions of PV electricity.

List of Tables

List of Figures

List of Symbols

Symbol	Description	Unit
A	solar cell area	cm^2
I	current	A
I_{mpp}	current at the maximum power point	A
I_{ph}	photo-generated current	A
I_{sc}	short-circuit current	A
J	current density	A cm^{-2}
J_{01},J_{02}	saturation current densities of diodes in the two-diode model	A cm^{-2}
$J_{01\text{ metal}}$, $J_{02\text{ metal}}$	metal contact recombination currents	A cm^{-2}
J_{mpp}	current density at the solar cell's maximum power point	A cm^{-2}
J_{ph}	photo-generated current density	A cm^{-2}
J_{sc}	short-circuit current density	A cm^{-2}
J_{0e}	emitter saturation current density	A cm^{-2}
V_{oc}	open-circuit voltage	mV
η	energy conversion efficiency	%
n_2	ideality factor of the 2nd diode	
FF	fill factor	%
PFF	pseudo fill factor	%
FF_0	fill factor corrected for the influence of series and shunt resistance	%
FFJ_{01}	upper limit of fill factor set by first diode recombination	%
ΔFFJ_{02}	loss in fill factor due to second diode recombination	%

P_{mpp}	power at the maximum power point	W
R_s	series resistance (area weighted)	Ω cm^2
R_{sh}	shunt resistance (area weighted)	Ω cm^2
R_c	contact resistance (area weighted)	Ω cm^2
ρ_c	specific contact resistance (area weighted)	Ω cm^2
c	speed of light in vacuum	m s^{-1}
λ	wavelength	m
h	Planck's constant	m^2 kg s^{-1}
E_v	valence band edge	eV
E_c	conduction band edge	eV
E_0	characteristic energy	eV
E_F	Fermi energy level	eV
q	elementary charge	eV
Φ_m	work function of a metal	eV
Φ_s	work function of a semiconductor	eV
Φ_{BN}	*n*-type semiconductor and metal Schottky barrier height	eV
N_D	dopant concentration	cm^{-3}
σ_{long}	1.5 cm line segment conductivity	S cm
σ_{short}	250 µm line segment conductivity	S cm
α	power law scaling factor	
f_{metal}	metal contact areal fraction	%

List of Abbreviations

Abbreviation	**Description**
2D	two-dimensional
3D	three-dimensional
Ag	silver
Al	aluminium
AM 1.5G	air mass 1.5 global spectrum
ARC	antireflection coating
BB	busbar
BSE	back scattered electron
BSF	back surface field
CIJ	continuous inkjet printing
CO_2	carbon dioxide
c-Si	crystalline Silicon
Cu	copper
Cz Si	Czochralski-grown silicon
DOD	drop on demand
DI	deionised
ECV	electrochemical capacitance voltage
EL	electroluminescence
EQE	external quantum efficiency
FE	field emission
HCl	hydrochloric acid

H_2SO_4	sulphuric acid
HNO_3	nitric acid
IPA	isopropyl alcohol
IPCC	intergovernmental panel on climate change
IQE	internal quantum efficiency
I-*V*	current-voltage
KOH	potassium hydroxide
M3D	maskless mesoscale material deposition
multi-Si	multicrystalline silicon
mono-Si	monocrystalline silicon
mpp	maximum power point of a solar cell
PCB	printed circuit board
PECVD	plasma-enhanced chemical vapour depositions
PL	photoluminescence
PSG	phosphosilicate glass
PTP	pattern transfer printing
PV	Photovoltaics
QE	quantum efficiency
QSSPC	quasi-steady-state photoconductance
RCA	Radio Corporation of America
SEM	scanning electron microscope
SE	secondary electrons
SiN_x	silicon nitride
SR	spectral response
STC	standard test conditions

TE	thermionic emission
TFE	thermionic field emission
TLM	transfer length method
WAR	weighted average reflectance

Chapter 1: Introduction

1.1 Need for renewable energies

Energy is vital for human development. Energy demand is expected to increase considerably in the coming years as the result of population growth and economic development. World population is projected to grow by 0.9% per year on average, from an estimated 7.0 billion in 2012 to 9.0 billion in 2042 [1] [2]. The inevitable increase in world population and the economic development that must necessarily occur in many countries have serious implications for the environment, because the current energy generation processes based on fossil fuels are polluting and harmful to the environment [3]. More than 80% of the current global energy needs are met by fossil fuel-based energy sources (oil, coal and natural gas) [4] [5]. Burning fossil fuels creates carbon dioxide, the number one greenhouse gas contributing to global warming. The overwhelming consensus of researchers is that global warming is real and is caused by human activity, primarily by the burning of fossil fuels that pump carbon dioxide, methane and other greenhouse gases into the atmosphere. Fossil fuel combustion accounts for about 90% of the total global carbon dioxide emissions [6]. The effects of global warming are more evident than ever, with reports suggesting increase in average temperatures, extreme weather events, melting of glaciers and rise in sea levels [7].

The urgent need to cut carbon emissions makes the development of renewable energy technologies essential. The potential of renewable energy sources is enormous and they can in principle meet many times mankind's energy demand. Renewable energy sources such as solar, biomass, wind, hydropower and geothermal power can provide sustainable energy services, based on the use of routinely available, indigenous resources [8]. It is becoming clear that future growth in the energy sector is primarily in the new regime of renewables, and not in conventional oil and coal sources. Renewable energy will not only play a key role in restoring balance to the natural environment, but will also provide better energy security to many countries.

1.2 Motivation for photovoltaics

Among various renewable energy sources, solar energy has several intrinsic advantages. It is a widely accessible and environmentally friendly source which has the potential to meet mankind's global energy requirements. As illustrated in Figure 1-1 solar energy is by far the largest source of inexhaustible power available to us. The annual energy received from the sun exceeds the total estimation of fossil resources. The solar energy that hits the earth's surface in one hour is equivalent to mankind's total annual energy consumption [9]. One possible way to use solar energy is the direct conversion of incident solar energy to electricity by photovoltaic (PV) technology using semiconductor devices called solar cells. Almost all solar cells on the market today use semiconductor materials to harness solar energy using the PV effect, whereby silicon wafer based technologies dominate today's market [10]. Some of the reasons are that silicon is a cheap, abundant material and that the bandgap of crystalline silicon (*c-Si*) is well suited for PV applications. In addition, its success can be attributed to the fact that it is a proven technology, benefitting from material and process research from the microelectronics industry which is largely based on silicon.

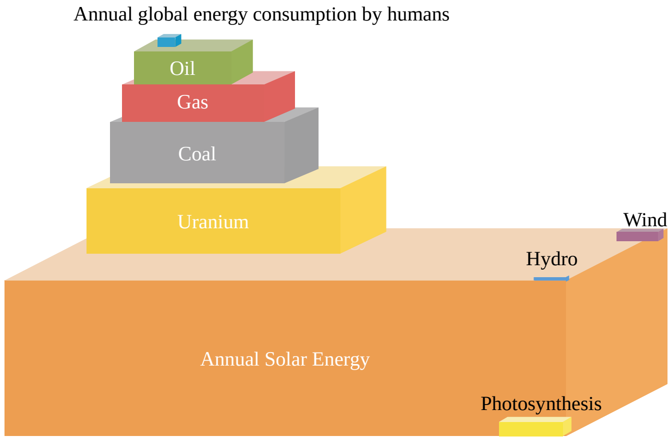

Figure 1-1: Total energy resources available to mankind [9].

The *c-Si* PV market has gone through tremendous price reductions over the past decades. Figure 1-2 shows the learning curve of *c-Si* PV, which shows the average selling price of a *c-Si* module per watt-peak (US$/$W_p$) as a function of the cumulative module shipments from 1976 to 2014 in megawatt-peak [11]. A learning rate (LR) plot of 21.5% is superimposed on the data, which implies that for every doubling of the cumulative shipments, there is about 21.5% reduction in the price of the modules. This learning rate is the highest in the energy world. The learning rates of 1% for hydro-electric power, 5% for geothermal power and 7-9% for wind power fade in comparison [9]. Two major deviations noticed in Figure 1-2 can be attributed to a temporary shortage of silicon feedstock around 2004-2007 and an overcapacity around 2012-2014 [12]. Despite these, the PV market is expected to continue at its average historical LR in the fore-seeable future. The 100 GW_p cumulative PV module power shipment landmark was exceeded in 2012 and the current shipped module power is estimated to be approximately 184 GW_p.

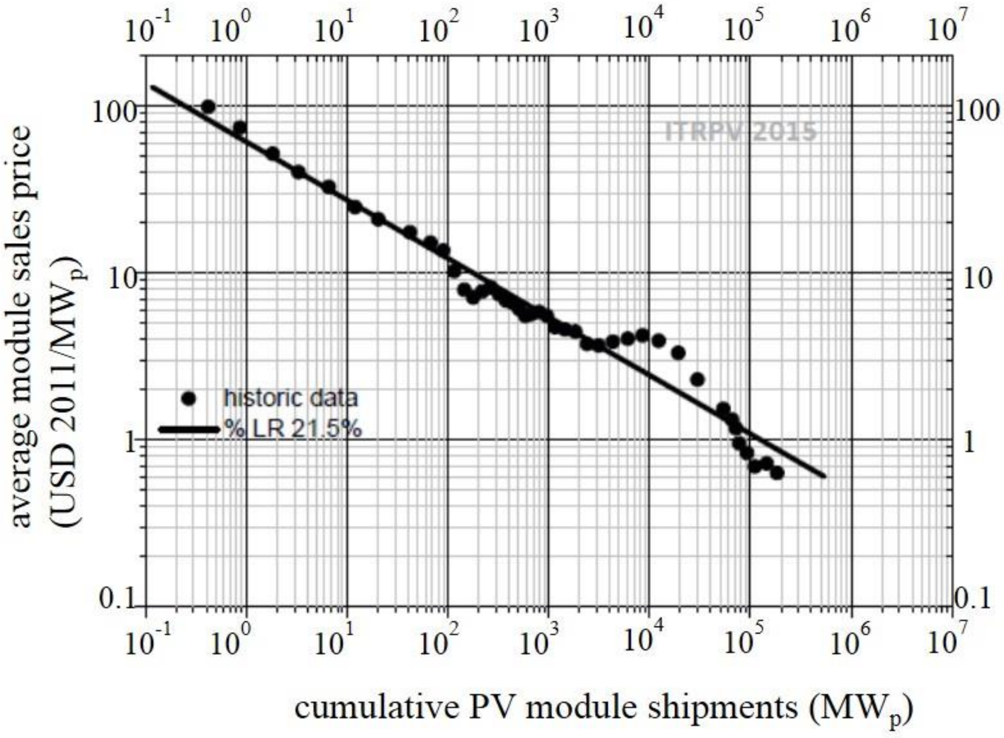

Figure 1-2: PV learning curve. The average crystalline silicon module price as a function of the cumulative crystalline silicon module shipments [11].

Despite the advantages of utilizing a virtually unlimited energy source, the penetration of PV power in the global energy supply is essentially dictated by economics. Today, PV contributes only ~0.1% of the global energy mix [13]. Hence the main focus of PV technology research is towards cost reduction, in order to achieve an energy cost that is comparable, or even lower, than the conventional fossil fuel based energy sources. For a crystalline silicon wafer solar cell manufacturer there can be two main strategies for cost reduction: (1) advanced or cost-effective manufacturing technologies which improve the solar cells' energy conversion efficiency and (2) the reduction of materials costs associated with the solar cell fabrication (this is achieved by reducing the usage of expensive materials for solar cell processing or through the use of thinner Si wafers).

The PV community is in a constant push to reduce manufacturing costs. Cost analysis reports have shown metallisation pastes to be the second most expensive material (first being the silicon wafer) in the process of making silicon wafer solar cells. Metallisation technologies and processes have a significant impact on both the cell efficiency and materials cost (due to the use of expensive metals like silver). Therefore this thesis focuses on the development and characterization of front-side silver contacts to phosphorus doped emitters, using industrial processing conditions.

1.3 Front side metallisation by screen printed Ag paste

Metallisation of phosphorus doped surfaces using screen printed Ag paste is a well-established process and also a key process in the production of silicon wafer solar cells. Screen printing is expected to remain the dominant metallisation method for *c-Si* solar cells until 2025 [11]. It is widely used by the PV industry due to its robust, simple and highly automated process, and also due to the rapid developments in the metallisation pastes. Metallisation pastes using Ag are the most process-critical and most expensive non-silicon material used in the current solar cell fabrication process. The paste consumption per cell therefore needs to be reduced. The PV market has been a strong market for Ag consumption. In 2013, 88 Moz (millions of ounces) of Ag were estimated to be consumed by the PV industry, and in the long run [14] the Ag price might increase to levels that cannot sustain the current low costs of screen printed cells, as the PV industry scales up and drives up demand. Even in the short term, the Ag price is prone to wild fluctuations which presents unfavourable conditions for the PV industry. The volatility of the Ag price in 2011-2012 was as high as 60% [15]. Because the price of silver is expected to remain high, it is extremely important to continue efforts to lower the silver consumption per cell as a means of achieving further cost reductions.

Strategies to replace or reduce Ag include the use of copper (Cu) or various alloys. Cu has a marginally lower conductivity than Ag, but it is more than 100 times cheaper than Ag [16]. Cu applied with plating technologies is the envisioned substitute for screen printed Ag contacts in the PV industry [17]. However, the major disadvantage of Cu is its high diffusion coefficient in Si even at room temperature [18]. Technical issues related to the reliability and adhesion of plated Cu contacts have to be resolved before alternative metallisation methods can be introduced. Front side metallisation by screen printed Ag paste is therefore expected to remain the most widely used process for standard *c-Si* wafer solar cells in the foreseeable future.

1.4 Thesis motivation

In Si wafer solar cells, forming good contact between the phosphorus emitter and the screen-printed (Ag) metal paste is essential to achieve high PV efficiency. The contacts to the phosphorus emitters are made by firing Ag containing pastes through passivating silicon nitride antireflection coatings, and it remains the dominant metallisation method. However, its dominant position is constantly challenged by pressures within the PV industry to reduce costs by cutting down on Ag metal consumption. The front side Ag consumption for a 156 mm × 156 mm *c-Si* wafer was around 100-130 mg/cell in 2014. Reducing the screen printed line width helps in reducing the shading losses and helps in reducing the Ag metal consumption, but also increases the line resistance due to the non-uniformity of the printed metal line profile. The contact resistivity values obtained by firing thick-film Ag metal pastes through the passivating silicon nitride coating to contact the phosphorus doped surface are orders of magnitude higher than the theoretically expected *n*-type Si emitter/Ag contact resistivity values. Screen printed Ag metal contacts also introduce significant recombination via the high interface defect density and the emitter damage caused by the high-temperature firing step. Both the metal contact recombination as well as the electrical resistance of the contacts are important factors in the optimization problem of the phosphorus diffused emitter profile.

The motivation of this thesis is on the application and characterization of advanced printed metallisation methods which are potentially suitable for cost-effective high-efficiency Si wafer solar cells. The topics discussed in this PhD thesis work such as fine-line Ag printing using stencils, understanding the contact formation to lightly doped phosphorus emitters, and the development of a new method to characterize the metal contact recombination parameters will be helpful to enable the transition towards Ag reduction in the front-side metallisation of silicon wafer solar cells. This in turn would strengthen the dominance of the screen and stencil printing metallisation methods and reduce the manufacturing cost of Si wafer solar cells.

1.5 Outline of this thesis

This thesis is divided into seven chapters, as follows:

Chapter 1 highlights the need and urgency to look into renewable resources for energy generation and in particular photovoltaics as the most promising alternative. This is followed by a description of the cost and challenges associated with *c-Si* solar cell technology, with special emphasis to front-side metallisation of phosphorus doped surfaces by screen printed Ag contacts. Finally the motivation of this thesis is presented.

Chapter 2 briefly presents the basic principles of silicon wafer solar cells. It also describes the fabrication process and the characterization methods used in this work. The Schottky model of metal-semiconductor contact theory is discussed. Various printed metallisation methods for the front-side metallisation of phosphorus doped surfaces such as screen printing, stencil printing, inkjet printing, aerosol jet printing, laser transfer printing, flexographic printing, pad printing, are reviewed.

Of the various available metallisation methods for printing front metal grids on to solar cells, stencil printing is the potential alternative to replace the traditional screen printing method for fine line metallisation.

In **Chapter 3** two high-throughput printing technologies, namely printing by screens *vs.* stencils are compared. A statistical method is introduced in this work to evaluate the quality of the printed front metal grid based on distributions of printed metal line profiles, line segment conductance, overall electro-luminescence pattern, and solar cell light current-voltage characteristics. The effect of topography of the printed Ag metal lines on its conductance and also its impact on the electrical characteristics of the fabricated solar cells are studied. Uniform print line definition and optimised Ag paste utilisation makes stencil printing the appropriate choice for fine line metallisation.

In **Chapter 4** the electrical and micro-structural properties of screen-printed contacts formed with two different Ag screen printing pastes (Sol 9411 and Sol 9600) on phosphorus diffused silicon emitters with different surface doping concentrations and emitter depths are investigated. Theoretically, emitters with lower surface doping concentration are preferable due to reduced emitter saturation current density, which results in higher open-circuit voltage V_{oc} and short-circuit current J_{sc} (and thus PV efficiency). However, these benefits can only be reaped experimentally with screen-printed contacts if the pastes are able to contact the more lightly doped n^+ surface. Microstructural analysis of the contact formation process reveals that a high density of Ag crystallites with a very thin interfacial glass layer is required for contacting phosphorus emitters with low surface doping concentrations.

The metal-silicon interface in a solar cell is a highly recombination active region that impacts the device voltage. A new method is developed for the accurate determination of the metal recombination parameters at the metal-silicon interface. This developed method is explained in **Chapter 5**. By analysing test patterns and finished solar cells using intensity-dependant photoluminescence imaging, the metal recombination parameters are extracted. Three different kinds of boundaries for the mini-cells are also experimented in this chapter and the results are presented.

Phosphorus emitter diffusion profile can greatly influence the solar cell characteristics. The degree of metal recombination in Si solar cells depends on the emitter profile itself. In **Chapter 6**, the new method developed in this work for the extraction of metal contact recombination parameters is applied on phosphorus emitters with varying junction depths and surface doping concentrations. All solar cells fabricated in this chapter, uses the same screen printed Ag paste. As the phosphorus emitter profile becomes shallower, the metallisation induced recombination losses increases. The clear trend obtained on the variation of the metal contact recombination values with respect to phosphorus emitter doping profiles are strengthened by analysing various test structures which are explained in details in this chapter.

Chapter 7 presents a summary of this PhD research work and highlights the author's original contributions. The chapter ends with a brief discussion of the future research motivated by this thesis.

Chapter 2: Background and literature review

2.1 Basic principles of solar cells

Semiconductor solar cells generate electric power under illumination due to PV effect. The PV energy conversion in solar cells consists of two essential steps. 1) Absorption of light generates electron-hole pairs. 2) The generated electron-hole pairs are then separated by the *p-n* junction in the solar cell (electrons to the negative terminal and holes to the positive terminal – thus generating electric power)**.**

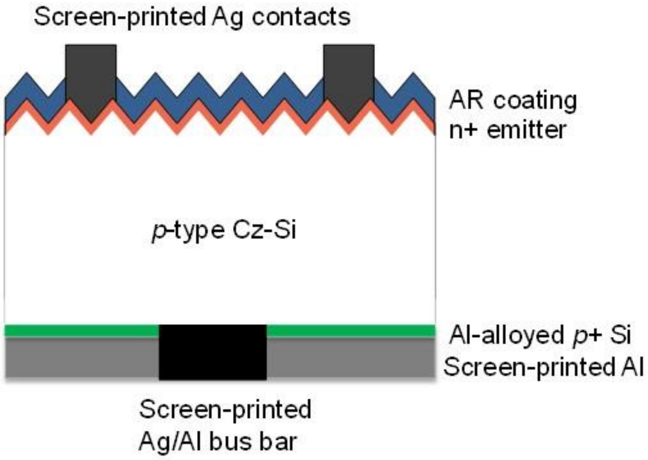

Figure 2-1: Schematic of a standard Al-BSF silicon wafer solar cell.

Industrial silicon wafer solar cells are basically large-area diodes consisting of a relatively thick *p*-type base (160 - 180 µm) and a shallow *n*-type emitter (phosphorus doped emitters with a thickness of less than 0.5 µm). On the front side of the solar cell, there is an antireflection coating and silver metal contacts (to contact the phosphorus doped surface) and on the rear side, there are aluminium metal contacts, and silver/ aluminium busbar metal contact as shown in Figure 2-1. Crystalline Si has an indirect bandgap of 1.12 eV (~1108 nm) at 300 K [19] and photons with energy higher than the bandgap are absorbed and lead to electron-hole pair generation. After carrier generation, the generated minority carriers will recombine unless they are efficiently separated from the majority carriers by the *p-n* junction. After efficient carrier separation, the electrons are collected by the front n^+ side while the holes are collected by the rear p^+ side. And now the photon generated current flow can be extracted via an external load.

2.2 Current-voltage characteristics

One of the most important measures for describing the performance of a solar cell is its current-voltage (I-V) characteristics. It is common to normalize the current to the area of the solar cell (J = I/A). A typical *I-V* curve of a solar cell under dark and illumination is shown in Figure 2-2. A Si wafer solar cell in dark conditions has the rectifying *I-V* characteristics of a diode. And when illuminated with light, the photo-generated current shifts the forward-bias *I-V* curve of a solar cell to the fourth quadrant, as shown in Figure 2-2. The negative current means that the photo-generated current flows in the opposite direction of the forward biased current of the diode.

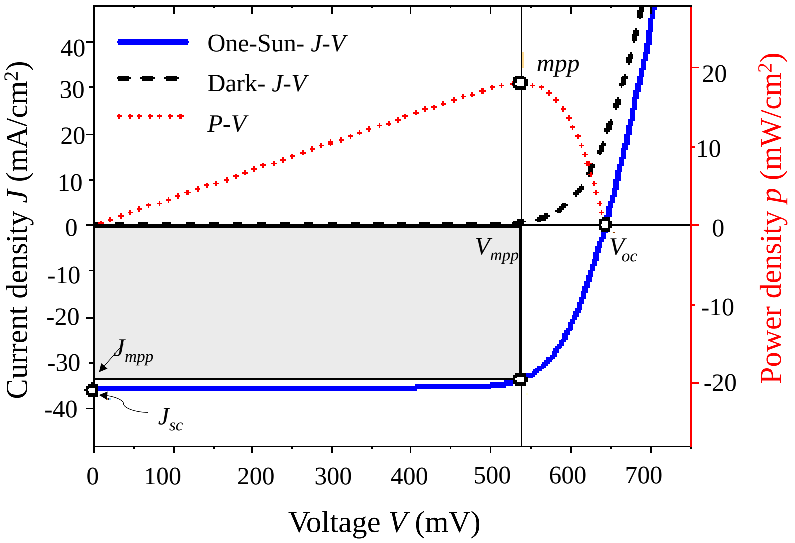

Figure 2-2: Illuminated and dark I-V curve and the power density vs. voltage of a solar cell, illustrating the key parameters.

The current generated by a solar cell can be approximated by the two-diode model [20].

$$J(V) = J_{01}\left(exp\left(q\,\frac{(V-jR_s)}{n_1\,k\,T}\right)-1\right)+J_{02}\left(exp\left(\frac{q(V-JRs)}{n2kT}\right)-1\right)+\frac{V-JR_s}{R_p}-J_L \qquad (2.1)$$

with q being the elementary charge, k the Boltzmann constant, T the temperature, J_{01} is the saturation current density in the emitter and the base, J_{02} is the saturation current density in the space charge region. The factors n_1 and n_2 are the ideality factors of the two diodes in the 2-diode model. R_p is the shunt resistance and R_s is the series resistance. The corresponding equivalent circuit diagram is shown in Figure 2-3.

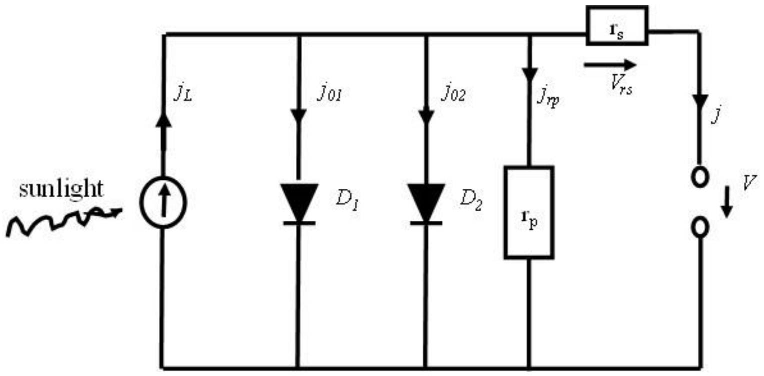

Figure 2-3: Equivalent circuit diagram (two diode model) of a solar cell [21]

From the illuminated *I-V* curve, basically four important parameters of the solar cells can be extracted. The short-circuit current density (J_{sc}) is the maximum possible current density of the solar cell (extracted when the voltage is zero in the illuminated *I-V* curve), the maximum possible voltage is the open-circuit voltage (V_{oc}, extracted when the current is zero in the illuminated *I-V* curve). The operating point corresponding to the maxima of the power-voltage curve is called the maximum power point (*mpp)* and the corresponding current density, voltage and power are labelled J_{mpp}, V_{mpp}, and P_{mpp} respectively. The other main parameter to describe the quality of the solar cell is the efficiency (η),which is defined as the ratio of the power at the maximum power point (P_{mpp}) to the power of the incident light (P_{in}). The efficiency is obtained from an *I-V* measurement, while the solar cell is illuminated and kept at constant conditions with a temperature of 25^0C, light intensity of 1000 W/m^2, and using the AM 1.5G spectrum [22] .

$$\eta = \frac{P_{mpp}}{P_{in}} = \frac{V_{mpp}\,J_{mpp}}{P_{in}} = \frac{V_{oc}\;J_{sc}\;FF}{P_{in}} \tag{2.2}$$

The ratio of maximum power point (P_{mpp}) and the product of ($J_{sc}\,V_{oc}$) is called the fill factor *FF*. The *FF* can be regarded as the ratio of two squares [23], the largest square fitting under the *I-V* curve and the square defined by V_{oc} and J_{sc}.

$$FF = \frac{V_{mpp}\,J_{mpp}}{V_{oc}\;J_{sc}} \tag{2.3}$$

The *FF* is an important factor and it should be as large as possible. The metallisation process has a significant influence on the solar cell's fill factor. The quality of the formed metal-semiconductor junction influences the shape of the *I-V* curve and therefore the value of the fill factor. Typical values for *FF* of *c-Si* solar cells are 76-80% [24] and the theoretical maximum value that can be attained is 89.3% [25].

2.3 Efficiency limitations for silicon solar cells

The theoretical maximum conversion efficiency of a Si wafer solar cell with a bandgap of 1.12 eV is limited to approximately 30% [25, 26]. This physical limitation for the efficiency mainly originates from the bandgap of Si and the main reasons are listed below.

- Photons with energy smaller than the bandgap of Si cannot generate an electron-hole pair (This corresponds to photons with wavelength greater than 1100 nm)
- Only one electron-hole pair can be generated by a photon of sufficient energy. Photon energy exceeding 1.12 eV is transferred to heat.

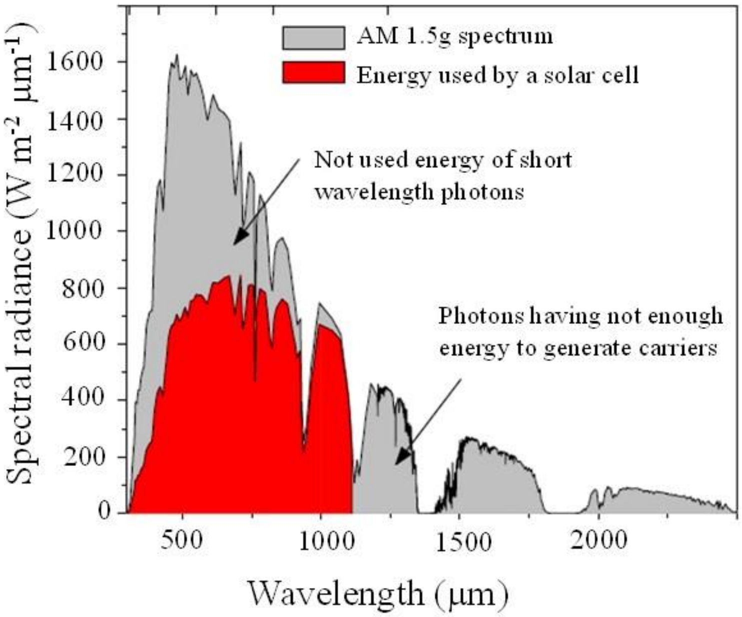

Figure 2-4: Schematic drawing of spectral radiance of the AM 1.5g spectrum plotted versus the wavelength. The part of the spectrum utilised by a silicon solar cell is illustrated by the red-shaded area, redrawn from [21].

- The maximum achievable open-circuit voltage is far below 1.12 V. It is the separation of the quasi Fermi levels, and not the bandgap, that defines the open-circuit voltage of the solar cell.
- As the current depends exponentially on the voltage, the maximum power of the solar cell is not equal to the product of the open-circuit voltage and the short-circuit current density. Due to non-rectangular *I-V* characteristics, the fill factor of the solar cell is limited to about 85% [21].

In addition to the above-mentioned loss mechanisms, optical losses due to surface reflection and metal shading, electrical losses due to series and shunt resistances, further reduce the conversion efficiency of silicon wafer solar cells. The highest conversion efficiency ever reported for a Si solar cell measured under standard testing conditions is 25.6% [27]. Typical industrially processed solar cells now achieve efficiencies of about 17-18% for multicrystalline and 18-19% for monocrystalline silicon wafers [28]. The main reason for this difference is that monocrystalline silicon wafers have a higher minority carrier diffusion length and better surface texturing properties than multicrystalline silicon wafers, and hence have a higher conversion efficiency [29].

2.4 Fabrication of *c-Si* wafer solar cells

A schematic representation of the conventional aluminium back surface field (Al-BSF) silicon wafer solar cell is shown in Figure 2-1. More than 80% of the silicon solar cells commercially produced in 2014 had this architecture, because of its relatively simple and well-known production sequence with high throughput rates. The fabrication of these standard Al-BSF solar cells is briefly discussed in this section. And the schematic of the major steps in the fabrication process is shown in Figure 2-5.

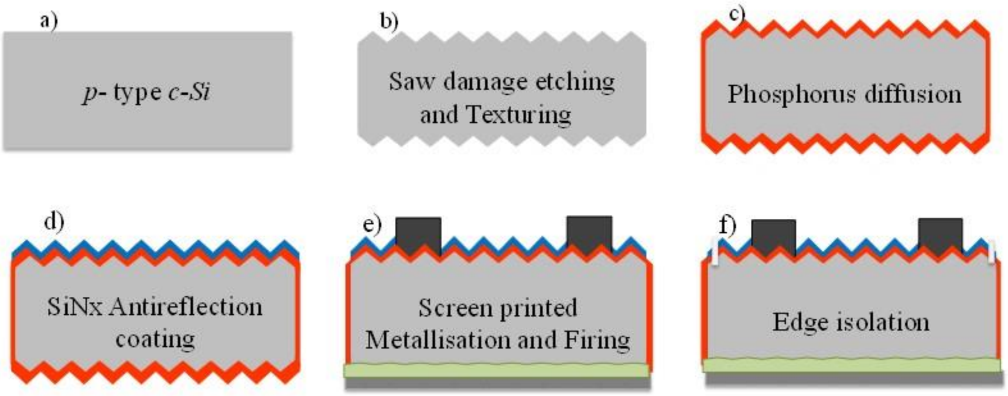

Figure 2-5: Fabrication process of Al-BSF silicon solar cells.

In this thesis, for the fabrication of standard Al-BSF silicon wafer solar cells, boron doped (typically 10^{15} – 10^{16} cm^{-3}) multicrystalline silicon (multi-Si) or Cz-grown monocrystalline silicon (mono-Si) wafers with dimensions of 156 mm × 156 mm and an area of 239 - 243 cm^2 and a thickness of 150 - 200 µm are used. To increase the absorption of light, the Si wafers are wet-chemically textured (using an acid solution in the case of multi-Si wafers and an alkaline solution in the case of mono-Si wafers. On mono-Si wafers with <100> orientation, a standard random pyramid surface texture is created by alkaline etching composed of potassium hydroxide (KOH) mixed with isopropyl alcohol (IPA), which simultaneously removes the saw damage on the Si surface (arising from the wire sawing of the Cz-Si ingots) and results in pyramids on the surfaces. KOH etches Si crystallographic planes with a <100> orientation faster than planes with a <111> orientation [30] [31]. This anisotropic etching creates pyramidal surfaces on the wafer surface with square bases (<100>) and intersecting <111> oriented crystallographic planes as the pyramidal walls. The heights of the pyramids across a textured surface are randomly distributed, and hence this texture is often referred to as a random-pyramid surface texture. These pyramids are effective in coupling the incident light into the cell, and reduces the weighted average reflectance over the solar spectrum to about 10%, whereas the bare Si wafer prior to texturing has a weighted reflectance of about 30%.

On the other hand multi-Si wafers exhibit a wide range of crystal orientations and hence non-selective etching solutions are commonly used. An acidic etching solution comprising of hydrofluoric acid (HF) and nitric acid (HNO_3) based solution is used to simultaneously remove the saw damage and create random hemispherical structures irrespective of the Si grain orientation [32, 33]. And this isotropic etching process improves the light absorption by reducing the reflection from the multi-Si wafer surface. For further reduction of reflection, the so called honeycomb texturing process is an alternative for multi-Si wafers.

The textured wafers are then wet-chemically cleaned by a standard cleaning sequence, Radio Corporation of America (RCA) clean 1 and 2, an HF dip, and a deionised (DI) water rinse [34]. RCA 1 uses a solution of ammonium hydroxide (NH_4OH) and hydrogen peroxide (H_2O_2) to remove organic impurities and RCA 2 uses a solution of hydrogen chloride (HCl) and H_2O_2 to remove metallic impurities.

As the substrate is *p*-type, a thin layer of *n*-type Si - the emitter - is created by phosphorus diffusion to form a *p*-*n* junction, which separates the light-generated e-h pairs. Emitter formation is one of the most critical and crucial process steps in the fabrication of standard Si wafer solar cells. The emitter diffusion process can be performed using either a tube furnace or an inline belt furnace, and both these methods are used in this work. Emitter diffusion generally involves two steps. First, a phosphorus glass (P_20_5) layer is grown on the Si surface, then a high-temperature step follows, by which phosphorus atoms diffuse into the silicon, thereby forming an *n*-type emitter layer. The phosphorus glass (PSG) layer acts as an infinite phosphorus source during the diffusion process. The maximum amount of phosphorus atoms that can be incorporated in the Si crystal lattice is determined by the diffusion/annealing temperatures, which typically are in the range of 750 to 950^0 C in the PV industry [35].

An important parameter for contact formation, and thus this work, is the sheet resistance of the emitter, including emitter profile and surface doping concentration. The emitter diffusion profile can greatly influence the solar cell characteristics such as junction shunting, contact resistance, open-circuit voltage, and short-wavelength response of the solar cells [36]. Figure 2-6 shows the profiles of some emitters that were frequently used in this work, as measured by Electrochemical Capacitance-Voltage measurements (ECV) [37]. The impact of these emitter profiles on the contact formation and metal recombination will be investigated in detail in Chapters 4 and 6, respectively.

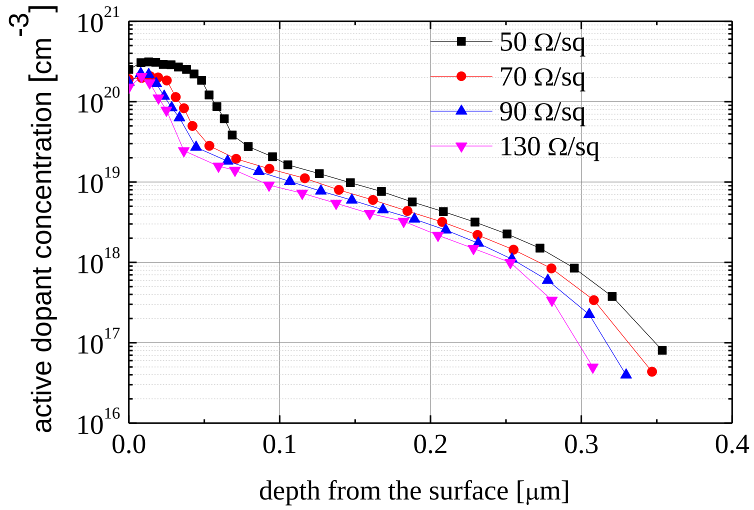

Figure 2-6: ECV doping profiles of the different phosphorus emitters used in this thesis.

After the diffusion process, the PSG layer is removed by a HF dip. As all wafer surfaces are diffused (front, rear, side edges) during this step, a shunt path is formed between the wafer's front and rear surfaces, which needs to be disconnected. The edge isolation process to disconnect this shunt path can be done wet chemically using strongly oxidising acids like nitric acid (HNO_3) and sulphuric acid (H_2SO_4) followed by HF etching [38]. Alternatively the wafers can be edge isolated using a laser to isolate the parasitic junction at the edges, as shown in the Figure 2-5. The laser isolation step may be done as the last step in the fabrication process of the solar cell.

An amorphous silicon nitride (SiN_x) is then deposited by plasma-enhanced chemical vapour deposition (PECVD) onto the front surface, in order to increase light absorption and to passivate defects at the Si surface to reduce surface recombination. Textured mono-Si wafers with an antireflection coating of SiN_x (approximately 70 nm) can achieve a solar weighted average reflectance of ~2% in the 300 - 1000 nm range and multi-Si wafers can achieve a reflectance of ~7% in the 300 - 1000 nm range [39]. The SiN_x layer also provides excellent surface passivation of the emitter front surface [40].

In order to collect the photo-generated carriers, metal contacts are required on both sides of the wafer. Screen printing metal pastes on the solar cell front and rear with subsequent drying of the metal pastes followed by co-firing of the metal pastes is the most widespread metallisation process in the PV industry. A typical solar cell requires three types of screen printed metal contacts: 1) Aluminium paste is used to metallise the full area of the rear side, 2) Ag/Al paste is used as pads on the rear side to enable inter-connection of solar cells in the solar module (Ag/Al pads are required, in addition to Al paste, because Al paste cannot be soldered), and 3) The front side of the solar cell is metallised using Ag paste. The Ag front grid metallisation of a solar cell covers about 6-10% of the total area using an H-pattern with three busbars and perpendicular fingers. Both front and rear contacts are simultaneously co-fired in an IR heated belt furnace to form the electrical contacts to the Si [41]. A typical firing temperature profile used in this thesis is shown in Figure 2-7. The profile was recorded during the firing process using a thermocouple soldered on to a metal plate.

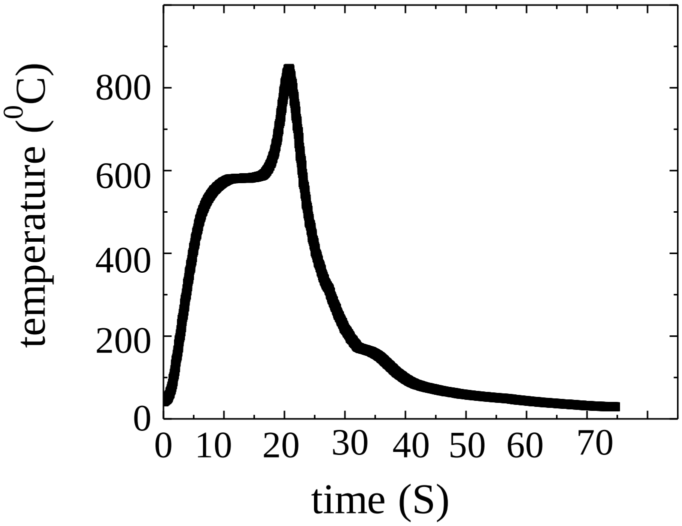

Figure 2-7: Firing temperature profile for an Al-BSF solar cell used in this work. The profile was recorded during the firing process using a thermocouple soldered onto a metal plate.

During this co-firing process, the glass frit in the front Ag paste melts and etches the front SiN_x layer to make a contact with the underlying n^+ Si surface [42]. And on the rear surface, the Al paste alloys with the Si wafer to create an Al doped p^+ Si region. The formed high-low junction at the rear due to Al paste alloying with Si, known as the back surface field (BSF), creates an electric field which repels minority carrier electrons from the highly recombination active metal/Si contact. The firing profile affects the uniformity and the thickness of the formed BSF [43]. The firing process for Ag contacts has huge impacts on the final solar cell performance, for several reasons. Insufficient firing leads to poor metal/Si adhesion and increases the resistive losses, due to poor contact resistance at the metal/Si interface. In the other extreme, over-firing drives the metal deep in the junction, causing junction shunting. Both these effects reduce the cell's fill factor and consequently its efficiency.

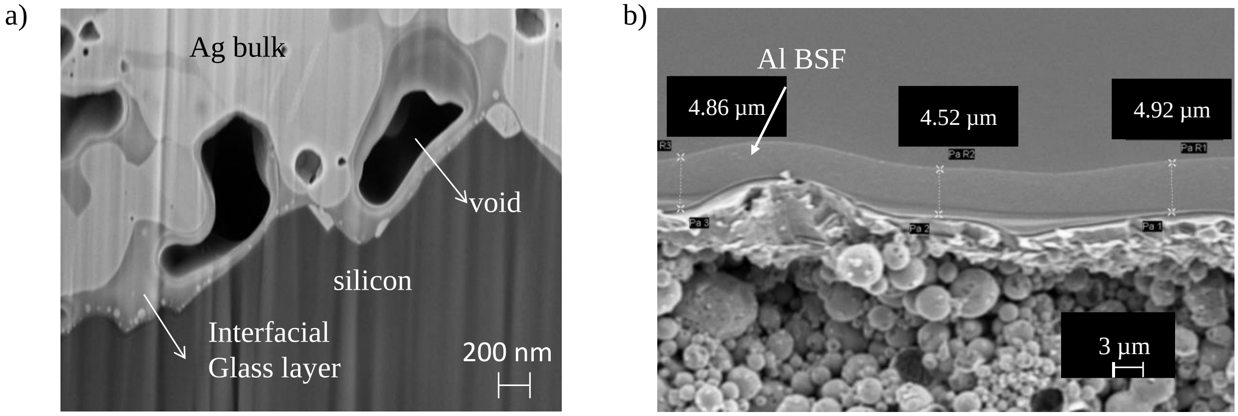

Figure 2-8: Optimisation of the firing process requires a complex balance between the front side Ag contact resistance and the BSF quality on the rear. a) SEM image of the Si-Ag interface and b) SEM image of the Al-BSF formed after the co-firing process.

Hence optimisation of the firing process requires a complex balance between front contact resistance and the BSF quality on the rear, which in turn affects the fill factor and the open-circuit voltage of the solar cells [44, 45]. In this thesis, silver pastes of different generations and manufacturers are applied. Screen printed metallisation of phosphorus doped surfaces with different Ag pastes is investigated in Chapter 4.

2.5 Characterisation techniques

This section provides a brief overview of the different characterisation techniques used in this thesis, to characterise the phosphorus diffused emitter surfaces, printed metal contacts and the fabricated silicon wafer solar cells.

2.5.1 Characterisation of phosphorus diffused emitter surfaces

2.5.1.1 Sheet resistance measurements

The emitter sheet resistance is a widely used figure of merit of diffused phosphorus emitters in Si solar cell processing. The sheet resistance is a characteristic property of the emitters and is commonly expressed in terms of “Ohms per square”. The industry standard for the measurement of the sheet resistance of the emitters is the four point probe method. Passing a current through the two outer probes, and measuring the voltage through the two inner probes, allows the measurement of the sheet resistance of the thin doped emitter layer. A four point probe mapping tester (Napson) was used to study the sheet resistance uniformity of the phosphorus diffused emitters in this work. The emitter sheet resistances of the silicon solar cells fabricated in this work lie in the range of 50-130 Ohm/square.

2.5.1.2 Electrochemical capacitance-voltage profiling

The doping profile of phosphorus diffused emitters has a strong influence on the metal-semiconductor contact formation. Hence it is important to measure the doping profiles. In this thesis, electrochemical capacitance-voltage (ECV) profiling was used to determine the doping profiles of phosphorus emitters [37]. ECV measures the electrically active doping profile. The measurements were carried out on a WEP control CVP-21 profiler and the commonly used emitter profiles in this thesis are shown in the Figure 2-6. The impact of these profiles on the metal-semiconductor contact formation and the metallisation induced recombination losses are discussed in this work.

2.5.1.3 Emitter saturation current density

In *c-Si* solar cells, surface passivation studies of heavily doped emitter regions are very important. They are usually characterised by the emitter saturation current density J_{0e}. This saturation current density is an important parameter which limits the open-circuit voltage and hence the efficiency of the solar cell. Kane and Swanson introduced a method for the extraction of J_{0e} from photoconductance measurements at high injection levels from specially prepared symmetrical lifetime samples [46]. In this thesis, the effective lifetime and the saturation current density of the samples were measured using the photoconductance tool WTC-120 from Sinton Consulting Inc.

2.5.2 Characterisation of printed front grid metal contacts

2.5.2.1 Optical surface profiler

The shapes of the printed metal fingers plays a major role in the line resistance. In this work, the printed metal fingers were characterised optically and electrically. 3D optical profiles of the printed line segments were captured using the Zeta optical profiler system [47]. The optical profiler yields the 3D height information of the printed fingers with high resolution. 3D profiles of metal fingers printed using screens and stencils having 60 µm opening, is shown in Figure 2-9 [48]. Optical analysis of fine-lines printed with screens and stencils are reported in Chapter 3.

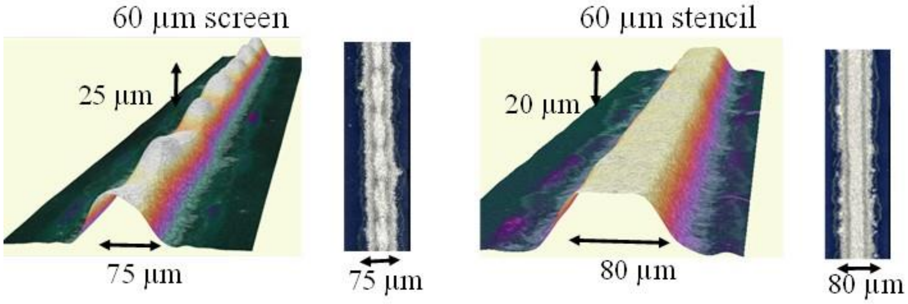

Figure 2-9: Optical and 3D profile of a screen and stencil printed metal line measured using an optical surface profiler.

2.5.2.2 Contact resistance measurements

The contact resistance refers to the resistance associated with the metal-semiconductor contact barrier and this can be measured by the transfer length method (TLM) [49]. The magnitude of this contact resistance depends strongly on the doping concentration of the emitter. Low values of contact resistance are associated with heavy surface doping concentration, and vice versa. Dedicated test structures (Circular TLM patterns) or isolated strips cut from metallised solar cells are required for TLM measurement [50] [51]. Since the test structure/isolated strip contact area is not the same as cell contact area, it is meaningful to use an area weighted parameter called specific contact resistance as a figure of merit for evaluating the contact quality of the solar cell samples. The impact of the phosphorus emitter doping profile on the specific contact resistance values for printed Ag pastes are studied in Chapter 4.

2.5.2.3 Scanning Electron Microscopy

The Scanning Electron Microscopy (SEM) investigations of this thesis were performed with the Carl Zeiss Auriga model at SERIS. In SEM, a focused beam of high-energy electrons (typically 1-15 keV) is scanned over the surface of a material. The electron beam interacts with the material, causing a variety of signals such as secondary electrons, back-scattered electrons, X-rays, etc [52]. Each of these can be used to characterise a material with respect to specific properties. Secondary electrons are valence electrons of atoms in the sample ejected due to inelastic collisions with other high-energy electrons. SEMs rely primarily on the secondary electron detectors to form images of the investigated surface. Secondary electrons are a tool for topographical analysis of the specimen surface, since changes in the surface topography of the sample, influences the number of secondary electrons that escapes from the surface [53]. In this work, SEM measurements were used to obtain cross-sectional images as well as top-view images of the printed Ag metal at the metal-Si interface, as shown in Figure 2-10.

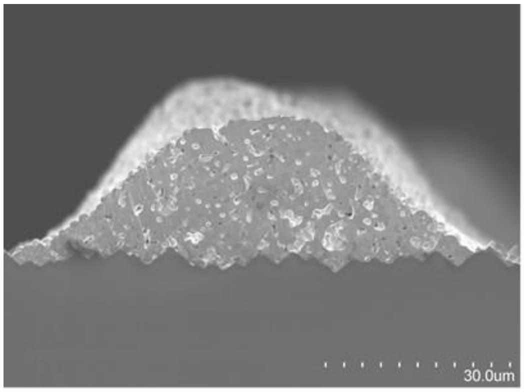

Figure 2-10: SEM image of the Si-Ag interface.

2.5.2.4 Contact etching process

Screen printed Ag contacts are characterised by complex interfacial regions comprising of a resistive glass layer, Ag crystallites, nanocolloids of Ag particles, and voids. The high series resistance is often a problem with the printed contacts, mainly due to the glass frits (in the Ag paste) that flow preferentially towards the Ag-Si interface during the high temperature firing step. This creates an interfacial glass layer between the Ag contact and the Si, and this in turn increases the contact resistance between the Ag and the Si [54, 55]. In order to explore the different front components by SEM, selective etching techniques are applied [56, 57], as shown in Figure 2-11 and Table 2-1. The impact of these different front components (interfacial glass layer, Ag crystallite density) on the contact formation process are investigated in Chapter 4.

Table 2-1: Sequential etching used to selectively etch the Ag bulk, interfacial glass layer and the Ag crystallites using nitric acid and HF solutions.

Step	Chemical Used	Duration (s)	Purpose
1	68% HNO_3 acid at 60 ^{0}C	120	Removal of bulk Ag
	DI water rinse	60	Cleaning off HNO_3
2	5% HF dip at room temperature	30	Removal of interfacial glass layer
	DI water rinse	60	Cleaning off HF
3	68% HNO_3 acid at 60 ^{0}C	120	Removal of Ag crystallites to reveal imprints left on silicon surface
	DI water rinse	60	Cleaning off HNO_3

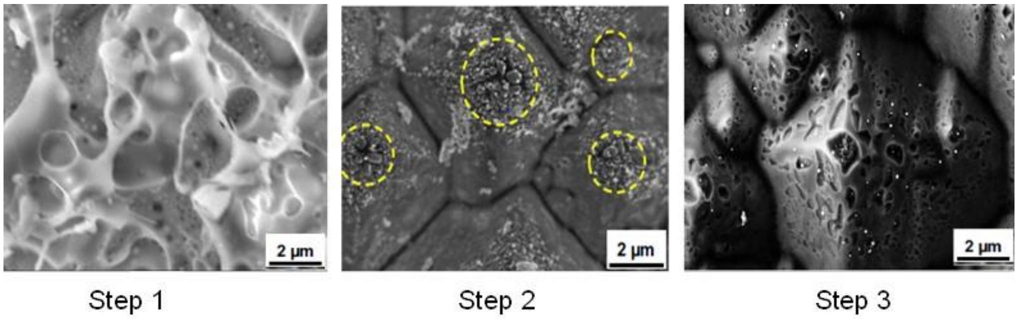

Figure 2-11: SEM micrographs of the interfacial glass layer (after removal of bulk Ag), Ag crystallites (after removal of the interfacial glass layer) and the Ag crystallite imprints (after removal of the Ag crystallites) at the Ag-Si interface obtained after selective etching.

2.5.3 Characterisation of silicon wafer solar cells

2.5.3.1 Current-voltage measurement

I-V measurement is the most important characterisation technique for a solar cell. Solar cell *I-V* curves under illuminated or dark conditions provide valuable information. Efficiency, fill factor, short-circuit current density, open-circuit voltage, series resistance and shunt resistance are some of the valuable information of the solar cells that can be extracted from the illuminated and dark *I-V* measurements [58]. At SERIS, one-Sun *I-V* curves were measured using a tester with steady state illumination (Aescusoft, SolSim 210) or discrete flashes (Sinton Instruments, FCT-350). Dark *I-V* curves were also measured using the SolSim 210 *I-V* tester.

2.5.3.2 Spectral response measurements

The spectral response (SR) of a solar cell is the ratio of current generated by a solar cell to the power of the incident illumination, measured over a range of wavelengths (typically 300 to 1200 nm for *c-Si* cells). SR is conceptually similar to the quantum efficiency (QE). QE is the ratio of the number of electron-hole pairs separated by a solar cell to the number of incident photons. The relation between the solar cell's external quantum efficiency (EQE) and the SR is shown below. The internal quantum efficiency (IQE) of a solar cell follows from the EQE and the solar cell's spectrally resolved reflectance (R). A widely used method to calculate the IQE is to divide the EQE by (1-R) for each wavelength. Front and rear surface recombination velocity, diffusion length at the emitter and at the base, width of the depletion region, length of the emitter, light trapping properties are some of the important material properties that can be extracted from the SR and QE of the solar cell [59, 60]. An Enlitech SR-156 large-area spectral response analyser was used at SERIS for spectral response measurements.

$$SR = \frac{q\lambda}{hc} EQE \tag{2.4}$$

$$IQE = \frac{EQE}{1-R} \tag{2.5}$$

2.5.3.3 Suns-*Voc* measurement

The Suns-*Voc* measurement gives a *Jsc*-V_{oc} curve by obtaining the V_{oc} for different Suns or illumination intensity using a quasi-steady-state light pulse from a flash lamp. The solar cell is illuminated by a flash lamp and the rate of decay of illumination is kept low enough for the cell's V_{oc} to be assumed in a quasi-steady-state with illumination intensity over the range of illumination decay [61]. The Suns-V_{oc} measurement gives the base saturation current density (J_{01}), the junction leakage current (J_{02}), and a pseudo-*FF* without the series resistance effect (R_s). A pseudo-efficiency without the effect of R_s can also be obtained by this technique, to assess the impact of R_s. The difference between the illuminated *I*-*V* curve and the Suns-V_{oc} *I*-*V* curve is a good measure of the effect of series resistance on the cell. In this thesis work, Suns-V_{oc} curves were measured using a Sinton Instruments Suns-Voc tester.

2.5.3.4 Luminescence imaging

Luminescence is the emission of light that is observed upon an external excitation of specific materials such as semiconductors. In Si, band-to-band luminescence is emitted when electrons from the conduction band recombine with holes in the valence band. And the imaging system is designed to detect band-to-band luminescence only. Photoluminescence (PL) or electroluminescence (EL) refer to photon emission by a semiconductor when excited by incident photons or an external bias, respectively. In both the cases, the emitted photons are a result of charge carrier excitation and subsequent radiative recombination. Luminescence imaging is now widely used for Si wafer solar cell characterisation, with applications including spatially resolved mapping of diffusion length [62], Si wafer defects, minority carrier lifetime [63], diode-model parameters [64], electrical cell parameters [65, 66], etc.

In this thesis, PL imaging is used for the determination of metal contact recombination parameters. The advantage with regards to PL measurements is that it is a contactless technique and this provides the flexibility to characterise the Si wafer after every fabrication process. PL and EL were done at SERIS using a luminescence imaging tool from BT Imaging.

2.6 Loss mechanisms associated with front grid metallisation process

The main focus of this thesis is on the analysis of printed Ag metal grids to contact phosphorus doped surfaces on the front side of the conventional silicon wafer solar cells. The front metal contact grid design is an important area in the design of silicon wafer solar cells.

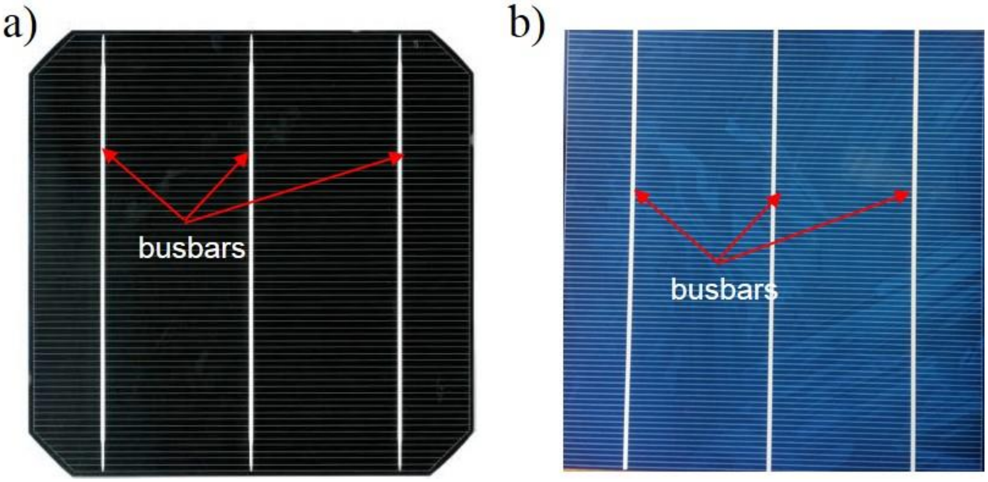

Figure 2-12: Scan of the fabricated solar cell a) front side of a mono-Si wafer solar cell, b) front side of a multi-Si wafer solar cell. The front grid metallisation of the solar cell covers approximately 6-10% of the total area in an H-pattern with three busbars and perpendicular fingers.

The current on the rear side is collected by the full-area metallised Al layer and on the front side by the fine metal Ag fingers and busbars. There are several power loss mechanisms associated with the front grid of the solar cell, and a reduction of all these losses is needed to optimise the solar cell performance.

2.6.1 Optical losses

Optical losses are caused by the presence of the metal on the top surface of the solar cell which prevents light from entering into the solar cell. Around 6-10% of the front surface is covered by the Ag metal grid, and hence shading losses plays a major role for the performance of industrial silicon wafer solar cells. The impact of printed Ag finger profile on the shading losses are discussed in detail in Chapter 3 of this thesis.

2.6.2 Electrical resistance losses

The series resistance and shunt resistance primarily affect the fill factor of the solar cell. Shunt resistance losses due to front side metallisation process occurs due to metal spiking the *p-n* junction and creating an ohmic path for the current to flow. The various components of the series resistance losses associated with the front grid metallisation process are R_{finger}, R_{busbar}, $R_{contact}$ and $R_{emitter}$, as shown in Figure 2-13. R_{finger} and R_{busbar} arise due to the ohmic resistance in the printed metal fingers [21]. Reducing the printed finger width increases the line resistance due to finger breaks and un-uniformity of the printed finger profile (peaks and valleys arising from the screen printing process) [48]. The impact of the finger profiles and ways to overcome this limitation of the screen printing metallisation process are discussed in this thesis.

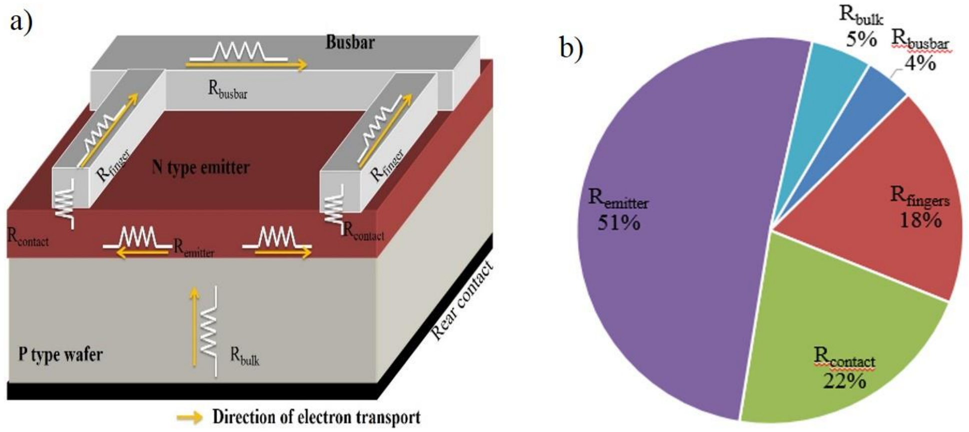

Figure 2-13: a) The different series resistance contributors for a standard Al-BSF Si wafer solar cell, b) Computed series resistance components of a fabricated screen-printed Al-BSF mono-Si solar cell (area of 239 cm^2). The different series resistance components are calculated analytically [23].

$R_{contact}$ is the series resistance losses associated with the metal semiconductor contact. The contact resistivity values of Ag paste varies with respect to emitter doping profile and the firing process. Minimising the contact resistance losses is essential for highly efficient silicon solar cells. Another important factor in front grid design is that of the resistive losses in the emitter layer $R_{emitter}$. The resistive loss due to the lateral flow of current in the emitter layer depends on the sheet resistance of the emitter, and is reduced by minimising the distance between the fingers. Closely spaced, wide fingers will reduce the series resistance losses but conversely increase the shading losses. Hence optimisation of the front contact grid requires a trade-off between the electrical and optical losses due to the front metal grids.

2.6.3 Metallisation induced recombination losses

The metal-silicon interface of a phosphorus doped emitter provides a highly recombination active surface for minority charge carriers. The phosphorus emitter diffusion profile can greatly influence the solar cell characteristics. Emitters with lower surface doping concentration are preferable (due to better blue response). But with the printed metallisation method, metal contacts introduce significant damage to the emitter due to the high-temperature firing step. As the phosphorus emitter profile becomes shallower and more lightly doped, the metallisation induced recombination losses increase. A new method to determine this metallisation induced recombination loss is developed in this work [67]. The metal contact recombination and the electrical resistance of the contacts are important factors in the optimization problem of the phosphorus diffused emitter profile.

2.7 Metal-semiconductor contact theoretical models

Metal contact formation is a complex and critical process in the fabrication of *c-Si* wafer solar cells. The metal-semiconductor contacts can be either ohmic (allowing the current to flow from the metal to the semiconductor or vice versa) or a rectifier type (allowing the current to flow only in one direction) [68]. The ideal metal contact for solar cells should be an ohmic contact (linear *I-V* characteristics) with negligible contact resistance [69]. However, the first metal-semiconductor contacts had a rectifying behaviour, as explained long ago by Schottky [70] and Mott [71]. In order to understand the conditions under which a metal-semiconductor contact shows ohmic characteristics, it is necessary to review the theoretical models of such contacts.

Figure 2-14 illustrates the energy band diagram of a metal-semiconductor contact, according to the Schottky model. If a metal and semiconductor are in direct contact, then the Fermi energy levels of the metal and the semiconductor need to align due to electron movement (from the material with higher Fermi energy level to the material with lower Fermi energy level), when both the materials are joined. The difference between the work function of metal and the semiconductor will lead to band bending at the semiconductor surface. The work function of the metal is defined as the energy difference between the vacuum and the Fermi level. The formed Schottky barrier, due to band bending determines the properties of the metal-semiconductor contact.

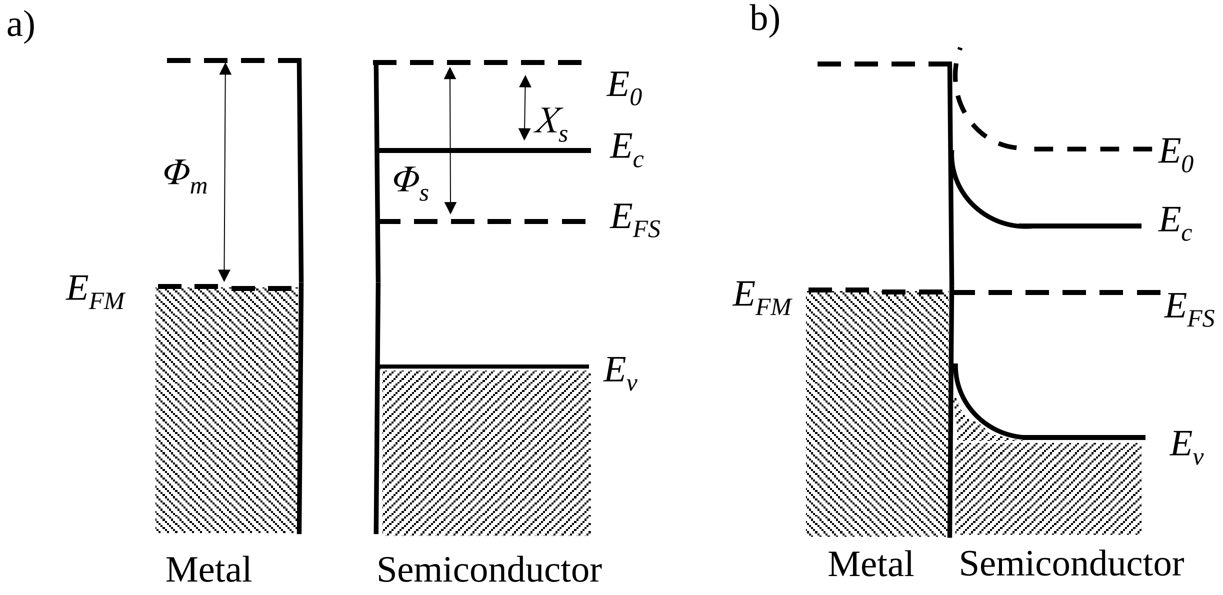

Figure 2-14: Energy band diagram of a metal and n-type semiconductor, (a) is before the contact is made and b) represents the band diagram after an intimate contact is made [16].

There are three possible band structures of metal and *n*-type semiconductor, as shown in Figure 2-15 [49]. (1) If the work function of the metal (Φ_m) is smaller than the semiconductor (Φ_s), then the electron transfers from the metal to the semiconductor until its Fermi levels are equalised. This results in an accumulation contact or ohmic contact. (2) If the work functions are equal ($\Phi_m = \Phi_s$), then the Fermi levels are aligned even before the contact formation. Hence after the contact formation, there is no band bending. (3) If the metal work function is larger than the work function of the semiconductor ($\Phi_m > \Phi_s$), then a rectifying contact is formed. In this case, due to band bending a potential Schottky barrier height (Φ_{BN}) is formed.

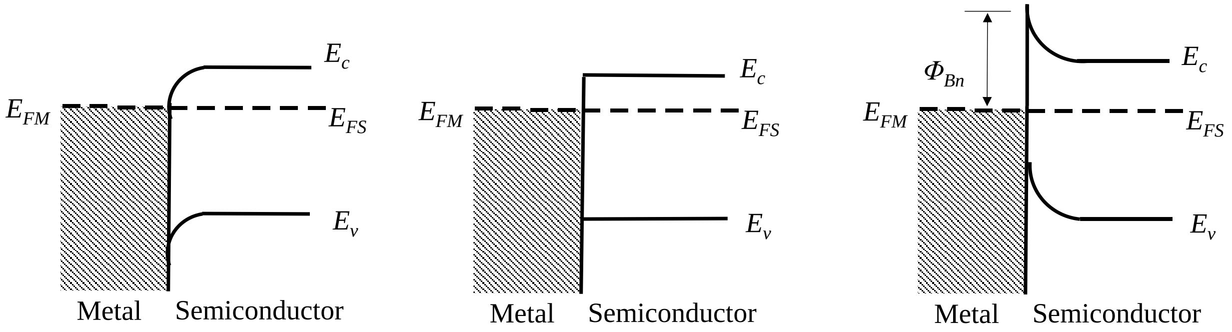

(a)
$\Phi_m < \Phi_s$

(b)
$\Phi_m = \Phi_s$

(c)
$\Phi_m > \Phi_s$

Figure 2-15: Band structure of a metal and n-type semiconductor contact depending on the work function of the metal and the semiconductor. a) Ohmic contact is formed when the metal work function is smaller than the semiconductor work function, b) similar work functions between the metal and semiconductor, c) rectifying contact is formed when metal work function is larger than the semiconductor work function [49].

In short, according to this model a potential barrier between metal contact and Si exists, depending on the difference between the metal work function and the silicon electron affinity. The most favourable condition for ohmic contact formation is the accumulation contact, in which the majority carriers can flow freely across the junction. Ideally it is possible to achieve an accumulation contact by choosing a metal of lower work function than the corresponding *n*-type semiconductor or a metal of higher work function than the corresponding *p*-type semiconductor.

The Schottky contact corresponds to an ideal aligning between the metal and the semiconductor. However, for a real contact the direct proportionality between metal work function and the potential barrier could never be measured [72]. Deviations from the Schottky models are commonly attributed to the presence of interface states with energy levels within the semiconductor's bandgap and also due to the effect of image force barrier lowering. The interface states "pin" the Fermi level and make the Schottky barrier relatively insensitive to the metal work function. The interface states may be due to dangling bonds at the surface, impurities or other defects. Image force lowering corresponds to the image force induced lowering of the potential barrier for charge carrier emission, in the presence of an electric field [73]. The potential barrier lowering due to image force effect, depends on the maximum field intensity, the width of the space charge region in the semiconductor and is hence indirectly dependent on the doping concentration and the externally applied voltage.

Based on the doping concentration of the semiconductor (N_D), three mechanisms are responsible for the transport of majority carriers (electrons for *n*-type) in a metal-semiconductor junction: 1) transport of electrons over a potential barrier by thermal excitation according to the model of thermionic emission (TE), 2) tunnelling of electrons through a thin potential barrier by field emission (FE), 3) a combination of TE and FE defined a thermionic field emission (TFE). In this, the electrons are thermally excited to an energy less than the barrier height to allow for consecutive electron tunnelling.

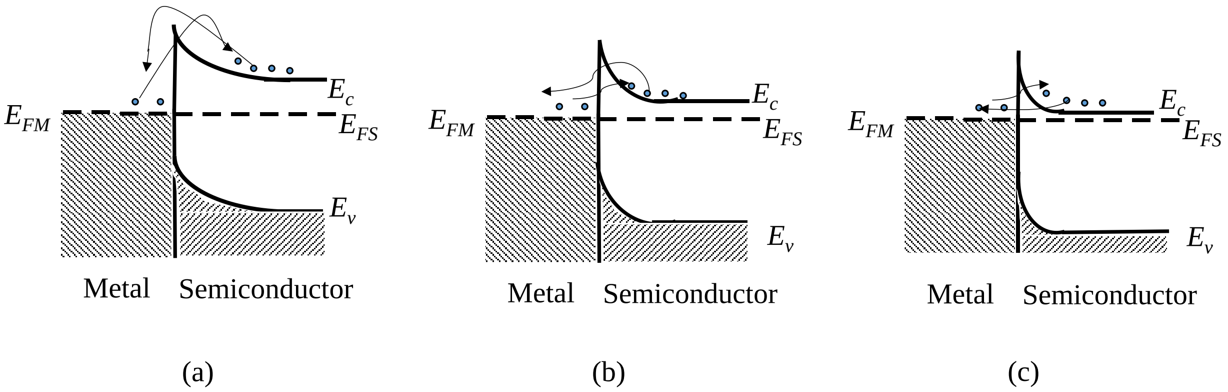

Figure 2-16: Current transport mechanisms in a metal-semiconductor contact. a) Thermionic emission over the potential barrier, b) thermionic field emission and c) field emissions through the potential barrier [21].

For low semiconductor doping concentration ($N_D < 1 \times 10^{17}$ cm^{-3}), the current is transported via TE over the potential barrier [74]. For $N_D > 1 \times 10^{19}$ cm^{-3}, the current is transported via FE through the potential barrier. For 1×10^{17} cm^{-3} < N_D < 1×10^{19} cm^{-3}, the current is transported via TFE, which is a combination of FE and TE [21, 75]. For standard screen printed Si solar cells, the phosphorus emitter surface doping concentration is $N_D > 1 \times 10^{20}$ cm^{-3}. This makes FE to be the most dominant conduction mechanism. However, Ag crystallites penetrate into Si during contact formation process, and hence contacts the lower doped phosphorus emitter regions [76]. The functional dependence of contact resistivity on the doping concentration for TE, FE and TFE in a *n*-type semiconductor is explained in detail by Yu and Padavoni [77] [78]. The impact of phosphorus emitter doping profile, primarily its surface doping concentration on the contact resistivity values and its effect on the solar cell performance are studied in Chapter 4.

2.8 Metallisation methods for silicon wafer solar cells

Various metallisation technologies are available for defining metallic contacts to silicon wafer solar cells. Metallisation technologies involving vacuum processes like evaporation, and sputtering requires the use of photolithography or a shadow mask for contact pattern (H-pattern on the front side of the wafer) definition. These limitations makes this method not only time-consuming but also a complex process and hence is not used for commercial silicon wafer solar cells. However, with these methods well defined contacts of very fine dimensions can be produced, and thus they are often used for the front-side metallisation of high-efficiency solar cells in the labs [79]. Electrochemical metallisation methods, or metal plating, involve deposition of metal ions from an electrolyte to the silicon wafer. Plating has its own limitations regarding metal adhesion and reliability [80], which prevents it from becoming the mainstream metallisation method for silicon wafer solar cells. Printing of metal pastes or inks to define metallic contacts has been the industry dominant metallisation method for Si wafer solar cells [81]. In this subsection, different printing methods available for the metallisation of Si wafer solar cells will be briefly discussed.

2.8.1 Screen printing

Screen printing is the most widely used metallisation method for defining metal contacts in the Si PV sector, due to its high throughput, reliability, high repeatability, good yield and lower cost when compared to other metallisation processes. This process was first introduced to PV in the 1970s [82] [83] and since then has remained the mainstream metallisation method, owing to constant development in the screens and metal pastes. The operating principle of screen printing process is represented in Figure 2-17. Screen printing involves printing a metal paste onto the Si substrate through a wire-mesh screen by the action of a squeegee. The squeegee moves across the screen and presses the metal paste through it. The screen consists of an aluminium frame, a mesh of wires (stainless steel or polyester mesh of wires) being clamped on to the frame and an emulsion layer, which is photolithographically structured with the desired printing image. Figure 2-18shows a microscopic image of a screen used in this work.

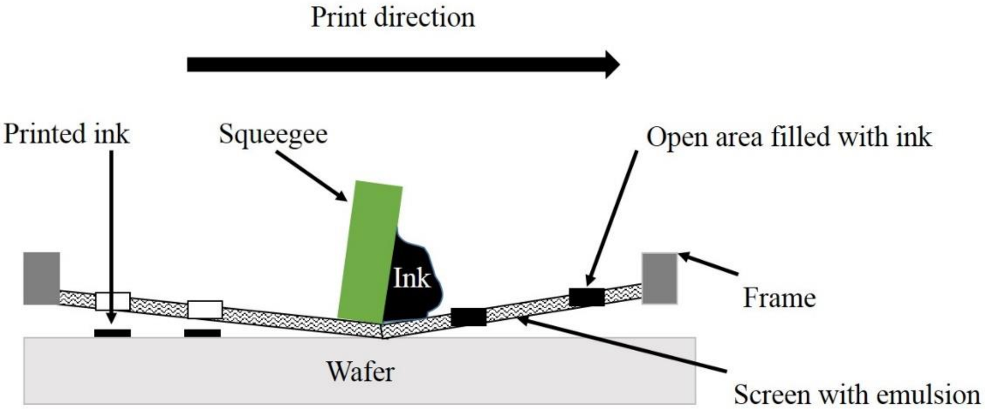

Figure 2-17: Schematic of a typical screen printing process.

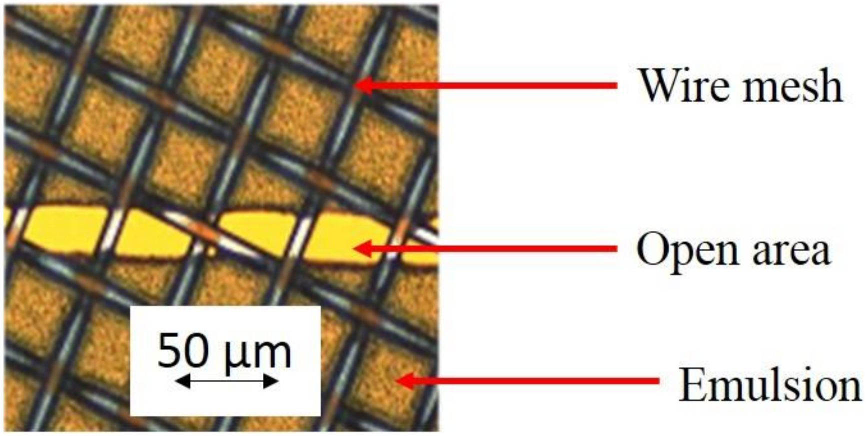

Figure 2-18: Optical microscopic image of a screen with stainless steel mesh used in this work.

2.8.2 Stencil printing

Stencil printing is a promising alternative to replace screen printing for front-side metallisation of silicon wafer solar cells [84]. Stencil printing is widely used in the printed circuit board (PCB) and semiconductor industry. Unlike screens with a wire mesh, a stencil features 100% open area in the aperture. This leads to excellent paste transfer and print line uniformity when compared to a mesh screen with an open area of around 60%. Stencils can be fabricated by different methods such as electroformed nickel, pulse laser processing and chemical etching [85, 86]. In this work electroformed nickel stencils are used and Figure 2-19 shows a microscopic image of a stencil used. Stencil printing uses the same base equipment and pastes (with slightly higher viscosity) that are used for screen printing applications, and this makes it readily adoptable by solar cell manufacturers.

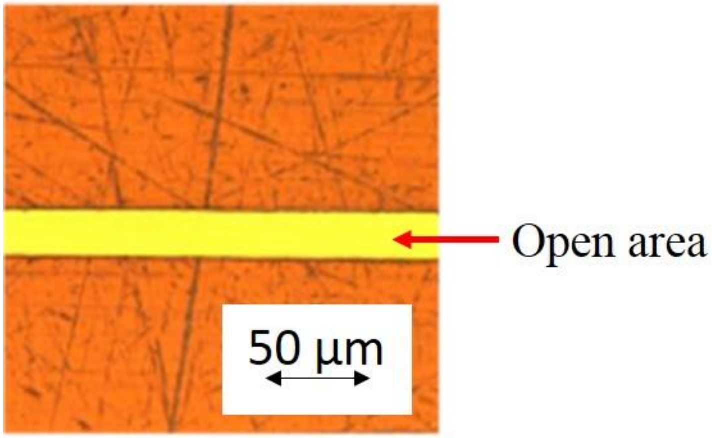

Figure 2-19: Optical microscopic image of a stencil used in this work.

2.8.3 Inkjet printing

Inkjet printing is a direct-write non-contact deposition technology with high print line resolution [87]. In 1987, first attempts were undertaken to use inkjet printing for the front side metallisation of silicon wafer solar cells [88]. It is a contactless technique which makes this metallisation method ideal for thin wafers (< 100 µm). In general the inkjet printing technology can be broadly classified as continuous inkjet printing (CIJ) and the drop on demand inkjet printing (DOD) [89]. A schematic of a widely used DOD printer is shown in Figure 2-20. The pulse voltage applied to the piezoelectric transducer controls the opening and closing of the nozzle for ink deposition. This digital patterning feature of the inkjet printing technique omits the need for screen fabrication and facilitates flexible and fast prototyping of desired metallisation patterns.

The metallisation process with inkjet printers can be divided into two categories: 1) seed and plate approach [90] (where a seed layer is printed using inkjet followed by electroplating), 2) full height inkjet printing [91] (where the metal finger is printed only using inkjet). Selective doping, patterning, masking, printing etching barriers are other applications wherein inkjet printers have been used [87]. The requirement of a special nano-particle based metal ink to prevent clogging of the inkjet printing nozzle and the lack of many ink suppliers prevents this method from becoming the dominant metallisation process for silicon wafer solar cells.

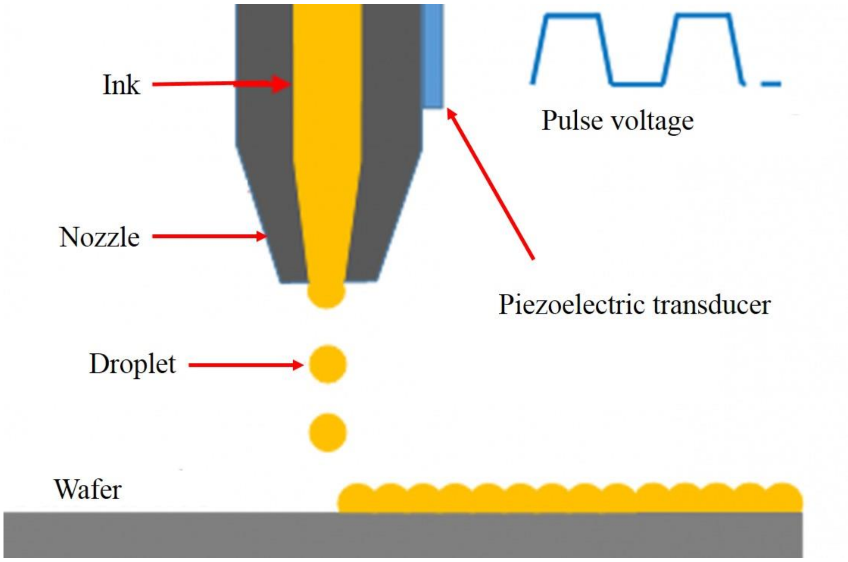

Figure 2-20: Operating principle of a drop on demand inkjet printing process [92].

2.8.4 Aerosol jet printing

The metal aerosol jet printer is a Maskless Mesoscale Material Deposition (M3D) technique from Optomec INC., USA [93]. This is a non-contact technique and hence has the same advantages as an inkjet printer. This technology became available in 2004, and is very different to the inkjet printing technology. It relies on the aerodynamic focusing of an aerosol consisting of ink droplets entrained in a carrier gas to form depositions. This method was developed to create fine lines on the front side of the cell which function as a seed layer for later electroplating. Specially designed metal inks [94] and nozzle clogging are some of the common drawbacks with this metallisation method. Using the aerosol jet printer, printed metal lines with a width of 30-40 µm and thickness of 1-5 µm were achieved. Figure 2-21 shows the schematic drawing of an aerosol jet printer.

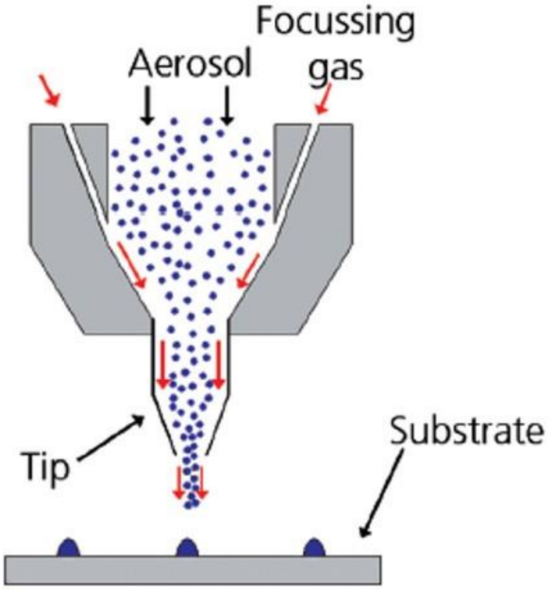

Figure 2-21: Schematic of an aerosol printing process [69].

2.8.5 Flexographic printing

Flexographic printing, also referred to as flexography, is a high-speed rotational printing method which is widely used in graphic arts and package printing on roll-to-roll materials like cardboard, paper or foil. The schematic of a flexographic printing platform for the metallisation of silicon wafer solar cells is shown in Figure 2-22. The printing plate is mounted on a printing cylinder using an adequate substructure with defined height and compressibility. A steel cylinder referred to as “Anirox roll”, transfers a specific amount of ink from the ink reservoir on to the elevated areas of the printing plate [95]. Due to the compressibility of the printing plate, this method is well-suited for the transfer of fine-line structures onto rough substrates. The first successful feasibility study of this printing method for metallisation of solar cells was demonstrated in 2011 [96]. Using this approach, several studies demonstrated flexographic printed seed layers down to 25 µm line width. Similar to inkjet and aerosol jet printing, flexographic printing method also requires specially designed metal ink.

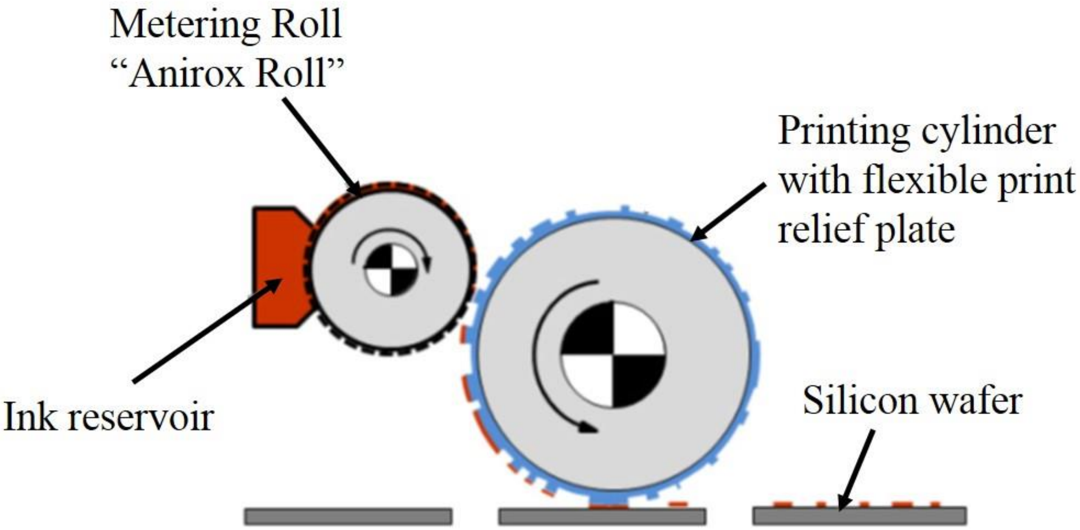

Figure 2-22: Schematic of a flexographic printing process [95].

2.8.6 Pad printing

Pad printing is a kind of gravure offset printing technique that offers the possibility of a simple, economic and high-throughput production of fine lines up to 30 µm even on uneven surfaces [97]. A transfer pad printing machine consists of a silicone rubber transfer pad, an engraved cliche and an ink tray with spatula or doctor blade or ink cup. The printer motion is reciprocating, whereby the cliche is inked with a spatula and then cleaned by a doctoral blade while simultaneously the image of the previous working cycle is transferred from the cliche to the solar cell via the pad. The wafer can be printed once or in repeating mode, depending on the desired printed ink volume. This technology was investigated intensively at Fraunhofer ISE [21]. Although it was possible to print very narrow contact lines, the height of the printed contacts is reduced simultaneously and this results in decreased line conductivity. However in combination with a subsequent plating process, pad printing was considered an ideal method to from the seed layer.

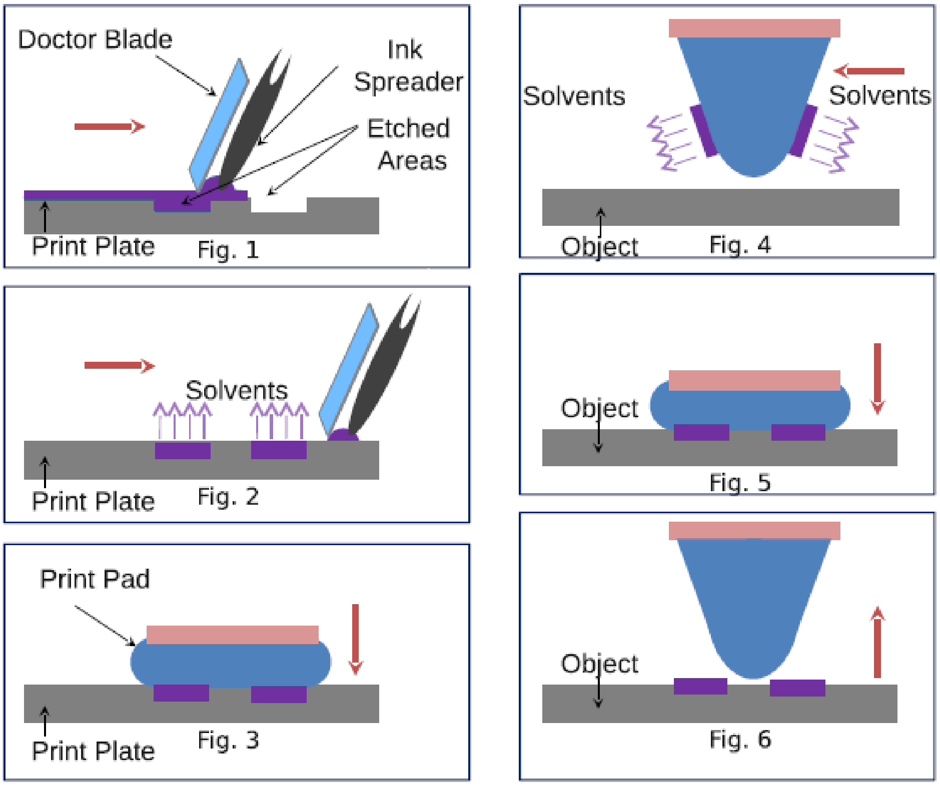

Figure 2-23: Schematic of a pad printing process

2.8.7 Laser transfer printing

The laser transfer printing system is a non-contact metallisation method jointly developed by Schmid and BASF in 2009 [98]. The schematic of the laser transfer printing method is shown in Figure 2-24. A transparent endless belt is coated with metal paste and a laser beam deposits the metal paste from the belt onto the silicon wafer. It is a contact-free digital process, designed for handling thin wafers.

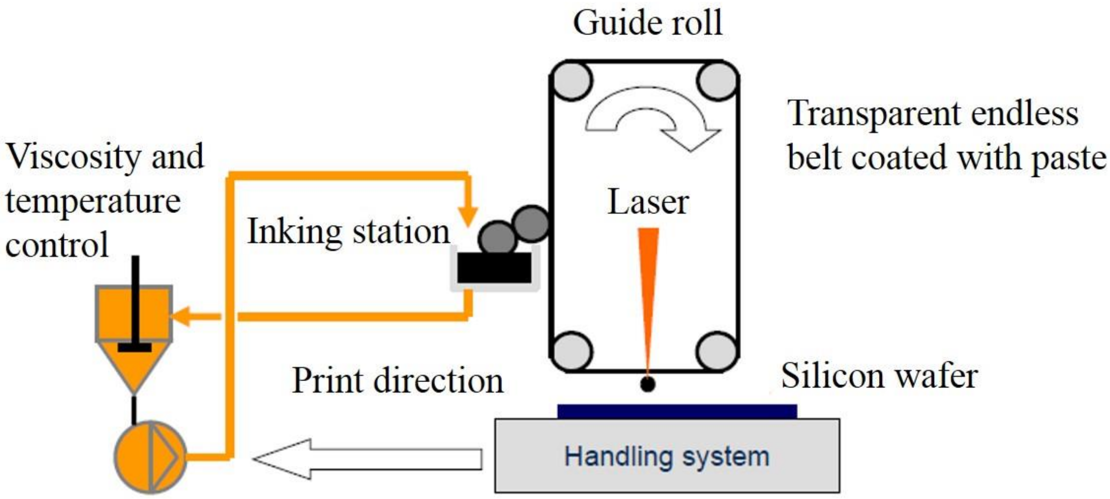

Figure 2-24: Schematic of a laser transfer printing process [98].

2.8.8 Pattern transfer printing

Pattern Transfer Printing (PTP) is a patented novel non-contact printing technology developed and commercialised by Utilight for advanced front side metallisation of silicon solar cells [99]. This is based on laser induced deposition from a polymer substrate and hence the geometry of the printed features is not restricted by the characteristics of the printing screen, and in turn allows much finer, higher and uniform fingers. The schematic drawing of the working principle of the PTP is shown in the Figure 2-25. This printing technology is based on two stages: 1) the filling of a transparent polymer substrate with pre-embossed trenches with paste and 2) the transfer of the paste pattern to the wafer surface using laser irradiation.

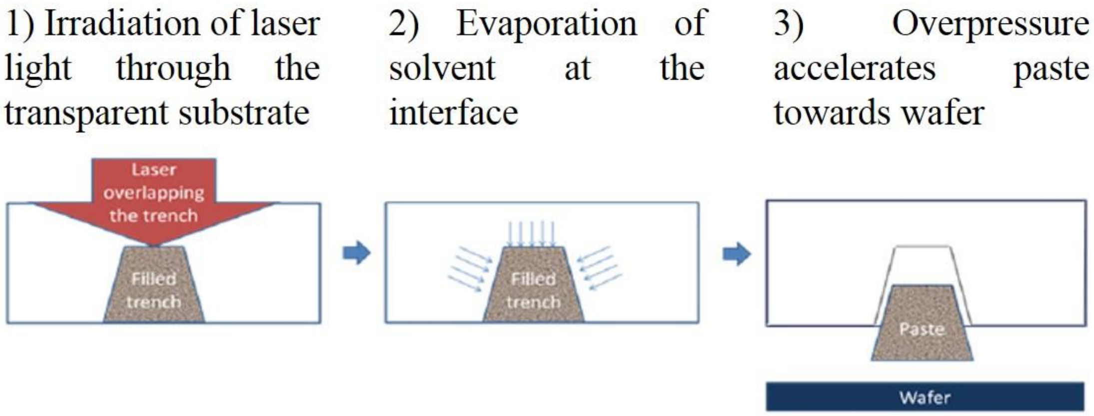

Figure 2-25: Working principle of the pattern transfer printing process [99].

Of the various available printed metallisation techniques, the primary focus in this thesis will be on screen printing. Primary challenges of fine-line printing associated with this metallisation method will be discussed and stencil printing is used as an alternative to overcome the fine-line printing limitations. This will be discussed in detail in Chapter 3. The other printed metallisation methods like inkjet, aerosol, flexographic, and pad printing methods are more suitable for printing metal seed layers (and not for full-height metal contacts).

Chapter 3: Experimental and simulation analysis of fine line screen and stencil printed metal contacts for silicon wafer solar cells[1]

3.1 Introduction

Screen printing technology is widely used by the PV industry due to its robust, simple and highly automated process. It remains the dominant production method thanks to rapid developments in metallisation pastes regarding line and contact resistance improvements. However its dominant position is constantly challenged by pressures within the PV industry to reduce costs by cutting down on silver (Ag) metal consumption. The ITRPV (International Technology Roadmap for PV) roadmap of 2014 shows that the current Ag paste consumption for a standard 156 mm x 156 mm *c-Si* wafer is around 100 mg/cell. This amount of Ag costs about 7 cents (US)/cell, making metallisation pastes the second most expensive material in the standard solar cell fabrication process after the silicon wafer [2]. The fundamental limitation of the screen printing process is its inability to print very fine lines with high aspect ratios and uniformity [100]. The screen consists of an aluminium frame, a mesh of stainless steel wires being clamped to the frame and an emulsion layer, which is photolithographically structured with the desired printing image. New developments in screen manufacturing have enabled finger widths of around 60 - 80 µm as a standard in production. For even finer lines with a width of less than 60 µm, a mesh with finer wires (more than 350 meshes per inch) and with high mesh separation distance is desired. However, the danger of screen breakage and screen clogging due to the paste particles increases strongly with reduced finger openings. Another problem with fine line screen printing is the transfer of the screen mesh pattern onto the printed lines, potentially resulting in undesirable striations [101]. This non-uniformity increases the resistance of the printed lines. The Ag

---

[1] Published as Vinodh Shanmugam et alia, “Analysis of fine-line screen and stencil printed metal contacts for silicon wafer solar cells”, *IEEE Journal of Photovoltaics,* volume 5, Issue 2, Mar 2015.

price is expected to remain high (> 15 USD per ounce) and hence it is of utmost importance to reduce the Ag consumption even further. As a result, metallisation using alternative methods like inkjet and plating are key areas of research[102]. Screen printer manufacturers are also responding to the price pressure by implementing changes to the traditional technology. One approach that is gaining popularity in the PV industry to reduce Ag usage is the dual print process[103]. Dual printing is a 2-print process where in the front busbars (*BB)* are printed first (using a separate screen and using a paste that is less aggressive on the SiN_x layer) followed by the second print where only fingers are printed using the conventional fire-through Ag paste to etch the SiN_x antireflection coating. The main advantage of this technique is that it helps in increasing the efficiency of the solar cells (by using *BB* pastes that are less aggressive and results in reduced metal recombination due to less damage to the passivation layer) and at the same time reduces the Ag consumption (the thickness of the *BB* can be reduced, as it is not required for the *BB* to be of the same thickness as that of the fingers) [104].

Stencil printing has emerged as a very promising candidate for the dual printing process [105]. Unlike screens with wire mesh, a stencil features 100% open area in the aperture (finger openings), which leads to an excellent paste transfer and printed line height uniformity when compared to a mesh screen open area of around 60% [103]. Typical stencil printed lines also have high aspect ratios independent of line width. Therefore stencil printing is very compatible with fine line printing down to line widths below 50 μm [106]. At the same time, stencil printing technology is only incrementally different from screen printing. It uses the same base equipment and pastes that are used for screen-printing applications, making it readily adoptable by cell manufacturers.

In this work, I used screens and stencils with different finger openings of 30, 45 and 60 μm to print on identically processed 156 mm × 156 mm *p*-type mono-Si wafers. The stencils used in this work were fabricated using the electroforming process [107]. The electroforming technology results in stencils with smooth, trapezoidal sidewalls which maximises paste release and enables fine line printing with uniform finger profile. Effect of the topography of printed Ag metal lines on its conductance and also its impact on the one-sun light I-V characteristics of the fabricated solar cells is reported. Using the 3D profile of the printed fingers along with line segment resistance measurements data, it will be shown that it is possible to develop a statistical model to predict the solar cell performance with different finger openings.

3.2 Experimental details

3.2.1 Sample preparation

All solar cells used in this study were made on large-area 239-cm^2 (156 mm × 156 mm) p-type pseudo-square mono-Si wafers with 1-3 Ωcm bulk resistivity. The wafers were saw damage etched and textured to generate a random pyramid surface texture on both sides. Phosphorus emitter diffusion was carried out using an industrial tube diffusion furnace, which resulted in a sheet resistance of about 80 Ω/sq. Following the diffusion process, a standard wet-chemical rear junction isolation and phosphosilicate glass (PSG) removal was performed. An amorphous silicon nitride (SiN_x) antireflection coating (ARC) was then deposited by plasma-enhanced chemical vapour deposition onto the front surface as an antireflection coating and passivation layer. The wafers were then metallised with a rear Ag busbar and rear Al. The front metallisation had an experimental split as shown in Figure 3-1. The front busbars were printed using commercially available Namics 331 paste, which does not fire through the ARC, using the same screen for all wafers whereas the front grids were printed using both stencils and conventional screens using DuPont PV17F Ag paste. The front grid design for different openings were optimised to ensure minimum power loss using GridSim [108]. A design with 30 µm openings has 108 fingers in total, for 45 µm openings the number of fingers is 95 and for 60 µm openings it is 85 fingers. These values were chosen using GridSim simulation to determine the optimal spacing between fingers such that the optical shading losses and electrical losses are minimised. Finally, all cells were fired at the same optimised firing profile. The printed metal lines in this work were characterized optically and electrically. 3D optical profiles of printed line segments were captured using the Zeta optical profiler system [47]. The optical profiler yields the 3D height information and the profile of the printed fingers with high resolution. The line conductance of the printed metal lines were measured from the fabricated solar cells. The measurements were done using four-wire method, on laser-cut pieces of the cell that do not include busbars (BB). The emitter conductance path between fingers on each piece was interrupted by means of scribing by a carbide tip. Transfer length method (TLM) was used to measure the specific contact resistance of the Ag paste to the emitter layer. One-sun current-voltage measurements of the finished solar cells were measured using a flash tester.

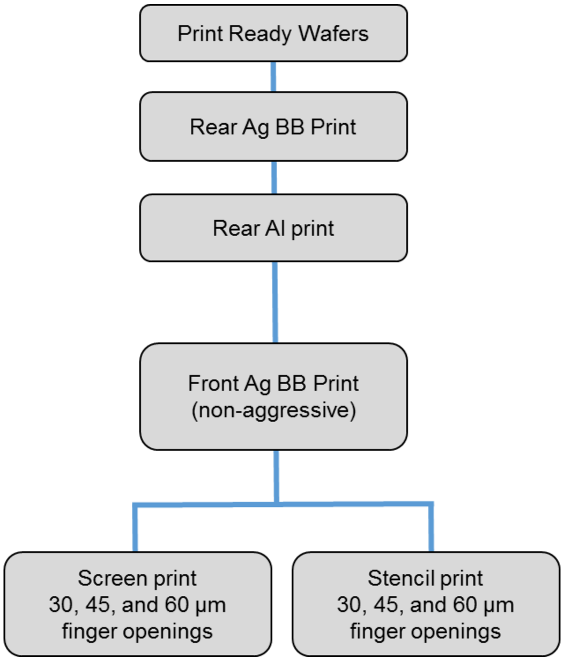

Figure 3-1: Cell metallisation experimental split. The drying step after each print process and the contact firing are not indicated in the process flow.

Table 3-1 indicates the geometrical properties of the screens that were used in this study. Stencils with different finger openings had the same number of fingers as their screen counterparts.

Table 3-1: Properties of the screens that were used in this study. The stencils with different finger openings had the same number of fingers as their screen counterparts.

Finger width (µm)	Number of fingers	Wire count (mesh per inch)	Wire diameter (µm)	Mesh thickness (um)	Emulsion thickness (µm)
30	108	380	14	26	14
45	95	350	16	23	22
60	85	325	24	35	25

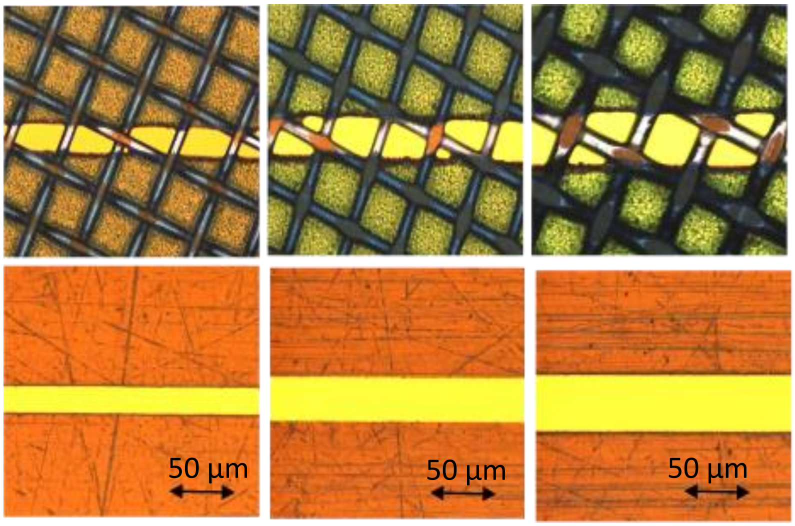

Figure 3-2: Optical microscopic images of the screen (top) and stencil (bottom) for different finger openings (30, 45 and 60 µm respectively).

Figure 3-2 shows the openings of screens and stencils for different line widths measured using an optical microscope. The line openings are well defined for stencils and are interfered by the mesh for the screens. This interference of the screen mesh will lead to a greater number of striations and finger breaks in the fine line screen-printed finger profile, as will be seen below.

3.3 Results and Discussion

3.3.1 Comparison of paste usage and cell performance

Table 3-2 shows the paste consumption for cells with the screen and stencil splits according to Figure 3-1. As expected, the Ag consumption lowers with decreasing the printed finger width.

Table 3-2: Ag paste consumption measured on the silicon wafers after printing

Printing method	Finger opening / Number of fingers		
	30 µm/108	45 µm/95	60 µm/85
Screen printed paste laydown (mg)	63 mg	106 mg	125 mg
Stencil printed paste laydown (mg)	78 mg	117 mg	137 mg

Figure *3-3* shows the results of the one-sun light *I-V* measurements on these solar cells measured using a flash tester. From the *I-V* parameters, it is noticeable that solar cells with stencil printed lines have a higher fill factor (*FF)* and conversion efficiency when compared to their screen printed counterparts. The highest short-circuit current density (J_{sc}) of 37.7 mA/cm^2 was achieved for solar cells with stencils-printed front metal lines. The highest batch solar cell efficiency of 18.8% was achieved for the solar cells that were stencil-printed with a 30 µm finger opening. Their screen printed counterparts had a significantly lower efficiency of 16.7% which was mainly due to a relatively poor *FF* of 71% which was limited by a very high series resistance. To rule out the possibility that the difference in series resistance is from different levels of contact resistance, the specific contact resistivity of the Ag paste to the emitter layer was measured using the transfer length method (TLM), and all cells regardless of their printing method yielded values around 3-6 mΩ cm^2, which is not significant enough to impact the *FF* by more than 2%. Hence the low *FF* for cells printed with 30 µm screen opening points strongly to the increase in the printed line resistance (arising due to non-continuous lines and due to the striations in the line profile). *I-V* results clearly indicates that the silver paste utilization in terms of line conductance is higher in the case of stencils when compared to the screens.

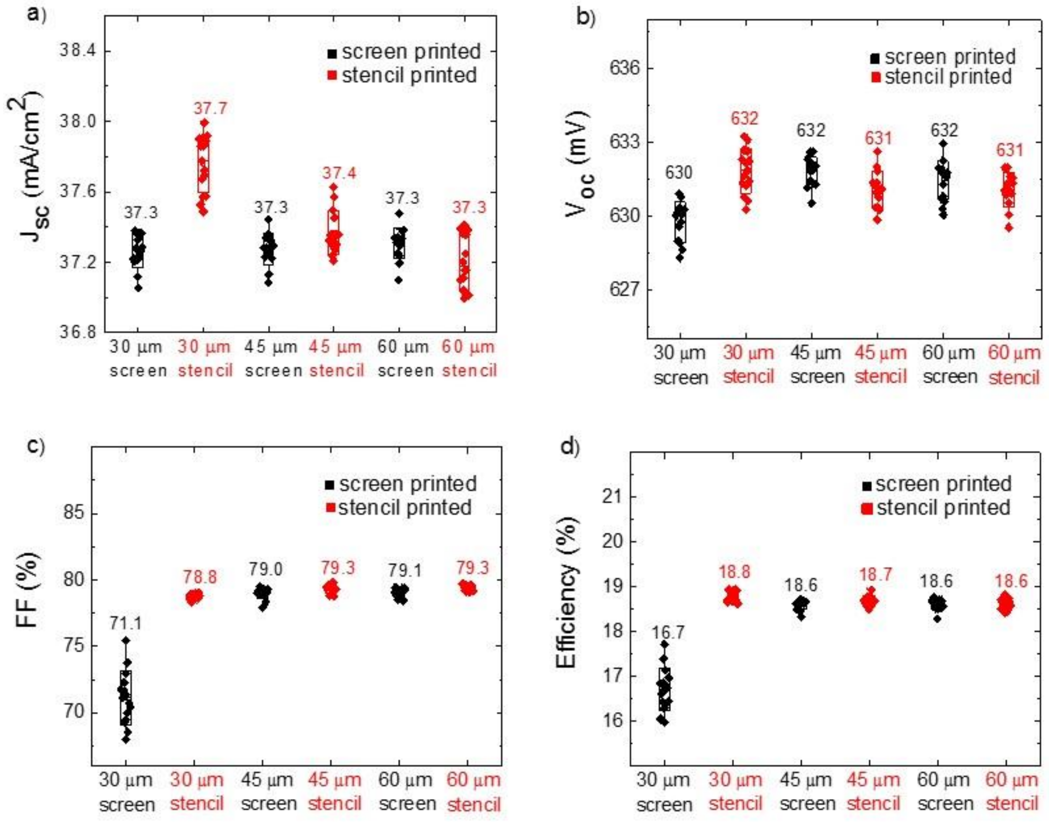

Figure 3-3: (a) Short-circuit current density, (b) Open-circuit voltage, (c) Fill Factor, and (d) Efficiency of solar cells printed with screens and stencils having different finger openings.

3.3.2 Line shape and resistance

The shapes of the printed metal fingers play a major role in the line resistance. Jiang *et alia* described the line uniformity by the so-called finger roughness [109], which assumed that the wire mesh of a screen creates a regular modulation in the metal line profile. In this work, no assumptions were made about the line shape, but instead attempted to infer statistical distributions to describe the line segment conductance in the cells. In order to do this, I rely on four types of data related to the finger shapes: 1) 3D optical profiles of short (250 um) segments; 2) line conductance of longer (1.5 cm) segments; 3) electroluminescence (EL) images of the cells, which gives a qualitative indication of the number of line breaks; 4) *I-V* parameters of the solar cell. A statistical distribution of line segment conductance that adequately describes the real situation must be consistent with all four data sets for each cell.

The shape of the printed metal lines were measured using Zeta optical profiler. As shown in Figure 3-4, the screen printed fingers have regular striations due to the screen mesh, leading to distinct peaks and valleys. On the other hand, the stencil printed fingers result in uniform distribution of the paste throughout the finger. For each cell, I measured close to 60 line segments (250 μm in length). The finite element analysis program Griddler [110] was used to simulate the conductivity of the printed line segments using the measure 3D profile data, assuming the silver paste bulk resistivity to be 2.6×10^{-6} Ωcm.

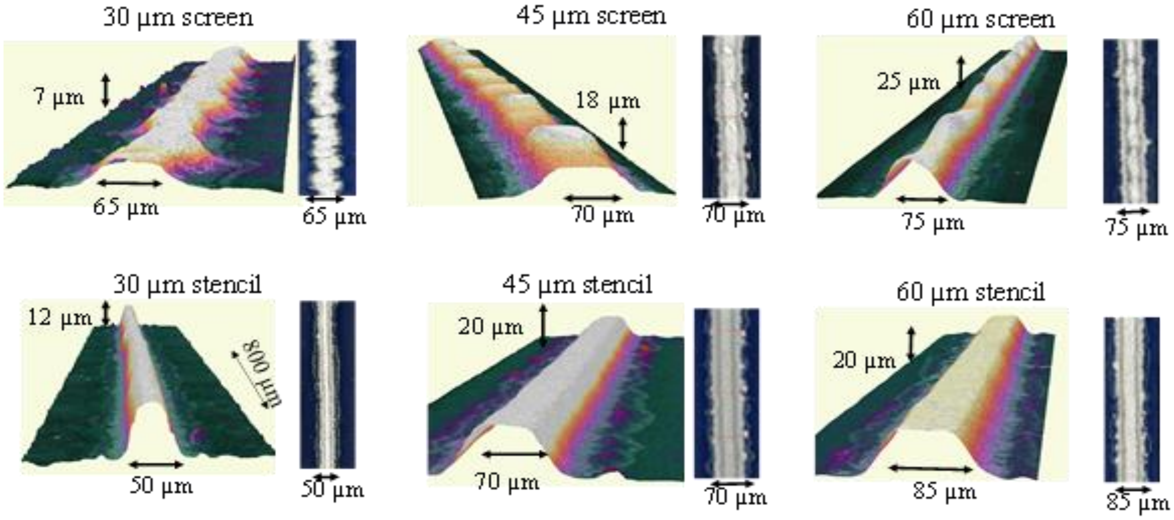

Figure 3-4. 3D profile and optical microscope image of the screen and stencil printed lines for different finger openings.

The printed metal lines were characterized by introducing a dimensionless factor known as the 'print quality factor'. The print quality factor is defined as the ratio of the conductivity of the actual printed line versus the conductivity if the Ag paste were distributed uniformly throughout the line. It is a calculated property derived from simulations of line conductance based on the line shape as given by the 3D profiles. The screen printed lines with narrowest finger openings of 30 μm have the lowest print quality factor of 69%, as shown in Figure 3-5. For the other openings and for stencils, the values are close to 100%. However, in the next section, it will be clear that even for lines with such high average print quality factor, the line segment conductance may follow a rather broad distribution that leads to finite probability of low conductance segments, which become ‘bottlenecks’ to current flow, thus noticeably impacting the cell fill factor. The print quality factor also does not reflect on the line width and aspect ratio, which are another two important parameters that play a role in shading loss and *FF*.

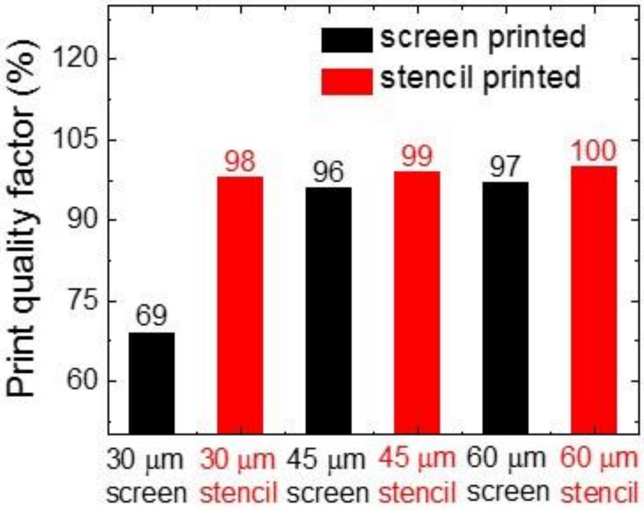

Figure 3-5: Average print quality factor for the screen and stencil printed lines.

The second set of data related to finger line shape are 1.5 cm segment line conductance measurements. Both the first data set (3D profiles and simulated short segment conductance) and second data set (actual measured conductance on longer segments) generate a wealth of statistics that will be the basis of building up a model distribution. The average and the standard deviation of the simulated line conductance values are shown in Table 3-3.

Table 3-3: Average and standard deviation of the conductance values of simulated short line segments and measured long line segments.

Finger opening		Conductivity (S cm)			
		Screen-printed lines		Stencil-printed lines	
		250 µm line segment (simulated)	1.5 cm line segment (measured)	250 µm line segment (simulated)	1.5 cm line segment (measured)
30 µm	Average	0.76	0.6	1.19	1.22
	Standard deviation	0.19	0.27	0.32	0.16
45 µm	Average	2.24	2.15	2.73	2.67
	Standard deviation	0.27	0.08	0.19	0.06
60 µm	Average	2.51	2.70	3.73	3.93
	Standard deviation	0.28	0.08	0.19	0.08

The measured conductivity of long segments can be fit using the conductivity of short segments. As every 1.5 cm line segment consists of 60 x 250 um short segments, its line conductivity σ_{long} (expressed in Ω^{-1}cm) can be written in terms of those of the constituting short segments $\sigma_{short,I}$ with i = 1 - 60:

$$\frac{1}{\sigma_{long}} = \frac{1}{60}\sum_{i=1}^{60}\frac{1}{\sigma_{short,i}} \tag{3.1}$$

Thus once the probability distribution P($\sigma_{short,i}$) of $\sigma_{short,I}$ is given, through equation 3.1, it is straightforward to simulate the distribution P(σ_{long}) by Monte Carlo methods [111]. As the sampling number for σ_{long} and $\sigma_{short,I}$ are low (about 70-80 measured data points), fitting of P(σ_{long}) and P($\sigma_{short,i}$) to the data histogram is not reliable because the histograms are inevitably coarse. A clearer representation of the data in a statistically meaningful way is to plot the sampled data in order of increasing value, as in Figure 3-6 for the case of the screen printed cell with 30µm screen finger opening. These plots are then fitted by the cumulative distribution functions of P(σ_{long}) and P($\sigma_{short,i}$) which are drawn as solid lines in the Figure 3-6. Figure 3-6 makes a good example to compare the fitting of two model distributions, one being the conventional Gaussian, and another being the Pareto distribution [112]as given by

$$P(\sigma_{short,i}) = \left(\frac{\sigma_{short,i}}{\sigma_{short,io}}\right)^{-\alpha} \qquad ; where\ \sigma_{short,i} \geq \sigma_{short,io}$$

$$= \left(\frac{2\sigma_{short,io} - \sigma_{short,i}}{\sigma_{short,io}}\right)^{-\alpha} \qquad ; where\ \sigma_{short,i} < \sigma_{short,io} \tag{3.2}$$

where $\sigma_{short,io}$ is the mean and α is a power law scaling factor. Note that negative values of $\sigma_{short,I}$ are admissible but are interpreted as zero. The smaller the scaling factor, the larger is the spread in the data. The Gaussian and the Pareto distributions are distinctly different in that the former has an exponentially decaying tail, and the latter has a 'heavy' power law tail. As can be seen in Figure 3-6, the Gaussian of best fit generates $P(\sigma_{short,i})$ that is significantly broader than the data, but underestimates the probability of near-zero σ_{long} compared to data. In contrast, the Pareto distribution is able to fit both $\sigma_{short,I}$ and σ_{long} well, including the peculiar jump in the σ_{long} data which reflects a bimodal distribution. As seen in the next section, it is also able to predict the number of line breaks and the impact on the cell FF reasonably well. Therefore, the Pareto distribution to each cell fitting is applied, and the statistical parameters of best fit are listed in Table 3-4.

Table 3-4: Mean conductivity and scaling factor α of Pareto distribution model for different finger opening screen and stencil printed lines.

Finger opening		Pareto distribution model	
		Screen printed lines	Stencil printed lines
30 µm	Mean xo (Scm)	0.83	1.26
	Scaling factor α	6	9
45µm	Mean xo(Scm)	2.27	2.67
	Scaling factor α	10	18
60µm	Mean xo(Scm)	2.72	3.92
	Scaling factor α	16	26

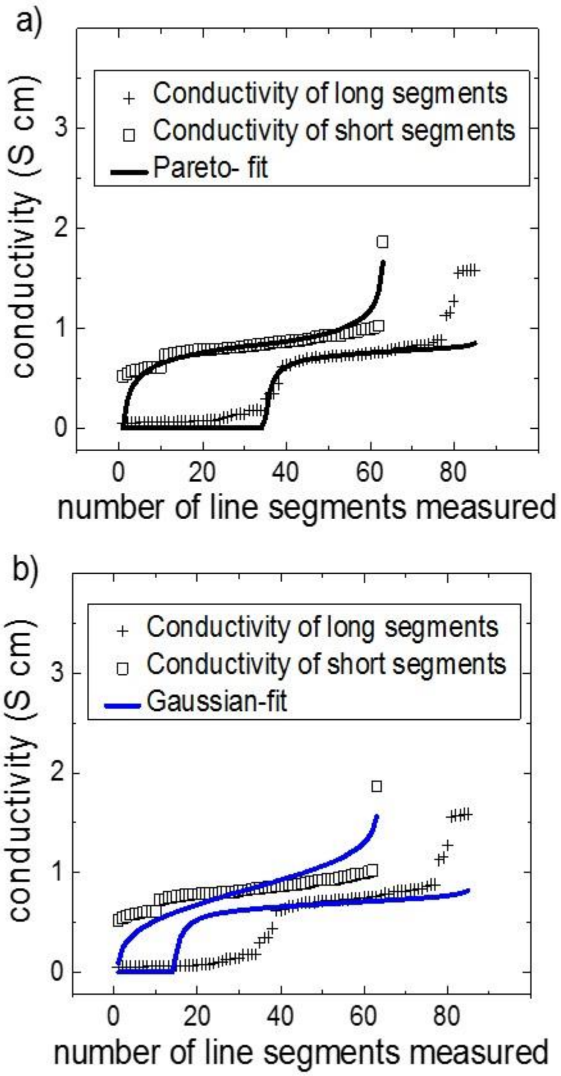

Figure 3-6: Cumulative distribution of conductivity of short and long line segments and their corresponding fit using a) Pareto distribution and b) Gaussian distribution. The x-axis represents the number of line segment measurement points.

3.3.3 Measured and simulated EL images

The Pareto statistical model of line conductance, and the parameters of Table 3-4 were used to simulate a realistic solar cell. This was done in the Griddler software [110], which constructs and solves the full two dimensional distributed network representation of the metallised solar cell using FEM (Finite Element Method). In Griddler, it is possible to define a realistic front grid pattern whose finger segment conductance is modulated in a pseudo-random manner according to the fitted Pareto distribution, and then simulate the voltage and current distributions along the cell plane at any illumination and bias conditions. By means of this simulation, Griddler is able to predict the *J-V* characteristics as well as the electroluminescence (EL) patterns of the realistic cells. Both the simulated EL images and *J-V* parameters match well with measurements (Figure 3-7 and Table 3-5).

Revisiting the Pareto distribution described in equation 3.2, the frequency of broken fingers can be found by evaluating the area under the curve where x is less than zero. The lower the scaling factor, the higher is this area and hence the occurrence of broken fingers. According to the best fit to 3D profile line shapes and line segment conductance measurements of Figure 3-4, the screen printed cells with 30 µm opening have the lowest scaling factor of 6. The corresponding Griddler simulation of the EL image shows numerous finger line breaks, which is in good qualitative agreement with the actual EL image when laid side by side. In contrast, the fitting to line shape and segment conductance for the stencil printed cells with 30 µm opening, has a higher scaling factor of 9. The resultant EL pattern has therefore a far more tolerable number of finger breaks.

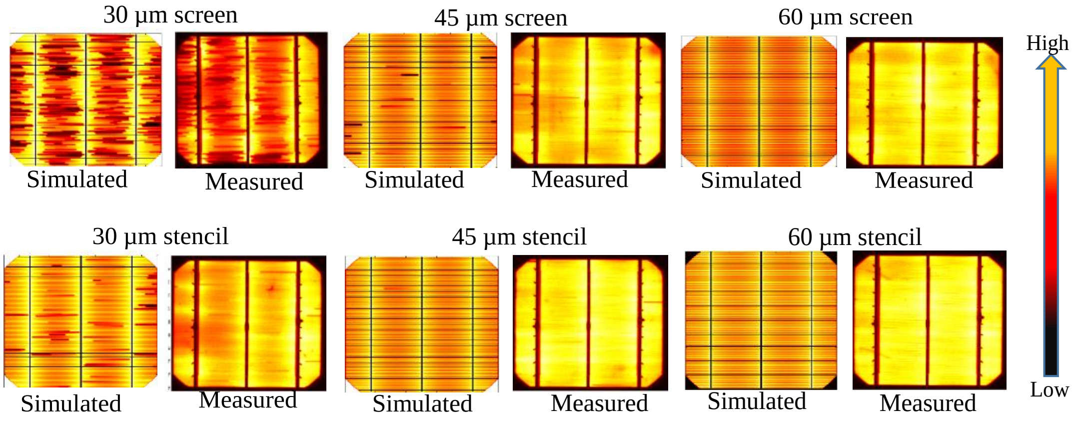

Figure 3-7: Simulated and measured EL images for screen and stencil printed cells with different finger openings. The scale bar represents the EL count.

The simulated and measured one-Sun *I-V* parameter for screen and stencil printed fingers are in good agreement as shown in Table 3-5. Note that all cells are assumed to be consisting of a network of diodes, whose characteristics is described by a two diode model with J_{01} = 730 fA/cm^2 and J_{02} = 30 nA/cm^2. All cells front grids are assumed to have the same specific contact resistance of 3 mΩcm^2. The only difference in the Griddler model of the different cells are in the mean value and statistical variation in the finger segment conductance, as described by the Pareto distribution with the parameters of Table 3-4. Therefore, the degree of agreement between the observed and simulated variations in *FF*, attests to the accuracy of the model distribution.

Table 3-5: Comparison of the simulated one-Sun I-V parameters based on the optical profile of the printed fingers with the average measured one-Sun I-V parameters.

Finger Opening/ Number of fingers	Simulated I-V parameters				Measured average *I-V* parameters			
	J_{sc} (mA/cm^2)	V_{oc} (mV)	*FF* (%)	η (%)	J_{sc} (mA/cm^2)	V_{oc} (mV)	*FF* (%)	η (%)
Screen-30 µm /108	37.3	630	73	17.1	37.3	629	71.1	16.7
Stencil-30 µm /108	37.8	631	78.3	18.7	37.7	632	78.8	18.8
Screen-45 µm /95	37.3	631	79	18.6	37.3	632	79.0	18.6
Stencil -45 µm /95	37.4	631	79.2	18.7	37.4	631	79.3	18.7
Screen -60 µm /85	37.3	631	78.9	18.6	37.3	632	79.1	18.6
Stencil -60 µm /85	37.3	631	79.2	18.6	37.3	631	79.3	18.6

3.3.4 Effective finger width of screen and stencil printed fingers on the cell and module levels

Grid shading optical losses at a cell level is roughly equal to the front grid metal coverage area fraction [113]. However, when the solar cell is enclosed in a module, light reflected from the printed metal fingers undergoes internal reflection at the glass-air interface [114, 115]. Light which is reflected at greater than the critical angle of approx. 42°, is totally internally reflected and impinges another time on the cell surface. As the metal finger cross sectional profile determines the angular distribution of scattering, the profile can be used to estimate the fraction of light that is reflected at the glass-air interface and redirected towards the cell. Therefore, based on the optical profile of the printed finger measurement both the shading on the cell level and the effective shading when encapsulated (module level) can be determined. For the module level shading, a simple simulation that traces the light incident on the metal finger, which is then scattered in a specular manner towards the glass-air interface was used. The internal reflectance of the each ray at this glass-air interface is then calculated using Fresnel equations, and the internally reflected component of light is assumed to be entirely absorbed by the cell. This way of simulation slightly underestimates the shading, because it neglects rays which hit the finger a second time after reflecting off the glass-air interface as well as rays that are absorbed by the metal fingers.

Figure 3-8 summarizes the 'effective width' of the fingers for the screen and stencil printed cells, after encapsulation into the module. Figure 3-9 estimates the shading on the cell and module levels (assuming that only fingers have an altered optical width in the module and not the wider busbars). Firstly, on the cell level, the shading losses estimated by Figure 3-9 agree quite well with the J_{sc} values in Figure 3-3. In the absence of shading, the cells should generate about 40.2 mA/cm^2.

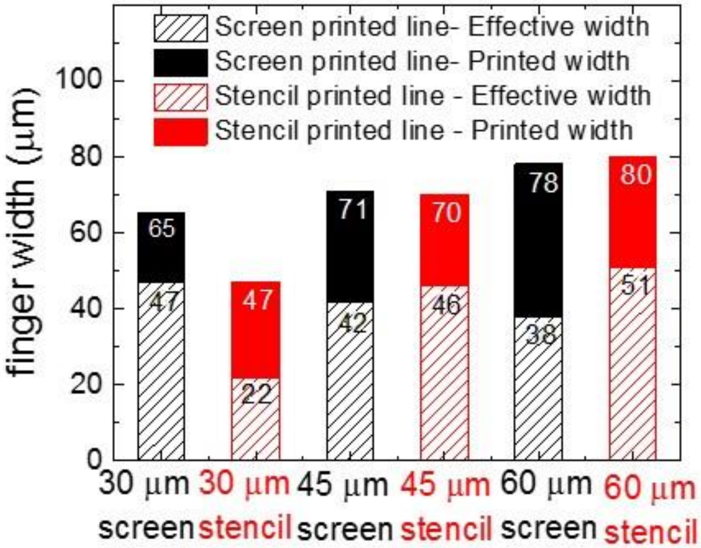

Figure 3-8: Printed line width and the effective width of the screen and stencil printed lines printed with different finger openings.

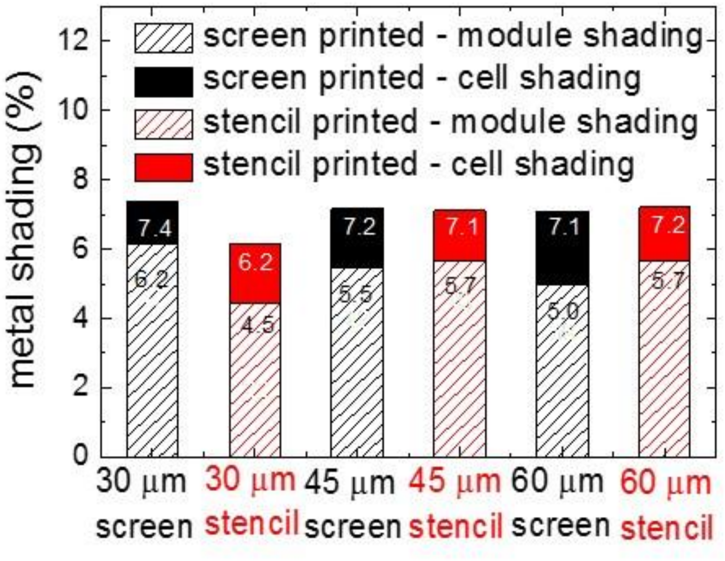

Figure 3-9: Measured cell level and simulated module level shading of the screen and stencil printed solar cells.

Based on the simulation and the measurements, it is evident that at 45 µm and 60 µm openings, stencil printed lines have less optical width reduction than the screen printed lines. This is because the wide stencil printed lines have a very rectangular profile (see Figure 3-4) when compared to the screen printed lines. Rectangular profiles tend to scatter light at near normal incidence to the glass-air interface, reducing the fraction of light which is internally reflected. On the contrary, at 30 µm opening, the trend is reversed and stencil printed lines have greater optical width reduction. This makes sense from the observation that as the finger width narrows, the stencil printed lines take on a round shape with high aspect ratio, while the screen printed lines become much flatter and low profile. Overall, stencil printed fingers also incur lower shading loss, on both cell and module levels, as the finger opening decreases to less than 45 µm.

3.4 Chapter summary

From both the perspectives of electrical (fill factor) and optical (shading and finger width narrowing) characteristics, it is obvious that stencil printed fingers are more suitable than screen printed fingers for fine line printing. At the lowest tested stencil finger opening of 30µm, the stencil printed lines are narrow

(47 µm) and have the ideal shape to benefit from significant optical width narrowing (to 22 µm) in a module. Meanwhile, the fingers have good aspect ratio and are very uniform, having a conductance of 98% compared to a perfectly uniform line. Cells printed using 30 µm stencil finger openings noticeably have higher short circuit current J_{sc} compared to rest of group, and is able to retain high fill factors. Moreover, the highest batch average efficiency of 18.8% were achieved on cells printed with stencils having 30 µm line openings, using only 78 mg of silver paste. Due to the good optical narrowing, the J_{sc} gain is expected to be even higher on a module level. In contrast, screen printed fingers at a screen opening of 30 µm, have unacceptable levels of finger breaks and low fill factor.

With the help of detailed survey of optical profile data, and line segment conductance measurements, I was able to construct a realistic distribution model of line segment conductance suitable for describing both the screen and stencil printed cells. Using the parameters of best fit, EL patterns and J-V parameters that closely resemble observed data were simulated. The optical profile data also derives finger widths that are consistent with the variation in J_{sc} observed between the groups of cells. The simulation gives confidence that the variations in cell level parameters observed, are indeed arising as a result of the different printing techniques and screen openings used in the study.

Chapter 4: Experimental analysis of contact formation to lightly doped phosphorus silicon surfaces by screen printing[2]

4.1 Introduction

Screen printing technology is the dominant metallisation process for industrial silicon wafer solar cells and is a well-established process for contacting phosphorus diffused (n^+) emitters on p-type Si wafers. Screen printed Ag pastes typically require a high phosphorus surface doping concentration to ensure a low-resistance ohmic contact. Industrial silicon wafer solar cells generally use phosphorus emitters with surface doping concentration above 5×10^{20} atoms/cm^3 to enable screen printed Ag metallisation contacts with low specific contact resistance. However, recombination losses in the emitter region increase with increasing phosphorus surface concentration [116]. A high phosphorus surface concentration results in a poor response to short wavelengths ("blue response") due to an increased Auger recombination in the emitter [117], [118]. Innovative Ag pastes have been developed to enable contacting phosphorus emitters with a lower surface doping concentration. This improves both the voltage (due to reduced heavy doping effects) and the current (due to improved blue response) of the solar cells.

In Si wafer solar cells, forming good contact between the emitter and the screen-printed Ag paste is essential to achieve high PV efficiency [119]. The Ag paste consists of Ag powder, glass frits and organic materials [120]. To establish a good contact with the diffused emitter, the screen printed Ag paste must etch through the insulating antireflection coating (ARC), typically silicon nitride (SiN_x), with minimum damage to the p-n junction [42]. The glass frits in the Ag paste melt during the firing process and then etch through the SiN_x layer to facilitate the formation of the electrical contact [121]. The organic materials in the paste act

---

[2] Published as Vinodh Shanmugam et alia, "Electrical and Microstructural analysis of the contact formation on lightly doped phosphorus emitters using thick film Ag screen printing pastes", *IEEE Journal of Photovoltaics,* Volume 4, Issue 1, Jan 2014.

as a carrier of the Ag powder and are responsible for the adhesion of the paste to the Si wafer during printing [42], [122].

Current transport through the screen-printed Ag/Si structure is relatively complex and several models have been proposed regarding its mechanism [57, 123]. The main reason for the complexity regarding the current transport mechanisms of the screen-printed contacts is the lateral non-uniformity of the contact, which is characterized by complex interfacial regions consisting of a resistive glassy layer, crystallites, colloids and pinholes. High series resistance is often a problem with screen-printed contacts on solar cells, which is mainly due to melted glass frits that flow preferentially towards the Ag-Si interface during the high-temperature (> 800 ºC) firing process. This creates an interfacial glass layer between the Ag contact and the Si which increases the contact resistance between the Ag and the Si, resulting in an increased series resistance of the solar cell. This interfacial glass layer is highly resistive (in the order of 10^9 Ωcm), and it prevents any electrical conduction through the glass to take place [123]. To date, two main conduction mechanisms have been proposed for screen-printed Ag contacts on Si. One model proposes that the current transport from the n+ silicon to the silver is not spatially uniform and occurs via a few isolated Ag crystallites that are directly connected, or in close proximity to, the Ag forming the bulk metal component of the contact [123]. The other model proposes electron tunnelling via nano-Ag colloids in the glass layer as the dominant current transport mechanism between the emitter and the Ag electrode [124]. The contact's microstructure changes with respect to the composition of the Ag paste. Recent studies show that the presence of direct contact between the silver electrode and the Ag crystallites grown into the silicon emitter reduces the contact resistivity by two orders of magnitude when compared to tunnelling via nano-Ag colloids present in the glass layer [57]. Though it is difficult to quantitatively determine the contribution from the different current transport mechanisms present in screen-printed Ag contacts on Si, qualitative measurements are possible [57]. The emitter diffusion profile can greatly influence the solar cell characteristics such as junction shunting, contact resistance, open-circuit voltage and short-wavelength response. Decreasing the phosphorus surface doping concentration leads to a higher specific contact resistance [125].

In this work, we analysed the contact formation process of two commercially available Ag pastes on phosphorus-doped emitters with active phosphorus concentrations ranging from 4.0×10^{20} to 1.7×10^{20} atoms/cm^3. The influence of the active phosphorus surface concentration on both the electrical properties and the contact formation process were investigated. Microstructural analysis of the contact formation process revealed that a high density of Ag crystallites with a very thin interfacial glass layer is required for contacting phosphorus emitters with low surface doping concentration. By tuning the emitter doping profiles and optimising the contact formation, PV efficiencies of up to 18.6 % were achieved on 156 mm × 156 mm p-type pseudo-square mono-Si solar cells.

4.2 Experimental details

4.2.1 Sample preparation

In this work, large-area 239-cm^2 (156 mm × 156 mm) p-type pseudo-square Cz mono-Si wafers with 1-3 Ωcm bulk resistivity were used. The wafers were saw damage etched and textured in KOH/IPA/potassium silicate solution at 80°C [126] to generate a random pyramid surface texture on both sides. The emitter diffusion was carried out using an industrial inline diffusion furnace (Despatch, DCF-3615), which has a doper section that feeds the wafers directly to a belt furnace for diffusion. After an atmospheric plasma pre-treatment step at the entry to the doper (to form a hydrophilic Si surface), a spray-on dopant source (a solution consisting of phosphoric acid and ethyl alcohol) was applied uniformly to both sides of the wafer, at a rate of 30 cm^3/minute. Following the diffusion process, a standard wet-chemical rear junction isolation and PSG removal step was performed in an industrial inline wet-chemical process tool (RENA, InPilot). Next, an emitter etch back process was applied using the so-called 'SERIS etch' [127] for different durations (120, 150 or 180 s) to achieve emitters with different surface doping concentration (4.0×10^{20}, 2.8×10^{20} and 1.7×10^{20} atoms/cm^3, respectively). An amorphous silicon nitride film was then deposited by PECVD (SiNA-XS, Roth & Rau) onto the front surface as an antireflection coating and passivation layer.

The cells were then metallized by screen printing using Al paste on the rear (MonoCrystal, PASE 12D) and Ag paste on the front (Sol 9411 or Sol 9600 obtained from HERAEUS materials). The cells did not receive rear Ag busbars. Finally, the front and rear contacts were co-fired in an industrial fast firing furnace (DESPATCH, Ultraflex). The inline-diffused emitters were characterized by 4 point probe (Napson) for sheet resistance measurements, electrochemical capacitance-voltage (WEP CVP 21) for dopant profile measurements, and implied V_{oc} and emitter saturation current density (J_{0e}) measurements. The implied V_{oc} was determined using the Suns-V_{oc} method [128], while the J_{0e} was determined using the Kane-Swanson method [129]. The specific contact resistance between the Ag pastes and the n^+ emitters was determined by the transfer length method. One-sun *I-V* measurements of the finished solar cells were measured using flash tester (Sinton FCT 350).

4.3 Results and Discussion

4.3.1 Emitter characterisation

The as-diffused emitter has a high active phosphorus surface concentration of 5×10^{20} atoms/cm^3. The heavily doped phosphorus layer at the surface results in increased carrier recombination losses, which reduces both the V_{oc} and the J_{sc} of the solar cell. However, after the emitter etch-back process the thickness of the heavily doped layer is significantly reduced (see Figure 4-1). The associated reduction in p-n junction depth, derived from the ECV profiles, is clearly evident for the three emitters (see Table 4-1). Furthermore, the implied V_{oc} and emitter saturation current density J_{0e}, also shown in Table 4-1, demonstrate a clear trend of a reduction in recombination (i.e. lower J_{0e} and higher implied V_{oc}) for the lower surface concentration emitters.

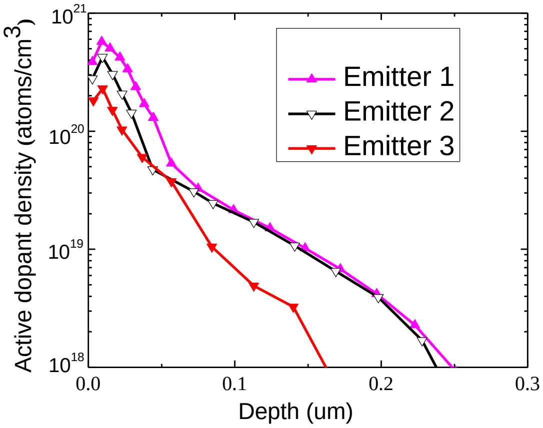

Figure 4-1: Active dopant profiles of inline-diffused emitters after etch back using the SERIS etch solution for different durations (120, 150 and 180 s), resulting in Emitter 1, Emitter 2 and Emitter 3, respectively.

Table 4-1: Characteristics of inline-diffused emitters after etch back using the SERIS etch solution for different durations (120, 150 and 180 s), resulting in Emitter 1, Emitter 2 and Emitter 3, respectively.

	As diffused	Emitter 1	Emitter 2	Emitter 3
Active phosphorus density (atoms/cm^3)	5×10^{20}	4×10^{20}	2.8×10^{20}	1.7×10^{20}
Junction depth (µm)	0.31	0.29	0.27	0.21
Ave. sheet resistance (Ω/□)	40	65	85	120
Sheet resistance uniformity (standard deviation) (Ω/□)	1.5	2.22	3.15	12.7
Implied V_{oc} at one-Sun (mV)	615	635	645	650
Emitter saturation current density J_{0e} (fA/cm^2)	240	156	142	120

4.3.2 Analysis of the contact formation

In order to study the contact formation mechanism of the two pastes (Sol 9411 and Sol 9600) to diffused emitters with different surface doping concentration, a microscopic analysis using scanning electron microscopy and focused ion beam imaging (FIB) was performed (Carl Zeiss, Auriga). For this analysis the contacts were etched sequentially using HNO_3/buffered HF/HNO_3 solutions [57]. Figure 4-2 presents FIB images of the Si-Ag interface of Emitter 1 for both of the pastes, fired at their respective optimized peak firing temperature as shown in Figure 4-3.

The SEM image (obtained after FIB milling) in Figure 4-2(a) clearly shows that a very thick and laterally continuous glass layer is formed when the Sol 9411 paste is used. As can be seen in Figure 4-2(b), only a very thin interfacial glass layer is formed when the Sol 9600 paste is used, resulting in more direct contact between the silver finger and the Ag crystallites grown in to the Si emitter, giving excellent cell fill factors (FF) of over 80 % (see Figure 4-3).

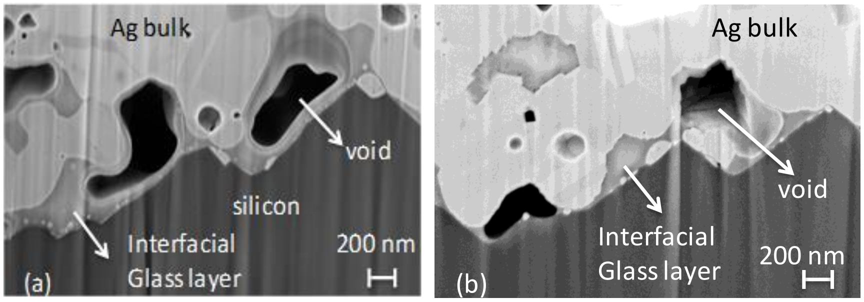

Figure 4-2: (a) SEM image of the Si-Ag interface (Sol 9411 paste, E1 emitter). A thick interfacial glass layer (maximum thickness of around 500 nm) exists between the bulk Ag and the underlying Si. (b) SEM image of the Si-Ag interface (Sol 9600 paste, E1 emitter). The presence of a thin (maximum thickness of around 150 nm) and a discontinuous interfacial glass layer results in more direct contact between the Ag crystallites grown into the Si emitter and the bulk silver finger, resulting in high fill factors of over 80%.

Figure 4-3 presents the fill factor (FF) of the Emitter E1 samples obtained as a function of the peak firing temperature. The peak firing temperatures were recorded using a DataPaq data logger with a K-type thermocouple soldered onto a metal plate. It can be seen that the Sol 9411 paste has a narrower firing window than the Sol 9600 paste. The optimum firing temperature was defined as the temperature at which both the lowest specific contact resistances and highest fill factors were achieved. It was found that the Sol 9600 performs best at temperatures between 800 ºC to 850 ºC (and all cells metallised with Sol 9600 were fired at a peak temperature of 850 ºC) whereas Sol 9411 paste performs best for a peak firing temperature of 795 ºC. At temperatures below and above this value of 795 ºC, the cells metallised with Sol 9411 paste were series resistance limited. This is due to the impact of the firing temperature on the glass layer thickness [130] and the growth of Ag crystallites [131]. It was found that the growth rate of the glass layer is enhanced at higher firing temperatures [130], leading to higher contact resistance values.

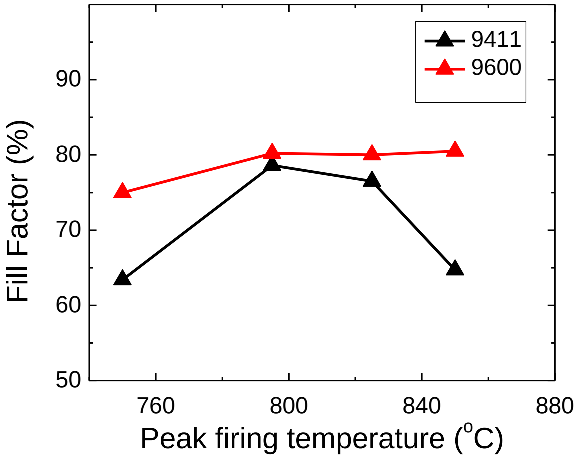

Figure 4-3: Fill factor as a function of the peak firing temperature.

The transfer length method (TLM) with a circular pattern [132] was used to determine the specific contact resistance between the Ag pastes and the n^+ emitter. The TLM samples were printed on 'print-ready' wafers (textured, diffused emitter and silicon nitride coated) and fired at the optimised firing profile. The contact resistivity results of Figure 4-4 indicate that the Sol 9600 paste is capable of contacting each of the three investigated emitters. However, the Sol 9411 paste did not create good ohmic contacts for the lower surface doping concentrations, and was only able to form an ohmic contact to the highly doped emitter (4×10^{20} phosphorus atoms/cm^3 at the surface), with a reasonable contact resistivity of about 5 mΩcm^2. Notably, the Sol 9600 paste was able to contact the lower surface concentration emitter (surface concentration of 1.7×10^{20} atoms/cm^3) while maintaining a reasonable contact resistivity of about 5 mΩcm^2.

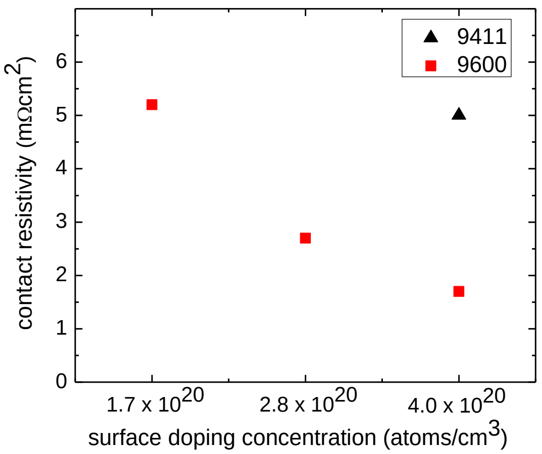

Figure 4-4: Contact resistivity (determined by TLM) as a function of phosphorus surface concentration of the n$^+$ emitter. The Sol 9411 paste was unable to form an ohmic contact to the lower surface concentration emitters and hence no specific contact resistance values could be measured.

Representative samples from the Emitter E1 and E3 sub-groups (i.e. highest and lowest surface concentrations) were selected for SEM investigation of the growth of the Ag crystallites. Prior to the SEM analysis, the contacts were wet-chemically etched off by immersing the samples into HNO_3, then buffered HF, and then again HNO_3. Figure 4-5a) and Figure 4-5(b) show the crystallite imprints of the Sol 9411 paste on sample E1 (surface concentration 4.0×10^{20} atoms/cm^3, junction depth 0.29 µm) and sample E3 (surface concentration 1.7×10^{20} atoms/cm^3, junction depth 0.21 µm), respectively. Ag crystallite imprints were seen at the tips of the pyramids for Emitter E1 samples and the amount of Ag crystallites decreased with respect to the emitter surface doping concentration. Based on the SEM image, the non-ohmic contact of the Sol 9411 paste on the lower surface concentration emitter (Emitter E3) can be explained by the lack of Ag crystallite imprints.

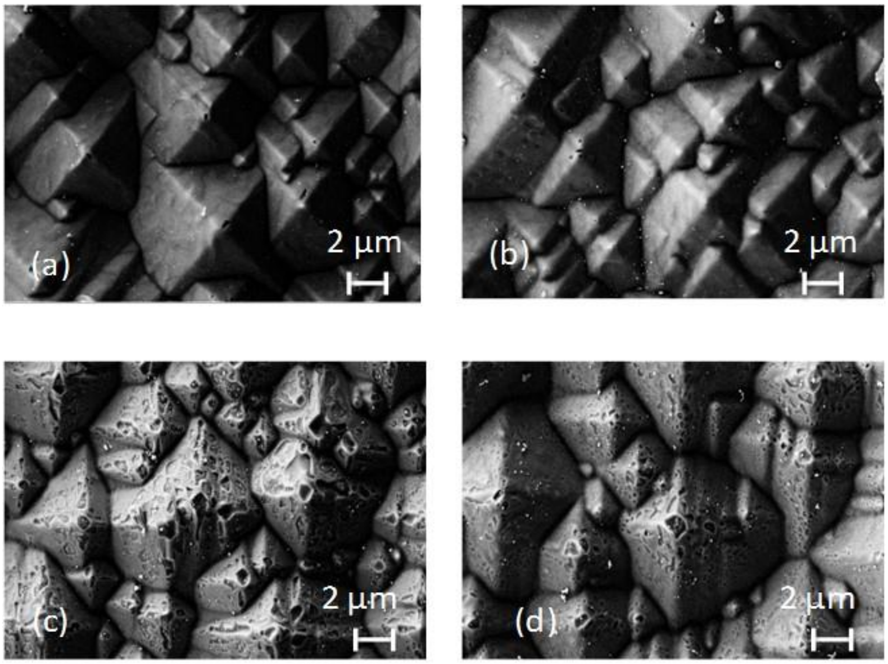

Figure 4-5. SEM micrographs of (a) Ag crystallite imprints of paste 9411 on Emitter E1 (surface concentration 4.0×10^{20} *atoms/cm*^{3}*, junction depth 0.29 µm). (b) Ag crystallite imprints of paste 9411 on Emitter E3 (surface concentration* 1.7×10^{20} *atoms/cm*^{3}*, junction depth 0.21 µm). (c) Ag crystallite imprints of paste 9600 on Emitter E1 (surface concentration* 4.0×10^{20} *atoms/cm*^{3}*, junction depth 0.29 µm). (d) Ag crystallite imprints of paste 9600 on Emitter E3 (surface concentration* 1.7×10^{20} *atoms/cm*^{3}*, junction depth 0.21 µm).*

Figure 4-5(c) and Figure 4-5(d) show the crystallite imprints of Sol 9600 paste on Emitter E1 and Emitter E3, respectively. The depth and size of the crystallites formed with the Sol 9600 paste are much bigger than for the Sol 9411 paste, indicating a higher level of direct contact between the Ag paste and the emitter. The growth of the Ag crystallites still depends on the surface concentration of the diffused emitter, with a lower crystallite density observed for the emitter with lower surface concentration.

4.3.3 One-sun current-voltage measurements

To complete the solar cell fabrication process, the rear contact was formed using a standard Al paste (MonoCrystal, PASE 12D). Ag paste Sol 9411 was used as the front contact for one batch of cells and Ag paste Sol 9600 was used for the remaining ells. The cells were then fired at the optimized firing profile (obtained for E1 emitter, as shown in Figure 4-3). Figure 4-6(a) presents the average J_{sc} as a function of the emitter surface concentration. It can be seen that reducing the surface concentration tends to increase the

J_{sc} for cells metallized with the Sol 9600 paste but the J_{sc} for cells metallized with the Sol 9411 paste drops due to high specific contact resistance of this Ag paste to emitters with lower surface concentration. Figure 4-6(b) presents the average V_{oc} as a function of the emitter surface concentration. The V_{oc} tends to increase with reduction in the emitter surface concentration. However the drop in V_{oc} of cells for the E3 emitter group (surface concentration 1.7×10^{20} atoms/cm^3, junction depth 0.21 µm) is attributed to the drop in the cells' shunt resistance. The drop in the cells' shunt resistance for the E3 emitter solar cell group could be due to the fact that the firing profile used was not optimal for shallower p-n junctions. The highest average efficiency of 18.5% was achieved with the E2 emitter group (surface concentration 2.8×10^{20} atoms/cm^3, junction depth 0.27 µm) when metallized with the Sol 9600 paste. The highest cell efficiency achieved in this study was 18.6% (also the E2 emitter group), see Figure 4-7.

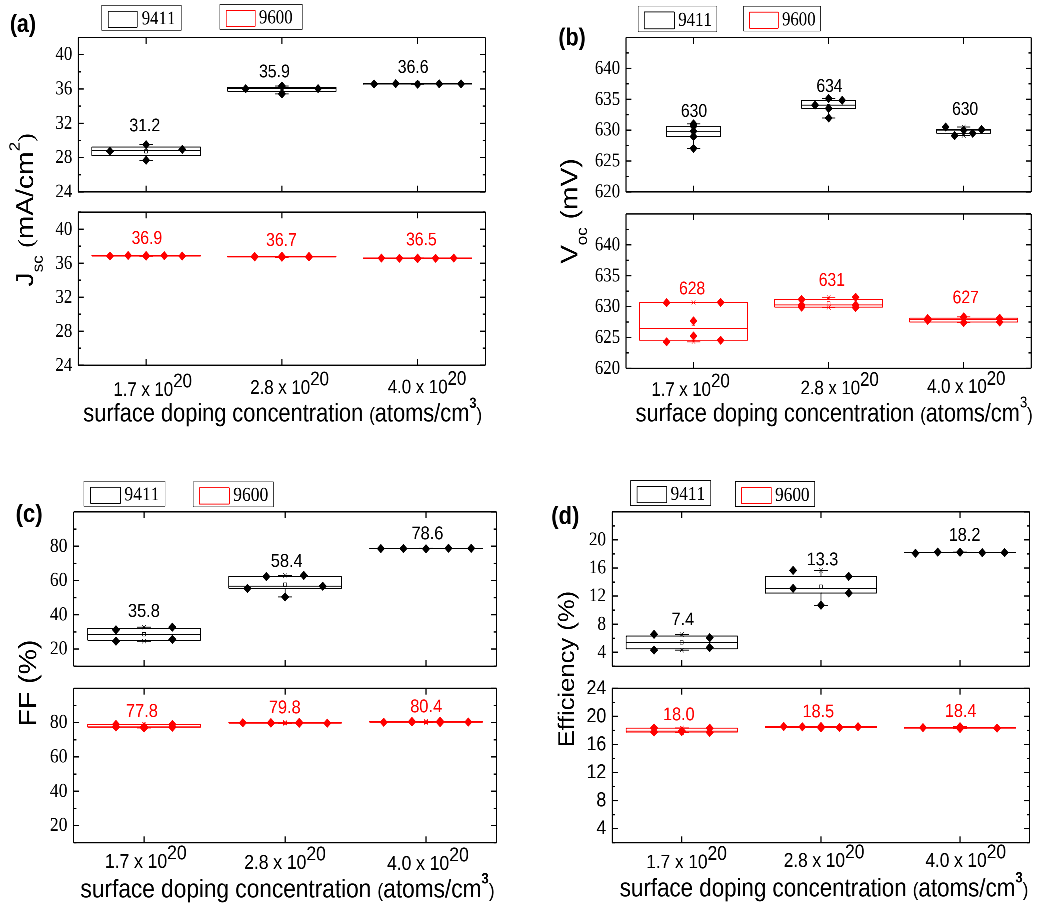

Figure 4-6: Measured emitter surface doping concentration dependence of (a) average short-circuit current density, (b) average open-circuit voltage, (c) average FF and (d) average efficiency.

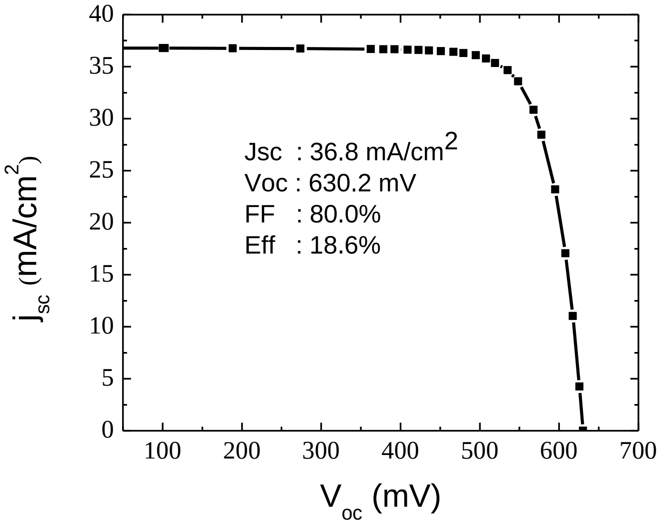

Figure 4-7: One-sun I-V curve of the best cell (E2 emitter group metallized with the Sol 9600 paste).

4.3.4 Fill Factor loss analysis

The average V_{oc} of cells metallised with Sol 9600 Ag paste is consistently 3 mV lower than cells metallised with Sol 9411 Ag paste for all the three emitters studied (as shown in Figure 4-6 b). To investigate this further we performed a detailed FF loss analysis to quantify the influence of resistive (series and shunt) and recombination losses on the FF. As the cells were processed identically with the only difference being the front metallisation paste, the results of the FF loss analysis can be used to infer the influence of the paste. The key difference between the pastes in our investigations is the crystallite depth. Sol 9600 results in bigger and deeper Ag crystallite imprints when compared to Sol 9411(as shown in Figure 4-5). This is likely to provide lower resistance contacts but the deeper contacts may increase space charge region recombination. A recent study has shown that metallisation pastes can have a significant influence on space charge region recombination [133]. Representative samples from Emitter 1 (surface concentration 4.0×10^{20} atoms/cm^3, junction depth 0.29 µm) metallised with Sol 9411 and Sol 9600 are taken for detailed FF loss analysis to quantify and compare resistive (series and shunt) and recombination losses for the two pastes. The parameters used for computing FF losses are summarised in Table 4-2. The I-V parameters were measured using a one-Sun flash tester (Sinton FCT 350 flash tester). Additionally the flash tester also determines the pseudo I-V curve (from Suns V_{oc} [61]) and the series resistance at the maximum power point (mpp) is calculated by the shift between the one-sun I-V and the Suns V_{oc} curve at mpp [61]. R_{sh} is calculated by fitting the pseudo I-V curve in the range 0-400 mV.

The method described in [134] based on the two-diode model of solar cells (symbols used in subsequent text: diodes with saturation current densities J_{01}, J_{02}, series resistance R_s, shunt resistance R_{sh}) is used to quantify the FF losses attributed to Rs, R_{sh} and J_{02}. FF_{J01} is the upper limit of FF assuming the absence of R_s, R_{sh} and J_{02} recombination [135]. The symbols in the FF loss analysis section of Table 4-2 ΔFF_{Rs}, ΔFF_{Rsh} and ΔFF_{J02} refer to the loss in FF due to R_s, R_{sh} and J_{02} respectively.

Table 4-2: One-sun J-V data and fill factor loss analysis results for cells metallised with Sol 9411 and Sol 9600.

Cell parameters									FF loss analysis results			
Metal paste	V_{oc} (mV)	J_{sc} (mA/cm^2)	FF (%)	Eff. (%)	V_{mpp} (mV)	J_{mpp} (mA/cm^2)	R_s at MPP (Ωcm^2)	R_{sh} (Ωcm^2)	FF_{J01} (%)	ΔFF_{Rs} (% absolute)	ΔFF_{Rsh}	ΔFF_{J02}
Sol 9411	632	36.7	78.7	18.3	530	34.4	0.82	3.8K	83.5	**4.2**	**0.4**	**0.2**
Sol 9600	628	36.6	79.9	18.4	532	34.6	0.53	3.9K	83.4	**2.8**	**0.3**	**0.4**

Based on the results of the FF loss analysis (as shown in Table 4-2), it is clear that Sol 9600 achieves higher FF than Sol 9411 because of significantly lower ΔFF_{Rs} (2.8% absolute for 9600 compared to 4.2% absolute for 9411). This is consistent with the much lower contact resistance measured with 9600 (as shown in Figure 4-4) and the deeper and bigger crystallite imprints (as shown in Figure 4-5). On interpreting the difference in ΔFF_{J02} loss terms with regards to the paste it follows that Sol 9600 leads to slightly increased J_{02} recombination over Sol 9411 (ΔFF_{J02} of 0.4% absolute instead of 0.2% absolute). This may be due to deeper crystallites formed as a result of higher peak firing temperature used for Sol 9600. However the crystallite depth is not severe enough to cause ohmic shunting as is clear from the comparable shunt resistance losses for cells metallised with both pastes. Increased J_{02} recombination also has a small influence on V_{oc} [134], this is again consistent with a V_{oc} drop of 3 mV for Sol 9600.

Interestingly, the marginal increase in recombination losses (evident form a comparison of delta FF_{j02} and V_{oc}) for cells metallised with paste Sol 9600 are strongly compensated by a significant decrease in series resistive losses for paste Sol 9600, leading to higher efficiency solar cells than the cells metallised with paste Sol 9411.

4.4 Conclusion

In this chapter, the electrical and micro-structural properties of screen-printed contacts formed with two different Ag screen printing pastes (Sol 9411 and Sol 9600) on phosphorus diffused silicon emitters with different surface doping concentrations and emitter depths were investigated. Theoretically, emitters with lower surface doping concentration are preferable due to reduced emitter saturation current density, which results in higher V_{oc} and J_{sc} (and thus PV efficiency). However, these benefits can only be reaped experimentally with screen-printed contacts if the pastes are able to contact the more lightly doped n^+ surface. The experiments showed that, compared to the Sol 9411 paste, the Sol 9600 paste produces bigger and deeper Ag crystallites with a thin and discontinuous glass layer. This results in more direct contact between the Ag crystallites grown in the Si emitter and the silver electrode and thus results in a better specific contact resistance. A low-resistance ohmic contact was demonstrated for phosphorus emitters with a surface doping concentration as low as 1.7×10^{20} atoms/cm^3. The best PV efficiency (18.6 %) was obtained for an intermediate surface dopant concentration of 2.8×10^{20} atoms/cm^3.

Chapter 5: Characterization of recombination at the metal silicon interface using photoluminescence imaging[3]

5.1 Introduction

Metallisation of phosphorus diffused emitters using screen printing Ag pastes is a well-established process for industrial silicon wafer solar cells [136]. Front-side Ag contact to the phosphorus diffused emitters is a key area of research, as it has a large impact on the cell efficiency and incurs significant production cost [2]. Metal contacts introduce significant recombination via the high interface defect density and the emitter damage caused by the high-temperature firing step. Both this metal contact recombination, as well as the electrical resistance of the contacts, are important factors in the optimization problem of the phosphorus diffused emitter profile [36]. Aside from the issue of contact quality, shallow emitters are more prone to junction shunting and increased recombination losses introduced by the metallisation process than emitters with deeper junction. Hence the optimal diffused emitter for an industrial silicon wafer solar cell has a significantly heavier diffusion and lower sheet resistance than one which minimizes the emitter saturation current density (J_{0e}), although the recent vast improvements in silver paste technology are enabling a trend towards higher emitter sheet resistance [36, 137].

There are several notable studies in recent years reporting on the recombination losses associated with metallisation based on specially designed experiments [138-140], [141]. Fellmeth *et al.* prepared samples each consisting of eight 2 cm × 2 cm solar cells of varying metal contact fractions F_M (F_M is the ratio of area of metallised regions to the total area of solar cell) on the same wafer [138]. By measuring the one-sun V_{oc} of each cell and extracting the dark saturation current density J_{01} via the one-diode model, plots of J_{01}

---

[3] Published as Vinodh Shanmugam et alia, “Determination of metal contact recombination parameters for silicon wafer solar cells by photoluminescence imaging”, *Solar Energy Journal,* Volume 118, pp 20-27, May 2015.

versus F_M were constructed from which the slope from linear fits yielded the metal contact contribution $J_{0e\text{-metal}}$. Hoenig *et al*. printed full metal grid patterns on 156 mm × 156 mm wafers, with additional interrupted contact fingers between the fingers of the base grid [139]. They observed a clear rise in FF_0 - pFF, the difference between the ideal fill factor FF_0 and the pseudo fill factor pFF (pFF is only influenced by recombination and shunting effects and it is an useful parameter to evaluate the non-series resistance related limitation of a solar cells fill factor), as the coverage of the interrupted contact fingers increased. Edler *et al.* studied both metal recombination at the phosphorus and boron diffused layers in bifacial solar cells [140]. In this case, the difference between the finished cell V_{oc} and the implied V_{oc} determined from lifetime measurements on the samples prior to metallization was tracked as a function of the metal contact fractions on the emitter (boron) and back-surface-field (phosphorus) sides of the cell. It is interesting to note that while references [138] and [140] observe near-unity ideality factor and good conformity to the one-diode model for their samples, with V_{oc} being the parameter that clearly changed with increasing metal contact fraction, reference [139] focuses on FF_0 - pFF, which seems to imply that it is the ideality factor rather than V_{oc} that changes most obviously with metal contact fraction in their samples. It is not clear whether this difference in observation arises from the different metal test structure patterns used by the different groups, or from a difference in the metal paste tested.

In this work, the use of PL imaging on simple-to-prepare screen printed silicon cells with special test patterns, which defines different regions-of-interest on a wafer with varying metal contact fractions is investigated. Like reference [138], only one screen is needed to print all eight different regions of interest. The added advantage related to analysis by PL imaging is that it is a contactless technique, so that automation of the test routine can be simply accomplished without having to design a dedicated test jig with precision alignment probes. Additionally, with the help of detailed finite element method (FEM) based simulation, which accounts for lateral balancing currents along the wafer that has a non-uniform voltage distribution, the possibility of forgoing any efforts to isolate the regions of interest from one another, thus saving many processing steps and making the test pattern cells as easy to prepare as a standard solar cell is also investigated. The simplicity of the experiment makes it conceivable to be implemented in a production environment, where a small fraction (e.g. one per 30 minutes, which is less than < 0.1%) of the processed wafers can be diverted to an offline printer to produce the test structures, so that the metal recombination parameters can be tracked over time to aid process control and design of experiments.

5.2 Methodology

The PL based method described in this work, for the extraction of recombination parameters at the metal-silicon interface, requires measurements on both a finished solar cell (wafer with an H-pattern front grid) and a wafer printed with the special test pattern as shown in Figure 5-1. Both patterns are printed on large-area (239 cm^2) 156 mm × 156 mm *p*-type pseudo-square Cz silicon wafers having the standard Al-BSF solar cell architecture. As shown in Figure 5-1 (a), the test pattern defines 8 mini cells (regions of interest) with metal fraction varying from 0 to 27%, by virtue of different nominal metal line widths ranging from 0 to 280 µm. The H-pattern in Figure 5-1(b) defines a standard 3-busbar solar cell with about 7% metal contact fraction. Both the test pattern and the H pattern have the same finger pitch of 1.8 mm.

Figure 5-2 shows the process flow and experimental split. Silicon wafers with 1-3 Ωcm bulk resistivity were saw damage etched and textured to generate a random-pyramid surface on both sides. Phosphorus emitter diffusion was carried out using an industrial tube diffusion furnace, which resulted in a sheet resistance of 80 Ω/square on both wafer surfaces. Following the diffusion process, phosphorus silicate glass (PSG) removal was performed. SiN_x antireflection coating was then deposited by PECVD onto the front surface as an antireflection coating and passivation layer. All wafers were then metallized with full-area Al on the rear (Monocrystal, PASE 12D) and Ag paste (DuPont, PV 18) on the front for the test pattern or H pattern. Finally, all cells were fired at the optimized firing profile, and then edge isolated using a laser with nanosecond pulses.

As the mini-cells' regions of interest in the test pattern are small and not cut out of the wafer, their boundaries play a significant role in both the local open-circuit voltage V_{oc} and the ideality factor *m*. If the boundary of each region contains a physical disruption, such as an emitter laser isolation, then the boundary may introduce a large and varying edge recombination component that tends to lower the V_{oc} and raise the ideality factor of each region. On the other hand, if the boundary contains no disruption such that it is only an imaginary demarcation line, then lateral balancing current may flow in and out of each cell, which tends to raise the V_{oc} and lower the ideality factor. In either case the boundary may introduce significant bias to the result. Three kinds of boundaries were experimented with for the mini-cells: 1) passivated iso-lines (where the laser lines isolating the mini-cells are treated to minimize recombination), 2) unpassivated iso-lines, 3) no iso-line (imaginary demarcation lines). Of the three types of boundary treatments, it was found that the no iso-line approach was the most reproducible and amenable to analysis, given that the analysis method can adequately account for the lateral balancing currents across the boundaries. Obviously, the no iso-line samples are also by far the simplest to fabricate. For these reasons, in the next sections the focus will solely be on this type of sample. In contrast, to create passivated iso-lines, the print ready wafers were first laser edge isolated at the intended boundaries of the mini-cells. Then the wafers were dipped in KOH at 80^{o}C for 2 minutes to remove the laser damage at the scribes. The masking silicon nitride layer was then removed, and the entire wafer was then re-passivated with a new silicon nitride film. For test structures with unpassivated iso-lines, the wafers were simply subjected to laser isolation around the edges of mini-cells after printing but, as will be seen, the laser damage is so great that the data is obscured by the recombination it introduces.

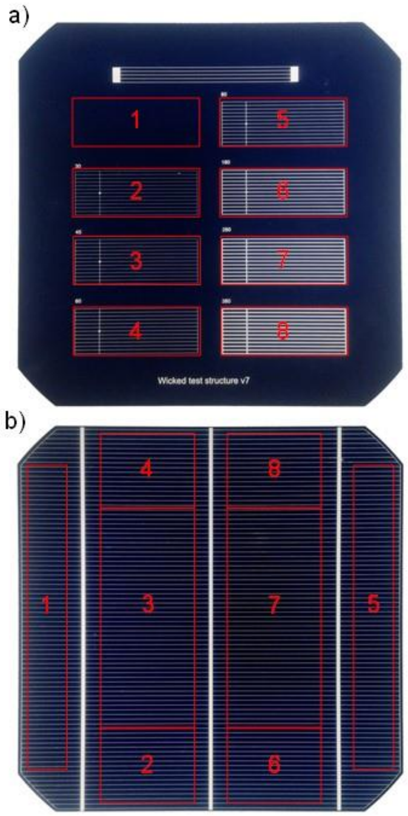

Figure 5-1: (a) Scan of the test pattern used in this work. The red boxes indicate the different regions of interest (ROI). The test pattern has 8 ROIs with metal fraction varying from 0% (ROI 1) to 27% (ROI 8). The varying metal fractions were obtained by printing metal with different finger widths ranging from 0 to 280 µm. (b) Scan of the H pattern solar cell with different ROIs. The ROIs of the test pattern and H-pattern solar cell were analysed individually from PL images obtained at different illumination intensity. The same finger spacing of 1.8 mm was used for both the test pattern and the solar cell.

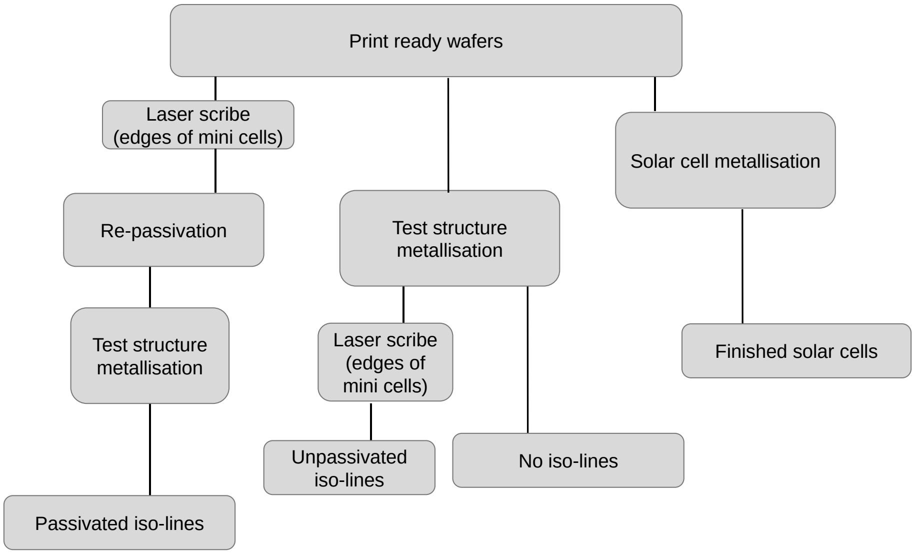

Figure 5-2: Metallisation experimental split for the different test pattern and finished solar cell.

A commercial PL imaging system was used in this study (BT Imaging, Australia). The system is based on a 915 nm wavelength laser as the excitation source and the illumination intensity can be varied in the range of 0.01-3.5 Suns. Both the test pattern and H-pattern cells are imaged under the full range of illumination, and the H-pattern cells are additionally probed at each busbar to monitor their open-circuit voltage (via Suns-V_{oc} measurements). A variety of different methods for quantitatively imaging the local solar cell parameters have been presented in recent years [142] [64, 143, 144]. All these methods rely on calibrating the local luminescence intensity to the local junction voltage. Trupke *et al.* introduced the method in 2007 to calibrate the luminescence images to the local junction voltage [142]. This method was later extended by Glatthaar *et al.* in 2010 [64]. The emitted PL signal I_{pl} is related to V_{oc} by

$$I_{pl} = \mathrm{C}\exp\left(\frac{V_{0c}}{V_t}\right) + \mathrm{B}I_L \qquad (5.1)$$

where V_t is the thermal voltage (25.68 mV at 298 K), B is the local luminescence intensity of an image taken under short-circuit conditions, I_L is the illumination intensity, and C is the calibration constant.

Equation 5.1 relates the spatial signal I_{PL} to the spatial distribution in V_{oc} along the wafer plane. In order to have a correct calibration of the internal voltage from the PL images, it is necessary to accurately determine the constants B and C. Including B in the equation is necessary to reduce the effect of diffusion limited charge carriers occurring during PL imaging and is determined by taking one image at short circuit and at known illumination intensity. The constant C depends on the PL setup and the sample investigated. It is generally determined at open-circuit conditions and at sufficiently low illumination intensities where lateral voltage gradients are negligible in the H pattern cell. In particular C is determined by inserting the probed V_{oc} of the H pattern cell into equation 1 at 0.03-0.05 suns illumination. Both the test pattern and the H pattern cells are assumed to have a common set of B and C since their optical structures and base diffusion lengths are similar.

Equation 5.1 yields the V_{oc} at each pixel for both the test pattern and H pattern cells at every illumination intensity. Instead of performing a pixel-by-pixel parameter extraction [64, 143, 145], a region-of-interest approach of condensing the data by spatial average according to the regions defined in Figure 5-1 for the test pattern and the H pattern was adopted. The results are calibrated Suns-PL plots of the regions of interest, in addition to the probed Suns-V_{oc} curves. Two analysis methods are used. The first is a simple four parameter graphical fitting to the Suns-PL plots of the regions of interest for the test pattern cells only. The graphical fitting involves drawing simple Suns-PL plots by regions-of-interest, followed by two diode fitting and linear regression of the saturation current densities versus metal contact fraction. Here, each region of interest is approximated as a closed boundary system whose V_{oc} obeys

$$\begin{aligned} J_{L,i}(1-f_{metal,i}) \\ &= \left(J_{01}(1-f_{metal,i}) + J_{01,metal}f_{metal,i}\right)\left(exp\left(\frac{V_{OC}}{V_T}\right)-1\right) \\ &+ \left(J_{02}(1-f_{metal,i}) + J_{02,metal}f_{metal,i}\right)\left(exp\left(\frac{V_{OC}}{2V_T}\right)-1\right) \end{aligned} \tag{5.2}$$

where $J_{L,i}$ is the light induced current density in the non-shaded parts of the i^{th} region of interest, consistent with the overall short-circuit current density J_{sc} of the H pattern cell. The reason that $J_{L,i}$ is different for different regions of interest is that the illumination laser is not laterally uniform. Therefore, the laser intensity at different areas needed to be measured using a small-area solar cell and accounted for. $f_{metal,i}$ is the aerial fraction of metal contact area for the i^{th} region of interest. The four adjustable parameters for fitting are J_{01}, J_{02}, $J_{01,metal}$, $J_{02,metal}$, representing the first and second diode saturation current densities of the passivated emitter and the additional contributions at the metallized emitter. Plots of Suns-PL by region on the test pattern cell, obtained from the experiment and simulation, are compared, and the root-mean-square deviation in the recombination current between experiment and simulation is used as a measure of goodness of the fit.

The second method involves high-fidelity constructions of the test pattern and H pattern cells using an in-house finite-element method (FEM) based simulator called Griddler [110], which breaks down the wafer plane and the metallization pattern into roughly 80,000 nodes and 160,000 triangular elements, then solves the voltage distribution among the nodes, and then converts it into a PL distribution via equation 5.1. Each node is treated as a solar cell consisting of a current source and two diodes of ideality factor $m = 1$ and $m = 2$, respectively. Neighbouring nodes are connected by resistors with a suitable value consistent with the emitter sheet resistance (80 Ω/sq), for nodes in the emitter plane, and the metal sheet resistance (3 mΩ/sq) for nodes in the metallization plane. Coinciding nodes in the emitter and metal planes are connected via resistors according to the contact resistance (3 mΩcm^2). There are three types of nodes which differ by the value of saturation current densities assigned to them: 1) passivated emitter nodes, assigned with J_{01} and J_{02} for the two diodes; 2) metallized emitter nodes, assigned with $J_{01,metal}$ and $J_{02,metal}$, and 3) wafer edge nodes, assigned with an additional $J_{01,edge}$ on top of J_{01} and J_{02}. The light-induced current density J_L is distributed in a way that is consistent with metal shading (with triangular elements representing metallized regions receiving no light), illumination laser non-uniformity (which is separately measured), and the cell short-circuit density. Overall, there are five adjustable simulation parameters J_{01}, J_{02}, $J_{01,metal}$, $J_{02,metal}$, $J_{01,edge}$, which Griddler manipulates to simulate high-fidelity PL images for the test pattern and H pattern solar cells. Plots of Suns-PL by region and Suns-V_{oc} by busbars obtained from the experiment and simulation are compared, and the root-mean-square deviation in V_{oc} between experiment and simulation is used as a measure of goodness of the fit.

5.3 Results and Discussion

The degree of metal recombination in Si solar cells depends greatly on the emitter profile. The emitter in this work was characterized by four point probe for sheet resistance measurements, electrochemical capacitance-voltage for active dopant profile measuremnts, and implied V_{oc} and emitter saturation current density measurements. The 80-Ω/sq phosphorus diffused emitter has a peak surface doping concentration of 3.9×10^{20} atoms/cm^3 and a junction depth of 0.32 µm, as shown in Figure 5-3. This profile is representative of the typical phosphorus emitter found in today's industrial Si wafer solar cells.

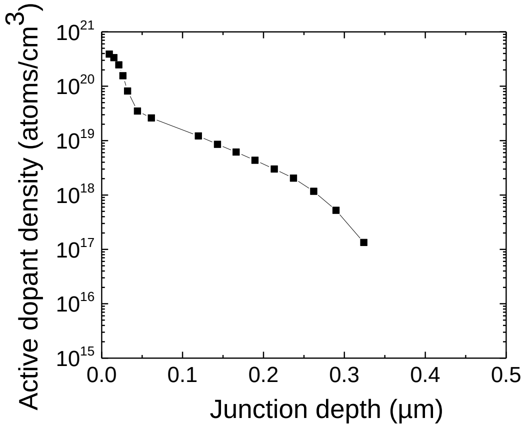

Figure 5-3: Active dopant profile of the phosphorus diffused emitter used in this study. The 80-Ω/sq phosphorus diffused emitter has a junction depth of 0.32 µm and active surface doping concentration of 3.9×10^{20} atoms/cm^3.

PL images of the test pattern cells were taken at different illumination intensities ranging from 0.03 to 3.6 Suns. Figure 5-4 shows the PL images of the different test patterns used in this study when taken at about

1 Sun (top) and about 0.1 Suns (bottom). The test structure with unpassivated iso-lines shows dark boundaries which reflects the much higher recombination induced by the laser scribe damage. The impact of the boundary recombination on the overall voltages of the region of interests is especially severe at 0.1 suns (because the lateral balancing current is lower). The test pattern with passivated iso-lines has visibly much lower boundary recombination because the laser damage has been reduced by chemical etching and re-passivation. However, the SiN_x masking during the chemical etching was not perfectly selective, and thus the emitter sheet resistance has risen significantly above the original 80 Ω/sq, indicating that even the masked regions of the wafer were likely etched to some degree. Moreover it was generally difficult to obtain perfectly passivated boundaries of the mini-cells after laser isolation. Both the undesirable emitter etching and the imperfectly passivated boundaries introduce bias and additional uncertainty to the experiment. Interestingly, the no iso-line samples - which are simplest to process - were also the easiest to model of all investigated samples, as long as the model of analysis manages to account for the balancing currents flowing through the open boundary of each region of interest. Therefore, in the following the focus will be on the no-iso line samples for determining the metal recombination values.

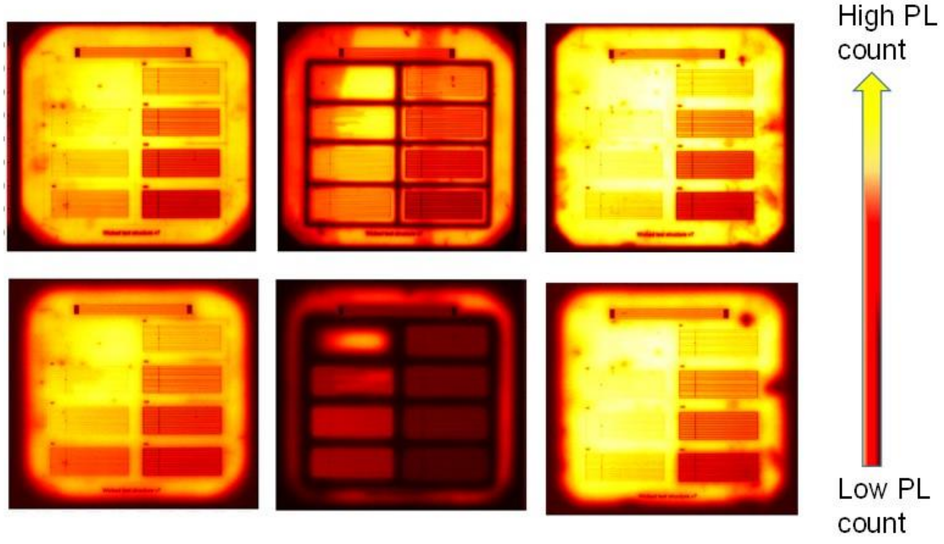

Figure 5-4: Measured PL images of the test patterns with passivated iso-lines, unpassivated iso-lines and no iso-lines, respectively, at 1 sun (top row) and 0.1 sun (lower row) illumination intensity. The impact of laser lines are clearly visible at lower suns (bottom). Test patterns with no iso-lines were used in this work for extracting metal recombination values, since it eliminates the impact of irregular boundaries on the extraction of saturation current densities. All images were scaled using the same calibration constants.

The results from the more rigorous Griddler FEM analysis will be presented first. Figure 5-5 compares the Griddler simulations to the experimental PL images of the test pattern and H pattern cells at 1 Sun and 0.1 Suns. The simulated images are generated using the best fit values of J_{01}, J_{02}, $J_{01,metal}$, $J_{02,metal}$, $J_{01,edge}$, as given in Table 5-1. A good qualitative agreement can be seen, in particular for the relative PL intensities in the 8 regions of interest in the test pattern cell, and also in the gradient of the PL intensity towards the wafer edges. Simultaneous Griddler fitting to both the test pattern and H pattern is very advantageous for the unambiguous determination of the five recombination parameters.

Table 5-1: Extracted saturation current density values by two different methods using PL images obtained at different illumination intensities. $J_{01,edge}$ cannot be determined using graphical fitting method. The high value of $J_{01,edge}$ obtained using FEM simulation is due to the non-optimised laser edge isolation process.

Extraction method	J_{01} (fA/cm^2)	J_{02} (nA/cm^2)	$J_{01,metal}$ (fA/cm^2)	$J_{02,metal}$ (nA/cm^2)	$J_{01,edge}$ (fA/cm^2)
Graphical fitting to Suns-PL curves	408 ± 100	8 ± 2	888 ± 100	36 ± 10	0
Finite element method simulation	423 ± 100	5 ± 2	810 ± 100	124 ± 40	11000 ± 1000

Figure 5-6 shows the Suns-PL curves of the regions of interest in the test pattern and H pattern cells, as well as the probed Suns-V_{oc} of the H pattern cell busbars. There is a striking difference between the Suns-PL behaviours in the two different metal patterns, in particular the slope in the semi-log plot suggesting that the H pattern cell has a higher ideality factor at low illumination intensity. It is also interesting to see that the Suns-PL curves of the different regions of interest in the H pattern cell converge towards low illumination, but those for the test pattern cell diverge. Remarkably, the Griddler FEM simulation is able to replicate these vastly different features using a common set of recombination parameters. The simultaneous fitting lends credibility that the underlying values of J_{01}, J_{02}, $J_{01,metal}$, $J_{02,metal}$, $J_{01,edge}$ used in the simulations are accurate.

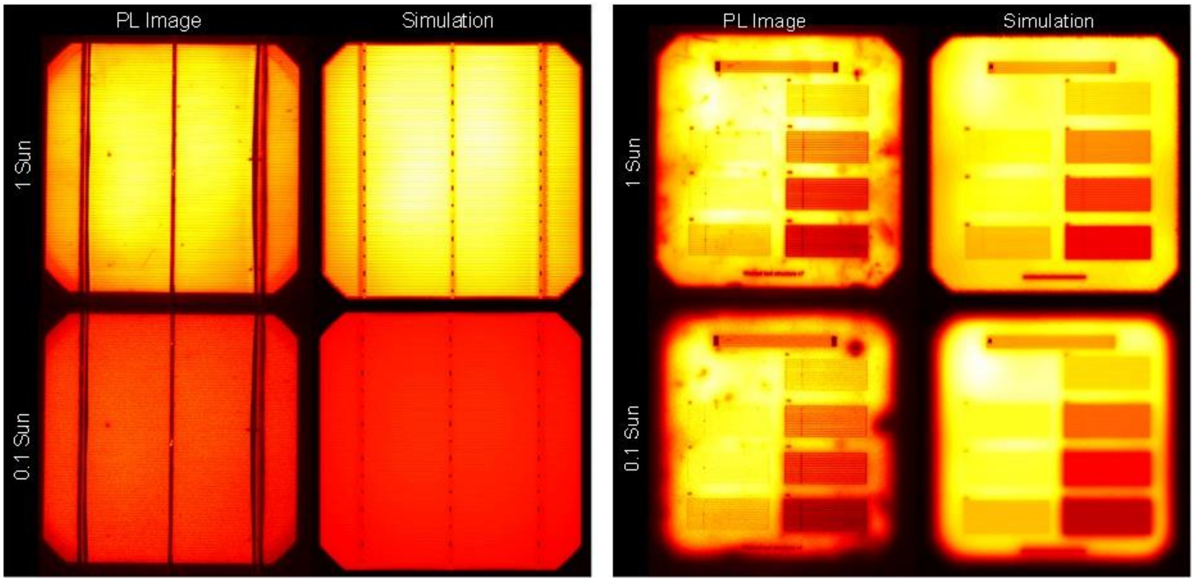

Figure 5-5: The simulated PL images (obtained from the saturation current density values determined using FEM method) match well with the measured PL images at 1 Sun and 0.l Sun illumination intensity.

Table 5-1 also shows the parameters of best fit according to the four parameter graphical fitting to the Suns-PL curves of the test pattern cell. As $J_{01,edge}$ is not considered here it is listed as zero. While this method yields J_{01}, $J_{01,metal}$ values to within 25% agreement with those obtained from the Griddler FEM fitting, the J_{02} and $J_{02,metal}$ values are much different. The better agreement in first diode parameters and poor agreement in second diode parameters suggest that the graphical fitting method is more accurate for analysing PL images at high illumination. At low illumination, the approximation of closed boundaries of the 8 regions of interest tends to break down, as the effects of lateral balancing currents become increasingly severe. For example, at 0.1 Suns, the Griddler FEM simulation predicts that the current flowing into region of interest number 8 is about half of the light-induced current in this region. Because the graphical fitting method ignores this lateral current flow, it grossly miscalculates the recombination parameters from the low light intensity images.

Figure 5-7 shows the fits to the Suns-PL curves for the test pattern cell and Suns-V_{oc} curves of the H pattern cell, based on the parameters of best fit by the graphical fitting method. It is important to note that while in Figure 5-6 the fitted curves are culled from full-area FEM simulations, in Figure 5-7 the fit lines are simply calculated from equation 2. In stark contrast to Figure 5-6, Figure 5-7 shows that it is impossible for the graphical fitting method to yield simultaneous fits to both the test pattern and the H pattern cells. Without taking account of the lateral balancing currents, the test pattern and H pattern cells appear as though they have completely different underlying recombination parameters, which was demonstrated by the Griddler fits in Figure 5-6 not to be the case.

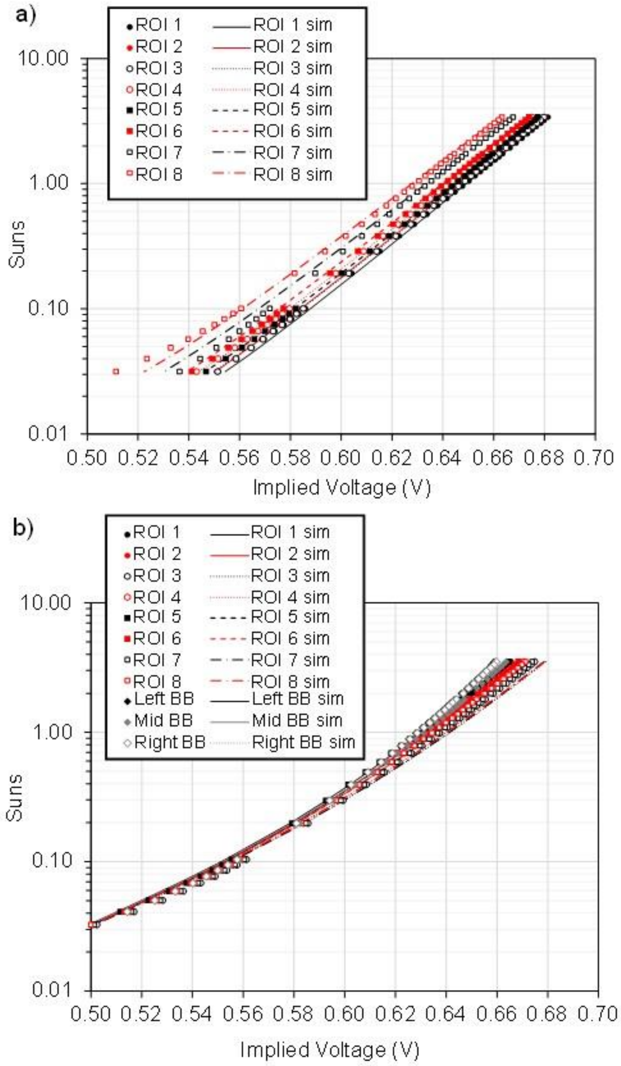

Figure 5-6: (a) Suns-PL curve of the different ROIs in the test pattern obtained experimentally from PL images. (b) Suns-PL curve of the H-pattern solar cell from PL images as well as probed Suns-V_{oc} of the H pattern cell busbars. Using a common set of recombination parameters, the Griddler FEM simulation method is able to accurately fit both the Suns-PL curve of the test pattern and the H-pattern solar cell. Though the term implied voltage is used in the x-axis, it actually means the junction voltage as all PL images are calibrated.

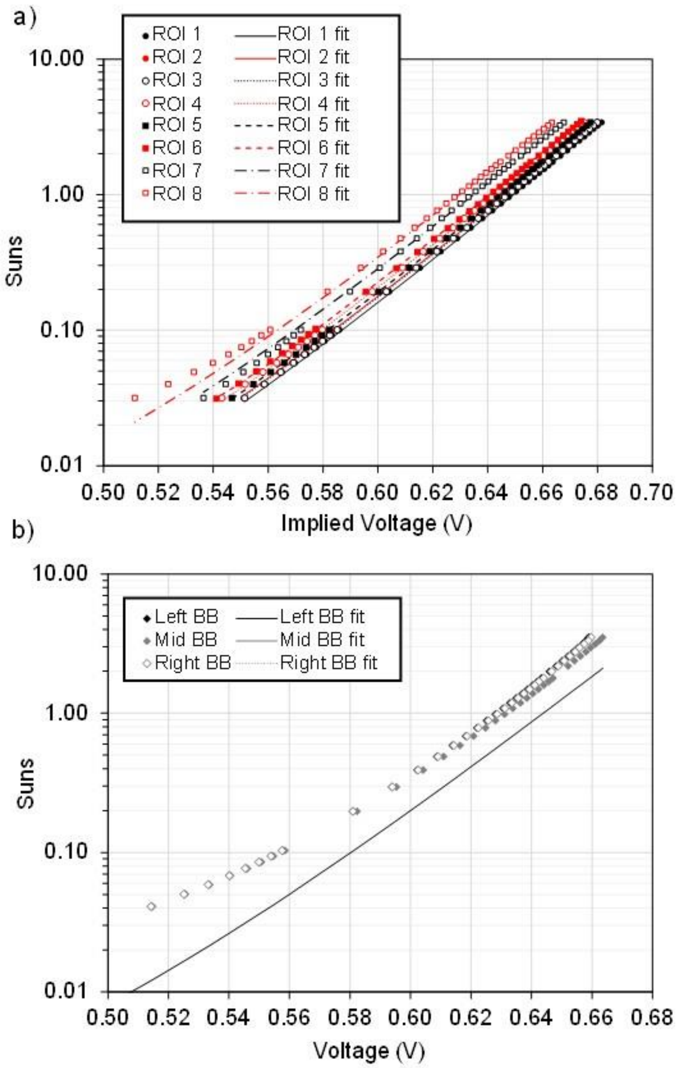

Figure 5-7: (a) Suns-PL curves for the test pattern cell and (b) Suns-V_{oc} curves of the H pattern cell, based on the parameters of best fit by the graphical fitting method. It is not possible to obtain simultaneous fits to both the test patterns and H-pattern solar cell using the graphical fitting method.

It is worth to place the fitted parameters in Table 5-1into perspective, by using the Griddler FEM simulation to predict the Suns-V_{oc} curves if there were no metal induced recombination, i.e. when $J_{01,metal} = J_{02,metal} = 0$. In this case, Griddler predicts that the cell V_{oc} will rise by 3.3 mV at 1 Sun and 5.2 mV at 0.1 Sun. Assuming the cell J_{sc} is 36.8 mA/cm^2, these increments translate into a gain in pseudo efficiency of 0.19% absolute and pseudo fill factor of 0.4% absolute. It is apparent from this assessment that the impact of metal recombination on the cell performance is quite mild.

5.4 Conclusion

The metal-silicon interface in a solar cell is a highly recombination active region that impacts the device voltage. The goal of this work was the accurate determination of the metal recombination parameters at the metal-emitter interface. By analysing test patterns (having mini-cells with varying metal fractions) and finished solar cells using intensity-dependent photoluminescence imaging, the metal recombination parameters were extracted. Three different kinds of boundaries for the mini-cells in the test pattern were experimented: 1) passivated iso-lines (where the laser lines isolating the mini-cells were treated chemically to minimize recombination), 2) unpassivated iso-lines, and 3) no iso-lines. Of the three different test patterns the one with no-iso lines was used in this work for extracting recombination values, since it eliminates the impact of irregular boundaries on the extraction of saturation current densities.

The PL images of the test pattern with no iso-lines and the finished solar cell with H-pattern were analysed in two different ways, one using a simple four parameter graphical fitting to the Suns-PL plots of regions of interest and the other being a detailed finite element method based simulation and numerical fitting. The graphical fitting method was more accurate for analysing PL images at high illumination. However, at low illumination intensity the approximation of closed boundaries of the mini-cells in the test pattern tended to break down, as the effect of lateral balancing currents became severe. As the graphical fitting method ignores this lateral current flow, it grossly miscalculates the recombination parameters from the low-intensity images. The latter method using FEM simulation and numerical fitting takes into account this lateral current flow and hence was able to replicate simultaneously the Suns-PL characteristics of both test pattern and H pattern cells using a common set of recombination parameters. The simultaneous fitting of the test pattern and H pattern cells increases the sensitivity of the developed method, as it was able to effectively extract $J_{01\text{-metal}}$ and $J_{02\text{-metal}}$ even for cases with moderate metal recombination.

Chapter 6: Impact of phosphorus emitter doping profile on the metal contact recombination for silicon wafer solar cells[4]

6.1 Introduction

Screen-printed Al-BSF Si wafer solar cells with phosphorus emitter on the front surface are the workhorse of the PV industry, due to its simple and high throughput nature of the fabrication process [11]. Phosphorus emitter formation and metallisation of these emitters play an important role in the fabrication of Si wafer solar cells. Increasing the conversion efficiency of the Si wafer solar cells without significantly increasing the production cost is a key area of research in the PV community. The emitter formation process followed by screen-printed Ag metallisation of the emitter surfaces are two main areas in the fabrication process, where significant efficiency gains and cost reductions are possible. Previously screen-printed Ag pastes required heavily doped phosphorus emitters, to achieve a good ohmic contact, and this in turn directly limited the conversion efficiency of the Si wafer solar cells. Highly doped phosphorus emitter surface on the front results in a poor response to short wavelengths (blue response) due to increased Auger recombination in the emitter [117] [118]. Recent results have shown the progress of the screen-printed Ag pastes in contacting lightly doped phosphorus emitters [36, 137]. This in turn improves both the voltage and the current of the solar cells.

The screen-printed Ag paste fires through the passivating silicon nitride (SiN_x) antireflection coating film to contact the phosphorus emitter surface. The glass frits present in the Ag paste melts during the firing process and then etches through the SiN_x coating layer to facilitate the formation of the electric contact to the underlying n^+ Si [42]. The metal-Si interface formed after the firing process, is often characterised by

---

[4] Published as Vinodh Shanmugam et alia, "Impact of the phosphorus emitter doping profile on metal contact recombination parameters for silicon wafer solar cells", *Solar Energy Materials and Solar Cells Journal,* volume 147, pages 171-176, April 2016.

complex interfacial regions comprising of a few Ag crystallites grown into Si, a resistive glass layer, nanocolloids of Ag particles and voids [44]. Printed Ag metal contacts introduce significant recombination via the high interface defect density and the emitter damage caused by the high temperature firing step. This makes lightly doped shallow emitters more susceptible to junction shunting and increased recombination losses from the printed metallisation process than emitters with deeper junction. Typical Ag front grid metallisation of a solar cell covers about 6-10% of the total area using an H-pattern with busbars and perpendicular fingers. One approach to reduce the metallisation induced recombination losses is to use a dual print approach for the front side metallisation, wherein the busbars are printed using a less aggressive paste (which causes minimum damage to the SiN_x coating) and also by printing finer fingers using stencils [48] or using advanced printing methods.

There are several studies in the recent years to accurately determine the metal contact recombination parameters using specially designed test structures [67, 133, 138, 146]. The metal contact recombination parameters depends on the phosphorus emitter profile itself. In this work, we analyse the intensity-dependent PL images on front metallization test patterns consisting of regions of different metal contact fractions [67], solar cells with no front metallisation, and solar cells with H-pattern front metallization, to accurately extract the metal contact recombination parameters. For each of these cells, a detailed finite element model (FEM) of the cell front plane with the exact dimensions of the metallization pattern is constructed using Griddler [67]. Griddler solves the voltage distribution in the cell plane and converts it into the PL intensity spatial distribution, via a calibration factor determined from the H-pattern solar cell probed voltage at low illumination intensity [67]. Simulation of the PL spatial distribution and comparing them to actual images then allows the metal induced recombination saturation current densities to be extracted when a best fit is achieved. The FEM approach fully accounts for lateral balancing currents along the wafer that has a non-uniform voltage distribution, thus eliminating the need to electrically isolate the different regions on the test structure and simplifying the fabrication process. The key contribution of this work is the application of the analysis routine of reference [67] to industrial multi-Si solar cells with different lightly doped phosphorus emitters.

6.2 Experimental details

6.2.1 Fabrication of different emitters

In this study, large-area 243 cm^2 (156 mm × 156 mm) *p*-type multi-Si wafers, with a thickness of approximately 160-180 µm were used. Wafers from the same ingot with a narrow base resistivity range (1.1-1.2 Ωcm) were selected to minimise the impact of variation in the bulk lifetime of the multi-Si wafers on the determination of the metal contact recombination parameters. The wafers underwent standard wet-chemical acidic texturing in an industrial wet-chemical process tool (RENA, InPilot). The texturing process involved three major steps: (1) isotropic texturing in a solution of hydrofluoric acid (HF) and nitric acid (HNO_3) solution, (2) followed by removal of the porous Si formed due to isotropic texturing in a solution of potassium hydroxide (KOH), and (3) finally cleaning in a solution of hydrochloric acid (HCl) and HF to remove the metallic impurities. The textured wafers were then diffused in a Tempress tube diffusion furnace at a peak diffusion temperature of 870°C using phosphorus oxychloride ($POCl_3$) as the dopant source. This resulted in a sheet resistance of 50 Ω/sq. The diffused wafers were then split into four groups. Group 1 is the as diffused wafer with a sheet resistance of 50 Ω/sq. An emitter etch back process was applied using the ‘SERIS etch’ [67] on the remaining as-diffused wafers for different durations (80, 150, and 200 s) to achieve emitters with different surface doping concentration and junction depths. Varying the duration of the etch back process resulted in sheet resistances of 70 Ω/sq, 90 Ω/sq and 130 Ω/sq (Group 2, Group 3 and Group 4 respectively).

6.2.2 Fabrication of lifetime samples

Symmetrical lifetime test structures were fabricated for the analysis of the different emitter groups. Textured and diffused wafers from the different emitter groups, underwent phosphosilicate glass removal.

On the front and rear surfaces of these wafers a 70 nm thick amorphous SiN_x layer (refractive index of 2.05 at 633 nm) was deposited by inline PECVD using an industrial machine from Roth & Rau. Finally the lifetime samples were fired in an industrial belt firing furnace (DESPATCH, CDF furnace) at a peak temperature of 850°C.

6.2.3 Fabrication of solar cells

The acid textured wafers were initially phosphorus diffused on both sides of the wafer using a Tempress tube diffusion furnace to result in a sheet resistance of 50 Ω/sq. These wafers then underwent simultaneous wet-chemical rear junction isolation and PSG removal steps by an inline wet chemical process tool (RENA, InPilot). It uses a mixture of HF, HNO_3, sulphuric acid (H_2SO_4), and DI water at a temperature of 7-8°C. The wafers were then split into 4 different groups. Group 1 is the as-diffused wafers with a sheet resistance of 50 Ω/sq. The 'SERIS etch' emitter etch back was then performed on the remaining wafers for different durations (80, 150, and 200 s) to result in Group 2, Group 3 and Group 4 batches with phosphorus sheet resistance of 70 Ω/sq, 90 Ω/sq and 130 Ω/sq respectively. A SiN_x film was then deposited by PECVD onto the front surface of the wafers as an antireflection coating and passivation layer. The cells were then metallised by screen printing using Al paste on the rear (Monocrystal, PASE 12D), without any rear Ag busbar prints, and Ag paste on the front (DuPont PV 18F). Finally the front and rear contacts were co-fired in an industrial fast firing furnace at a peak temperature of 850°C. Figure 6-1 shows the fabrication sequence used in this work for the fabrication of solar cells. As discussed in the introduction, for each emitter group there is a categorization of three solar cell test sample types: 1) ones metallised with the H-pattern front grid (3 busbars and 82 fingers with finger widths of ~55 µm), 2) ones that did not have front metallisation, 3) one metallised with the front test pattern as shown in the Figure 6-2 (a), which consisted of 8 different regions of interest (ROI). The ROIs in this test pattern had metal fractions varying from 0% (ROI 1) to 27% (ROI 8). The varying metal fractions were obtained by printing metal with different finger widths ranging from 0 to 280 µm. The same test pattern was used in reference [67].

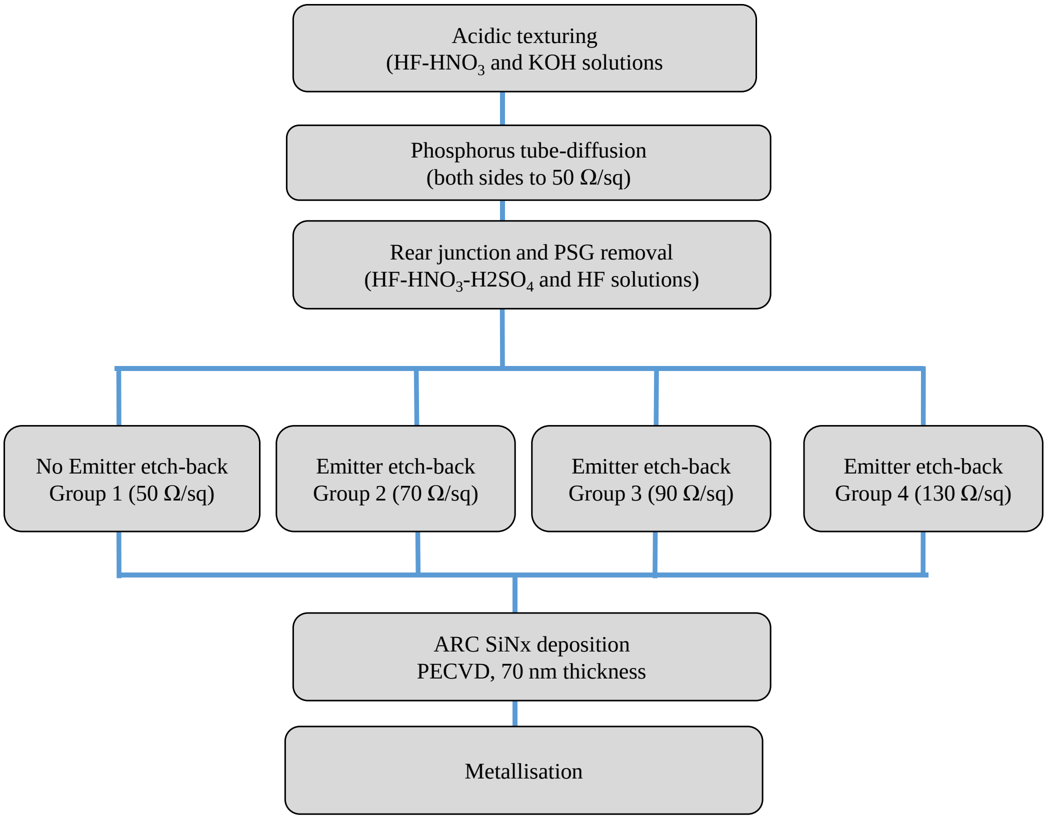

Figure 6-1: Fabrication process flow for the solar cells used in this work. Solar cells with different phosphorus doping concentration were achieved using the patented 'SERIS Etch solution.

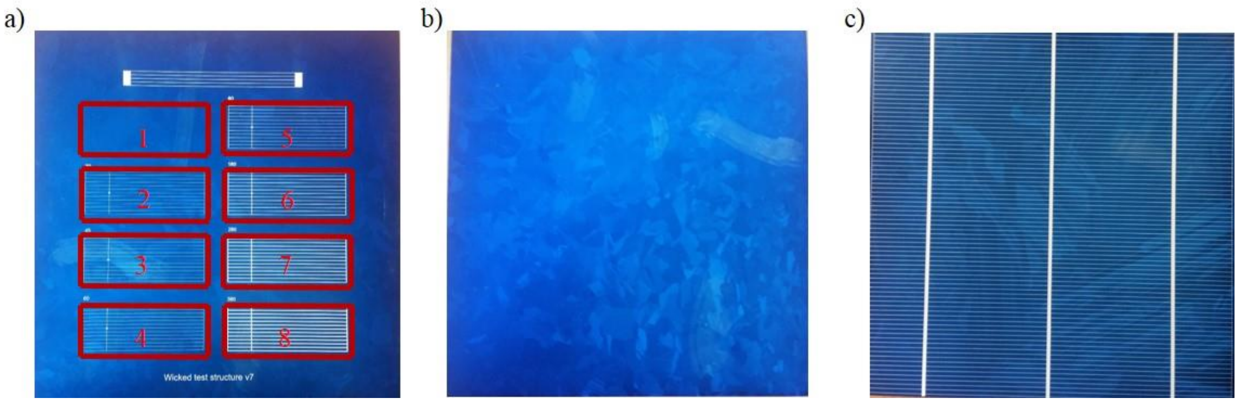

Figure 6-2: Solar cell sample types used for the determination of the metal contact recombination parameters. (a) test pattern with regions of varying metal contact fractions. The red boxes indicates the different regions of interest (ROI). It has 8 ROI with metal fraction ranging from 0% (ROI 1) to 27% (ROI 8). The varying metal fractions were obtained by printing metal with different finger widths ranging from 0 to 280 µm. (b) cells with no front metal grid. (c) cells with H-pattern front metal grid. The same finger spacing of 1.8 mm was used for the test pattern (a) and the solar cell.

6.3 Characterisation methods

The phosphorus-diffused emitters used in this study were characterised by 4 point probe (Napson) for sheet resistance measurements, electrochemical capacitance-voltage profiling (WEP CVP 21) for active dopant profile measurements. The implied V_{oc} and the emitter saturation current density J_{oe} for different emitter groups were determined from their respective lifetime samples using quasi-steady-state photoconductance (QSSPC, Sinton Instruments). The implied V_{oc} was determined using the Suns-V_{oc} [61] method and the J_{oe} was determined using the Kane-Swanson method [129]. One-sun current-voltage measurements of the finished solar cells were measured using a steady state I-V tester under standard testing conditions (1000 W/m^2, AM1.5G spectrum, 25^{o}C cell temperature). An Enlitech SR-156 large-beam scanner was used to measure the spectral response of the solar cells over the 300-1200 nm wavelength range. A commercial PL imaging system (BT Imaging, Australia) was used in this study for intensity-dependent PL imaging.

6.4 Results and Discussion

6.4.1 Emitter Characterisation

The as-diffused phosphorus emitter (Group 1) has a high active phosphorus surface doping concentration of 2.5×10^{20} atoms/cm^3. The heavily doped phosphorus layer at the surface results in increased carrier recombination losses, which reduces both the V_{oc} and the J_{sc} of the fabricated solar cells. After the etch back process, the thickness of the heavily doped layer for other groups (Group 2, 3 and 4 respectively) is significantly reduced (see Figure 6-3). Furthermore the implied V_{oc} and the emitter saturation current density J_{oe} as shown in Table 6-1, shows a clear trend of reduction in recombination for the lightly doped etched-back emitters. The effective minority carrier lifetime (τ_{eff}) is reported at an excess carrier concentration 10^{15} cm^{-3}, while emitter saturation current density (J_{0e}) is extracted at excess carrier concentration of 10^{16} cm^{-3} using the Kane-Swanson method [129]. A steady increase in the implied V_{oc} values from 638 mV to 664 mV (Group 1 to Group 4 respectively) and lifetime from 36 µs to 138 µs (Group 1 to Group 4 respectively), and a drop in J_{0e} values from 200 fA/cm^2 to 65 fA/cm^2 (for Group 1 to Group 4 respectively) indicates clearly the benefits of lightly doped phosphorus emitters.

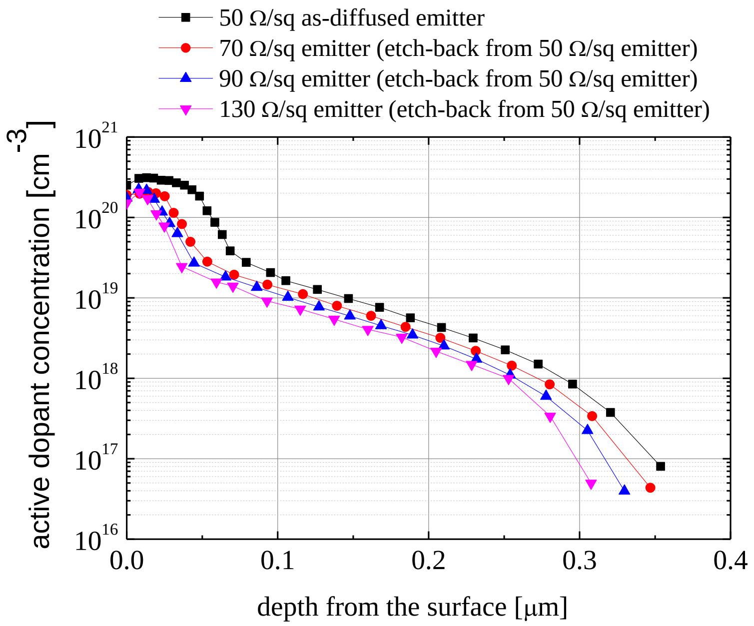

Figure 6-3: Active dopant profiles of the different phosphorus emitters used in this study. As diffused 50 Ω/sq phosphorus emitter was etched using the SERIS Etch solution for different time durations (80, 150 and 200 s), to result in Group 2, Group 3 and Group 4 emitters respectively.

Table 6-1: Characteristics of the different phosphorus emitters used in this study.

	Group 1	Group 2	Group 3	Group 4
Average Sheet resistance (Ω/sq)	50	70	90	130
Effective lifetime (μs)	36	60	83	138
Implied V_{oc} at one-Sun (mV)	638	652	660	664
Emitter saturation current density J_{0e} (fA/cm^2)	200	102	84	65

6.4.2 Solar cell results

Table 6-2 below shows the electrical characteristics (5 solar cells in every group) of the solar cells fabricated. There is a clear increase in the J_{sc} of the fabricated solar cells, as the emitters become lightly doped. Group 1 with an emitter sheet resistance of 50 Ω/sq resulted in an average J_{sc} of 35.6 mA/cm^2 and the other etch back emitter groups resulted in steady increase in the J_{sc} values with Group 4 (130 Ω/sq emitter batch) having the highest average value of 36.3 mA/cm^2. The variation of the internal quantum efficiency (IQE) of the representative cells from different groups is shown in Figure 6-5. Improvements in the short-wavelength IQE of the etch back emitter cells contribute to the enhancement in the J_{sc} values when compared to solar cells from Group 1 with high surface doping concentration. Fill Factor (*FF*) values of approximately 78% and above for all the groups indicates the contacting capability of the Ag paste (DuPont PV 18) used in this work. V_{oc} values of the solar cells fabricated shows the similar trend of implied V_{oc} and minority carrier lifetime values as shown in Table 6-1. However the variation in V_{oc} is not as strong as the variation in implied V_{oc}. The specific contact resistivity of the Ag paste to the emitter layer was measured using the transfer length method (TLM) [16], by cutting small strips (parallel to the busbars) from finished solar cells. All groups yielded values around 3-10 mΩ cm^2. The V_{oc} values increases as the emitter becomes lightly doped. However for the Group 4 emitters there is no significant increase in V_{oc} values and also a slight drop in the values are noticed. The reason for this drop is investigated in the next section. The highest average efficiency of 18.0% was achieved with the Group 3 emitters (sheet resistance of 90 Ω/sq). The highest solar cell efficiency achieved in this study was 18.1% (also from Group 3, see Figure 6-4).

Table 6-2: Statistics of the electrical parameters of the solar cells from different emitter groups. Group 1 is 50 Ω/sq, Group 2 is 70 Ω/sq, Group 3 is 90 Ω/sq and Group 4 is 130 Ω/sq.

Electrical parameters	Emitter groups	Statistics		
		Average	Minimum	Maximum
J_{sc} (mA/cm^2)	Group 1	35.6	35.5	35.8
	Group 2	36.2	36.1	36.2
	Group 3	36.2	36.1	36.3
	Group 4	36.3	36.1	36.4
V_{oc} (mV)	Group 1	626.0	625.0	627.0
	Group 2	630.0	629.0	631.0
	Group 3	632.0	629.0	634.0
	Group 4	631.0	628.0	634.0
FF (%)	Group 1	78.8	79.4	77.7
	Group 2	78.8	78.9	78.6
	Group 3	78.6	78.4	78.8
	Group 4	77.8	77.3	78.1
	Group 1	17.6	17.4	17.7
	Group 2	17.9	17.8	18.0

Efficiency (%)	Group 3	18.0	17.8	18.1
	Group 4	17.8	17.7	17.9

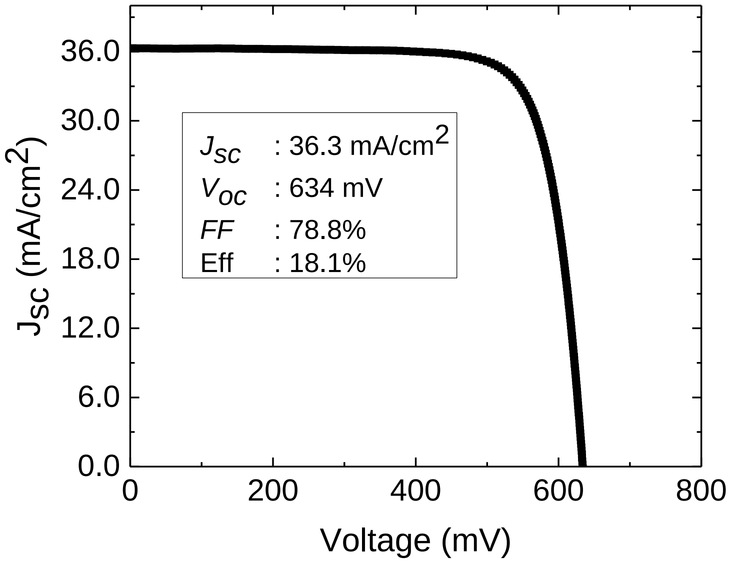

Figure 6-4: One-Sun I-V curve of the best cell (Group 3, with phosphorus emitter sheet resistance of 90 Ω/sq, surface doping concentration of 1.7 × 10^{20} atoms/cm^3 and junction depth of 0.30 µm).

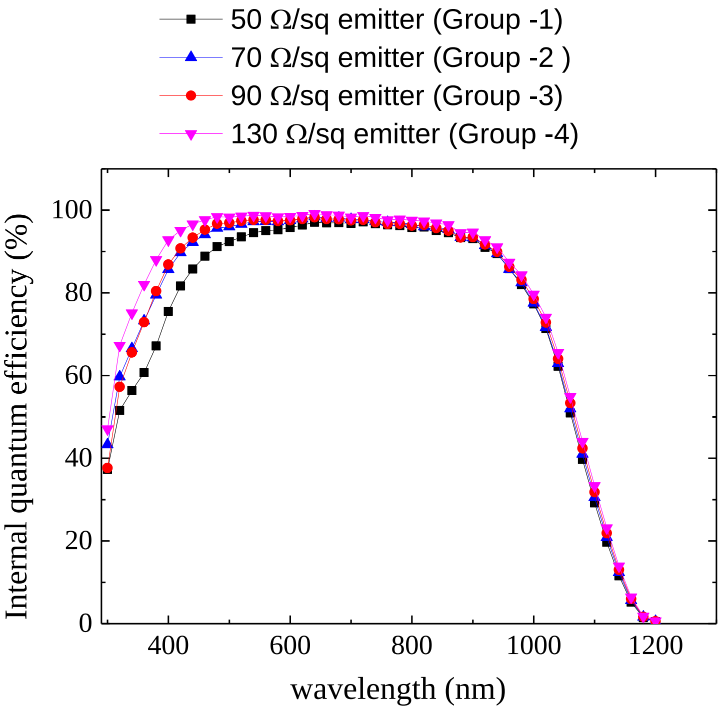

Figure 6-5: Internal quantum efficiency of all the four groups of solar cells fabricated. Group 2, Group 3 and Group 4 cells have better blue response (low wavelength response) when compared to as-diffused Group 1 emitter cells. This is the reason for the etched back cells to have better J_{sc} values than the as-diffused cells.

6.4.3 Metallisation-induced recombination

In this section, in order to understand the reasons for the drop in V_{oc} of the Group 4 cells after metallisation, we analyse the test structures and finished solar cell by intensity dependent PL imaging (for all the four groups). The PL imaging system used in this work, is based on a 915 nm wavelength laser as the excitation source and the illumination intensity can be varied in the range of 0.03-3.5 Suns. The test pattern and the H-pattern solar cells from the different emitter groups are imaged under the full range of steady-state illumination, and the H-pattern solar cells are additionally probed at each busbar to monitor their V_{oc}. The local luminescence intensity can be calibrated to the junction voltage and in this work calibration of the PL intensity to junction voltage was done at roughly 0.03 Suns illumination level, where the voltage across the cell plane could be approximated as being spatially uniform. The method demonstrated in this work involves high-fidelity constructions of the test pattern and H pattern cells using Griddler. This simulator breaks down the wafer plane and the metallisation pattern into roughly 80,000 nodes and 160,000 triangular elements. Each node is treated as a solar cell consisting of a current source and two diodes of ideality factors *n* =1 and *n* =2 respectively. The nodes are interconnected by resistors with values consistent with the emitter sheet resistances (based on the different emitter groups), and the metal sheet resistance (3 mΩ/sq) for nodes in the metallisation plane. Coinciding nodes in the emitter and metal planes are connected via resistors according to their respective contact resistance values. There are three types of nodes which differs by the value of saturation current densities assigned to them: (1) passivated emitter nodes, assigned with J_{01} and J_{02} for the two diodes; (2) metallised emitter nodes, assigned with $J_{01\text{-}metal}$ and $J_{02\text{-}metal}$, corresponding to about 6-10% of the regions in the cell with front metal contact; (3) for nodes within 2 mm distance from the edge of the wafer, the wafer edge nodes are assigned with an additional $J_{01\text{-edge}}$ on top of J_{01} and J_{02}. (The main contributing factors to edge recombination are the absence of a back surface field in Al-BSF cells near the wafer edge, or a drop off in passivating quality of a plasma deposited dielectric in the periphery of the solar cell) [147]. Overall there are five adjustable simulation parameters, which Griddler fits to simulate the high fidelity PL images for the test patterns and the H-pattern solar cell (for different emitter groups). The FEM simulation parameters of best fit are shown in Table 6-3. Using a common set of recombination parameters the FEM simulation method was able to accurately fit the two test patterns and the H-pattern solar cells at different illumination intensities (for all emitter groups). As can be seen from the values, the metal recombination current increases as the emitter becomes lightly doped.

Table 6-3: FEM simulation parameters of best fit. The common set of recombination parameters which were able to simultaneously fit the two different test structures and the H-pattern solar cell.

Cell Group	Emitter (Ω/sq)	J_{01} (fA/cm^2)	J_{02} (nA/cm^2)	$J_{01\text{-metal}}$ (fA/cm^2)	$J_{02\text{-metal}}$ (nA/cm^2)	$J_{0\text{-edge}}$ (fA/cm)
1	50	540	10	1800	10	760
2	70	450	10	2100	30	760
3	90	350	10	2100	100	760
4	130	260	10	2500	120	760

It is worth to place the fitted parameters in Table 6-3 into perspective, by using Griddler FEM simulation to predict the V_{oc} if there were no metal-induced recombination (that is when $J_{01\text{-}metal} = J_{02\text{-}metal} = 0$). In this case Griddler predicts an increase of 0.1% absolute inefficiency for Group 1 and Group 2 emitters and an increase of 0.2% in efficiency for Group 3 and Group 4 emitters primarily due to the increase in cell V_{oc}. The cell V_{oc} will increase by 6 mV at 1 Sun for Group 1 emitters (50 Ω/sq), by 7 mV for Group 2 emitters (50 Ω/sq), by 7 mV for Group 3 emitters (90 Ω/sq), and by 12 mV for Group 4 emitters (130 Ω/sq). This difference in V_{oc} obtained due to no metal-induced recombination matches well with the implied V_{oc} values obtained from the test structures with no front grid metallisation for the different emitter groups as shown in the Figure 6-6.

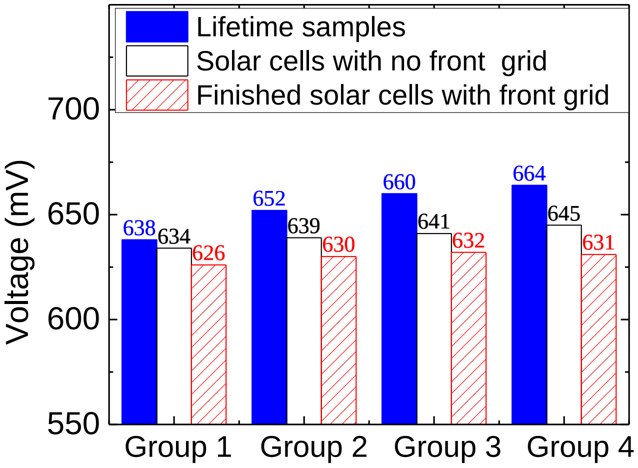

Figure 6-6: Implied voltage from lifetime samples and test structures with no front grid for different emitter groups are compared with the average measured voltage of the finished solar cells. Implied voltage from lifetime samples are measured using quasi steady state photoconductance measurements. Implied voltage on solar cells with no front grid are measured from PL images after calibration (with the finished solar cell's voltage at low Suns). After front grid metallisation, the Group 4 cells have the highest drop in V_{oc} *when compared to the other emitter Groups.*

6.5 Conclusion

This work presents a comprehensive approach using carefully designed experiments and simulations to determine the impact of metallisation-induced recombination losses on phosphorus emitters with varying surface doping concentration and junction depths. By analysing test patterns and finished solar cells simultaneously using intensity-dependent PL imaging, we were able to accurately determine the metal recombination parameters and also its impact on the solar cell performance. For the lightly doped emitter used in this study with a phosphorus emitter sheet resistance of 130 Ω/sq, there is a 12 mV drop in V_{oc} after front grid metallisation (and the metal recombination saturation current densities $J_{01\text{-}metal}$ and $J_{02\text{-}metal}$ were 2500 fA/cm^2 and 120 nA/cm^2 respectively). Screen-printed Ag pastes have improved drastically in contacting phosphorus emitters with lower surface doping concentrations. However due to the etching nature of the pastes, the metallisation induced recombination losses increases as the emitters become lightly doped and shallower. This limits the efficiency gain in solar cells with lightly doped emitters. Using a dual print approach by printing busbars with less aggressive pastes and printing fine metal fingers (less metal contact fraction) would help to reduce the metallisation induced recombination losses and in turn increase the conversion efficiency of the Si solar cells.

Chapter 7: Conclusions, original contributions and proposed future work

7.1 Conclusions

This thesis investigated printed metallisation of phosphorus doped silicon surfaces for solar cell applications. Screen printed metallisation of phosphorus doped surfaces is a well-established process and despite being a commercially successful and dominant metallisation method, there are certain fundamental limitations associated with this process. The various losses associated with the screen printed front side metallisation of phosphorus emitter surfaces were discussed. Methods to overcome these losses and new methods to characterise these losses were demonstrated in this work. The results of this thesis present significant progress in the development and characterisation of front-side Ag metal contacts to phosphorus emitters, using industrial processing conditions. Chapter 3 focused on fine-line printing, Chapter 4 focused on contact formation to lightly doped phosphorus emitters, Chapters 5 and 6 focused on determination of metal contact recombination parameters and the impact of phosphorus doping profile on the metal recombination parameters. Below, each chapter is briefly summarized.

Reducing the printed Ag metal line width without significantly increasing the line resistance and at the same time minimising the Ag paste consumption is a key area of research in the silicon PV community. Of the various available printed metallisation methods, stencil printing seems to be the potential alternative to replace screen printing for fine-line metallisation. In Chapter 3, two high-throughput printing metallisation methods namely printing by screens *vs.* stencils were compared. The electrical properties of fine lines printed with screens and stencils were investigated and a dimensionless factor known as 'print quality factor' was used in this work to characterise the printed metal lines. Uniform print line definition and optimised Ag paste consumption makes stencil printing the ideal choice for fine line metallisation.

In Chapter 4, the impact of the phosphorus doping profile on the contact formation of Ag screen printed pastes was studied. Typically screen printed pastes require a heavily diffused phosphorus emitter surface to ensure a low-resistance ohmic contact. The consequence of having a heavily-doped emitter on the light receiving surface results in a poor response to short wavelengths due to an increased Auger recombination in the emitter. Ag pastes from two different generations were used in this work to contact lightly doped phosphorus emitter surfaces. The patented ‘SERIS etch' solution was used in this work to alter the emitter doping profiles. A microstructural analysis of the contact formation indicated the dominant current transport mechanism for the two different pastes. Experiments showed that a high density of Ag crystallites formed with a thin interfacial glass layer at the Si-Ag interface is beneficial for contacting lightly doped phosphorus surfaces, and the benefits of lightly doped emitter surfaces can be reaped only if the Ag pastes are able to contact these n^+ surfaces.

In Chapter 5, a new method was developed to accurately determine the metal recombination parameters at the metal-phosphorus emitter interface. By analysing test patterns (having mini-cells with varying metal fractions) and finished solar cells using intensity-dependent photoluminescence imaging, the metal recombination parameters were extracted. Three different kinds of boundaries for the mini-cells in the test pattern were experimented: 1) passivated iso-lines (where the laser lines isolating the mini-cells were treated chemically to minimize recombination), 2) unpassivated iso-lines, and 3) no iso-lines. The impact of the boundaries of the mini cells were studied using PL imaging. Of the three different test patterns the one with no-iso lines was used in this work for extracting recombination values, since it eliminates the impact of irregular boundaries on the extraction of saturation current densities. The PL images of the test pattern with no iso-lines and the finished solar cell with H-pattern were analysed in two different ways, one using a simple four parameter graphical fitting to the Suns-PL plots of regions of interest and the other being a detailed finite element method based simulation and numerical fitting. The latter method using FEM simulation and numerical fitting was able to replicate simultaneously the Suns-PL characteristics of both test pattern and H pattern cells using a common set of recombination parameters. The simultaneous fitting of the test pattern and H pattern cells increases the sensitivity of the developed method.

In Chapter 6, the developed method for determining metal contact recombination parameters were applied to multi-Si silicon solar cells. The degree of metallisation induced recombination losses depends on the emitter profile itself. In this work, the effect of metallisation induced recombination losses on four different phosphorus doped emitters with active phosphorus surface doping concentration ranging from 2.5×10^{20} atoms/cm^3 to 1.5×10^{20} atoms/cm^3 and junction depth ranging from 0.32 µm to 0.28 µm were studied. As the phosphorus emitter profile becomes more lightly doped and shallower, the metallisation induced recombination losses increases. The clear trend obtained on the variation of the metal contact recombination values with respect to phosphorus emitter doping profiles were strengthened by analysing various test structures as explained in this work.

7.2 Author’s original contributions

The following is a brief summary of the author’s primary original contributions in this thesis:

I. Analysis of electrical properties of fine-lines printed using screens and stencils. A dimensionless factor known as the ‘print quality factor’ was used in this work to characterise the printed metal lines, based on the printed line profile measured using a 3D optical microscope. Screens and stencils with different finger openings were used in this work.

II. A statistical method was introduced to evaluate the quality of the printed front metal lines based on the distributions of printed metal line profiles, line segment conductance, overall EL pattern, and solar cell light current-voltage characteristics. The model distribution, combined with FEM model to predict realistic cell level voltage variations, was able to adequately describe all four kinds of characteristics. The FEM model predicted well the diverging performance of screen and stencil printed solar cells as the line width reduced to less than 50 µm.

III. Demonstrated an average efficiency gain of 0.2% absolute by consuming only 78 mg of Ag paste per solar cell. Achieved higher efficiencies at a lower cost (reduced Ag consumption by almost 40% than the baseline) by using stencils for fine-line printing.

IV. Analysis of contact formation to lightly doped phosphorus emitters. The emitter doping profiles were altered using the patented ‘SERIS etch' solution. The impact of phosphorus emitter doping concentration on the contact formation process was investigated. Microstructural analysis of contact formation showed that a high density of Ag crystallites with a thin interfacial glass layer at the Si-Ag interface was essential for contacting lightly doped phosphorus emitters.

V. Developed a new method to characterise the metal contact recombination parameters using intensity dependent photoluminescence imaging. Newly developed test structures and measurement methods were presented to accurately determine the metal contact recombination parameters.

VI. The impact of the boundaries of the mini cells used in the test structures were characterised using PL imaging. Griddler, a finite element method solver developed at SERIS, was used for extracting the metal contact recombination parameters.

VII. Application of the developed method to determine the metal contact recombination parameters on multicrystalline silicon solar cells. The impact of phosphorus emitter doping profiles on the contact formation and the metallisation induced recombination losses were studied using test structures. A clear trend was obtained on the variation of the metal contact recombination values with respect to the emitter doping profiles. Lightly doped phosphorus emitters had higher metallisation induced recombination losses.

The author's publications arising from this PhD research are listed at the end of this thesis.

7.3 Proposed future work

This section discusses the interesting future research topics motivated by this thesis.

7.3.1 Multi-busbar silicon wafer solar cells

The standard front side metallisation pattern for an Al-BSF silicon wafer solar cell (156 mm × 156 mm) is an H-pattern with three busbars and perpendicular fingers. Reducing the printed finger width increases the finger line resistance significantly (as the finger length before being intercepted by a busbar still remains the same at approximately 25 mm). One approach to reduce the finer line resistance is to print more number of busbars (greater than 3) of smaller widths than the original busbar width of 15 mm. This multi-busbar approach opens a wide range of possibilities to print finer metal lines using a variety of methods as discussed in Chapter 2 of this thesis. The problem of higher line resistance associated with finer printed lines using inkjet printing, aerosol jet printing, flexographic printing, laser transfer printing, etc. can be easily overcome by printing more number of busbars. Printing finer lines not only helps in reducing shading losses but also reduces the Ag consumption. This eventually helps in achieving higher conversion efficiency at a lower production cost. This approach is slowly being picked up the PV industry, with many companies using multi-busbar approach in their production lines.

7.3.2 Printed copper metallisation for silicon wafer solar cells

Screen printed Ag pastes are widely used for contacting phosphorus doped silicon surfaces. Cost analysis reports have shown that metallisation pastes to be the second most expensive material (after the Si wafer) in the solar cell fabrication process. Therefore the PV community is in a constant push to reduce the Ag consumption or completely even eliminate it. A promising alternative metal for solar cell metallisation is copper (Cu). Cu has similar conductivity as Ag, and is almost 100 times cheaper than Ag at present. Despite the significant cost advantage, Cu has not yet replaced Ag as the mainstream metal for Si wafer solar cells because of concerns regarding Cu diffusion to Si which would severely degrade the cells. To further the use of Cu metallisation, it is essential to use adequate barrier layers to prevent Cu diffusion into Si. Printing Cu metal pastes on top of transparent conductive oxide (TCO) layers or on top of printed Ag seed layers would be an ideal starting point to reduce Ag consumption.

7.3.3 Printed metallisation of boron doped surfaces

The standard Al-BSF Si solar cell has become the workhorse of the PV industry due to its simplicity and the high-throughput nature of the process. But there are certain limitations of this architecture, which makes it not suitable for next-generation, thin, high-efficiency silicon wafer solar cells. The relatively high back surface recombination velocity, low back surface reflection and wafer bowing due to full-area Al metal paste on the rear are some of the reasons for limiting the efficiency potential of this solar cell. Boron diffusion to form p^+ surfaces is a promising alternative and is being used in high-efficiency solar cells. Printed metallisation of boron doped surfaces using Ag/Al pastes is becoming widely adopted and is showing promising results. Recent studies have shown that screen printing and firing of metal pastes to contact the boron doped surfaces limits the open-circuit voltage of the solar cells. The characterisation and analysis methods developed in this thesis for Ag pastes contacting phosphorus doped surfaces can be easily applied to study the contact formation of Ag/Al pastes for contacting boron doped surfaces.

References

---

[1] (15 May 2015). *World population, US census bureau*. Available: http://www.census.gov/population/international/data/idb/worldpoptotal.php

[2] IEA, *World Energy Outlook 2014*: IEA, 2014.

[3] O. Ellabban, H. Abu-Rub, and F. Blaabjerg, "Renewable energy resources: Current status, future prospects and their enabling technology," *Renewable and Sustainable Energy Reviews*, vol. 39, pp. 748-764, 11 2014.

[4] S. Singer, "The energy report: 100% renewable energy by 2050," 2010.

[5] "IEA World Energy Statistics 2013," 29 October 2013 2013.

[6] J.-M. G. Oliver JGJ, Muntean M and Peters JAHW, "Trends in global CO2 emissions; 2013 report," The Hague: PBL Netherlands Environmental Assessment Agency; Ispra: Joint Research Centre 2013.

[7] Ipcc, *Climate Change 2014: Impacts, Adaptation, and Vulnerability. Part A: Global and Sectoral Aspects. Contribution of Working Group II to the Fifth Assessment Report of the Intergovernmental Panel on Climate Change [Field, C.B., V.R. Barros, D.J. Dokken, K.J. Mach, M.D. Mastrandrea, T.E. Bilir, M. Chatterjee, K.L. Ebi, Y.O. Estrada, R.C. Genova, B. Girma, E.S. Kissel, A.N. Levy, S. MacCracken, P.R. Mastrandrea, and L.L. White (eds.)]*. Cambridge, United Kingdom and New York, NY, USA: Cambridge University Press, 2014.

[8] A. M. Omer, "Energy, environment and sustainable development," *Renewable and Sustainable Energy Reviews*, vol. 12, pp. 2265-2300, 12 2008.

[9] IEA, *Solar Energy Perspectives*: OECD Publishing, 2011.

[10] "Fraunhofer Institute for Solar Energy Systems (ISE), "Photovoltaics Report"," 2014.

[11] "Interanational Technology Roadmap for Photovoltaics (ITRPV)," 2015.

[12] "International Technology Roadmap for Photovoltaics (ITRPV) Results for 2012," 2013.

[13] "REN21. 2014 Renewables 2014 Global Status Report."

[14] *The Silver Institute,* Available: *https://www.silverinstitute.org/site/2014/12/10/silver-demand-for-industrial-applications-forecast-to-reach-nearly-680-million-ounces-in-2018/*.

[15] Available: *http://silverprice.org/*. 16, May 2015.

[16] E. C. Campos, "Screen printed Ag contacting interface in industrial crystalline silicon solar cells," PhD, University of Konstanz, 2013.

[17] J. Bartsch, "Advanced front side metallization for crystalline silicon solar cells with electrochemical techniques," PhD, Albert-Ludwigs University, 2011.

[18] A. Kraft, C. Wolf, J. Bartsch, and M. Glatthaar, "Characterization of Copper Diffusion in Silicon Solar Cells," *Energy Procedia*, vol. 67, pp. 93-100, 4 2015.

[19] S. M. Sze, *Semiconductor devices, physics and technology*: Wiley, 1985.

[20] K. R. Mcintosh, "Lumps, Humps, and Bumps: Three detrimental effects in the current-voltage characteristics of silicon solar cells," PhD, University of New South Wales, Sydney, Australia, 2001.

[21] A. Mette, "New concepts for front side metallisation of industrial silicon solar cells," PhD, Fraunhofer Institute for Solar Energy Systems, University of Freiburg, Freiburg, 2007.

[22] (23 June 2015). *PVCDROM, Standard solar cell spectra*. Available: http://www.pveducation.org/pvcdrom/appendices/standard-solar-spectra

[23] M. A. Green, Solar cells : operating principles, technology, and system applications / Martin A. Green. Englewood Cliffs, N.J: Prentice-Hall, 1982.

[24] R. Honig, "Evaluation and microstructure analysis of thick film contacts for industrial silicon solar cells," PhD, Fraunhofer-Institute for Solar Energy Systems, University of Freibury, Freiburg, 2014.

[25] A. Richter, M. Hermle, and S. W. Glunz, "Reassessment of the Limiting Efficiency for Crystalline Silicon Solar Cells," *Photovoltaics, IEEE Journal of*, vol. 3, pp. 1184-1191, 2013.

[26] R. M. Swanson, "Approaching the 29% limit efficiency of silicon solar cells," in *Photovoltaic Specialists Conference, 2005. Conference Record of the Thirty-first IEEE*, 2005, pp. 889-894.

[27] M. A. Green, K. Emery, Y. Hishikawa, W. Warta, and E. D. Dunlop, "Solar cell efficiency tables (Version 45)," *Progress in photovoltaics: research and applications,* vol. 23, pp. 1-9, 2015.

[28] "Mono wafers to recapture share from multi in solar PV," 2014.

[29] "Modelling of Light Trapping in Acidic-Textured Multicrystalline Silicon Wafers," *International Journal of Photoenergy,* vol. 2012, 2012.

[30] P. Campbell and M. A. Green, "Light trapping properties of pyramidally textured surfaces," *Journal of Applied Physics,* vol. 62, pp. 243-249, 1987.

[31] D. L. King and M. E. Buck, "Experimental optimization of an anisotropic etching process for random texturization of silicon solar cells," in *Photovoltaic Specialists Conference, 1991., Conference Record of the Twenty Second IEEE,* 1991, pp. 303-308 vol.1.

[32] E. S. Marstein, H. J. Solheim, D. N. Wright, and A. Holt, "Acidic texturing of multicrystalline silicon wafers," in *Photovoltaic Specialists Conference, 2005. Conference Record of the Thirty-first IEEE,* 2005, pp. 1309-1312.

[33] R. Einhaus, E. Vazsonyi, J. Szlufcik, J. Nijs, and R. Mertens, "Isotropic texturing of multicrystalline silicon wafers with acidic texturing solutions [solar cell manufacture]," in *Photovoltaic Specialists Conference, 1997., Conference Record of the Twenty-Sixth IEEE,* 1997, pp. 167-170.

[34] W. Kern, "The Evolution of Silicon Wafer Cleaning Technology," *Journal of The Electrochemical Society,* vol. 137, pp. 1887-1892, June 1,1990.

[35] A. Bentzen, "Phosphorus diffusion and gettering in silicon solar cells," PhD, Department of Physics, University of Oslo, Oslo, Norway, 2006.

[36] V. Shanmugam, J. Cunnusamy, A. Khanna, P. K. Basu, Z. Yi, C. Chilong*, et al.*, "Electrical and Microstructural Analysis of Contact Formation on Lightly Doped Phosphorus Emitters Using Thick-Film Ag Screen Printing Pastes," *Photovoltaics, IEEE Journal of,* vol. 4, pp. 168-174, 2014.

[37] T. Ambridge and M. M. Faktor, "An automatic carrier concentration profile plotter using an electrochemical technique," *Journal of Applied Electrochemistry,* vol. 5, pp. 319-328, 1975/11/01 1975.

[38] P. K. Basu, F. Law, S. Vinodh, A. Kumar, P. Richter, F. Bottari, *et al.*, "0.4% absolute efficiency increase for inline-diffused screen-printed multicrystalline silicon wafer solar cells by non-acidic deep emitter etch-back," *Solar Energy Materials and Solar Cells,* vol. 137, pp. 193-201, 6 2015.

[39] S. Duttagupta, "Advanced surface passivation of crystalline silicon for solar cell applications," PhD, Department of Electrical and Computer Engineering, National University of Singapore, Singapore, 2014.

[40] A. G. Aberle, "Surface passivation of crystalline silicon solar cells: a review," *Progress in Photovoltaics: Research and Applications,* vol. 8, pp. 473-487, 2000.

[41] P. J. Richter, F. J. Bottari, and D. C. Wong, "Rapid metallization paste firing of crystalline silicon solar cells," in *Photovoltaic Specialists Conference (PVSC), 2011 37th IEEE*, 2011, pp. 002198-002201.

[42] M. Hörteis, T. Gutberlet, A. Reller, and S. W. Glunz, "High-Temperature Contact Formation on n-Type Silicon: Basic Reactions and Contact Model for Seed-Layer Contacts," *Advanced Functional Materials,* vol. 20, pp. 476-484, 2010.

[43] V. Meemongkolkiat, K. Nakayashiki, D. S. Kim, R. Kopecek, and A. Rohatgi, "Factors Limiting the Formation of Uniform and Thick Aluminum–Back-Surface Field and Its Potential," *Journal of The Electrochemical Society,* vol. 153, pp. G53-G58, January 1, 2006.

[44] V. Shanmugam, J. Cunnusamy, A. Khanna, M. B. Boreland, and T. Mueller, "Optimisation of Screen-Printed Metallisation for Industrial High-Efficiency Silicon Wafer Solar Cells," *Energy Procedia,* vol. 33, pp. 64-69, 2013.

[45] T. Kwon, S. Kim, D. Kyung, W. Jung, S. Kim, Y. Lee, *et al.*, "The effect of firing temperature profiles for the high efficiency of crystalline Si solar cells," *Solar energy materials and solar cells,* vol. 94, pp. 823-829, 2010.

[46] D. E. Kane and R. M. Swanson, "Measurement of the emitter saturation current by a contactless photoconductivity decay method," in *IEEE Photovoltaic Specialists Conference*, 1985.

[47] V. Velidandla, B. Garland, and F. Cheung, "Automated process metrology in solar cell manufacturing," in *Photovoltaic Specialists Conference (PVSC), 2012 38th IEEE*, 2012, pp. 000489-000495.

[48] V. Shanmugam, J. Wong, I. M. Peters, J. Cunnusamy, M. Zahn, A. Zhou, *et al.*, "Analysis of Fine-Line Screen and Stencil-Printed Metal Contacts for Silicon Wafer Solar Cells," *Photovoltaics, IEEE Journal of*, vol. 5, pp. 525-533, 2015.

[49] D. K. Schroder, *Semiconductor material and device characterization*: John Wiley & Sons, 2006.

[50] G. Reeves, "Specific contact resistance using a circular transmission line model," *Solid-State Electronics,* vol. 23, pp. 487-490, 1980.

[51] L. Mak, C. Rogers, and D. Northrop, "Specific contact resistance measurements on semiconductors," *Journal of Physics E: Scientific Instruments,* vol. 22, p. 317, 1989.

[52] K. D. Vernon-Parry, "Scanning electron microscopy: an introduction," *III-Vs Review,* vol. 13, pp. 40-44, 2000.

[53] T. Suganuma, "Measurement of surface topography using SEM with two secondary electron detectors," *Journal of electron microscopy,* vol. 34, pp. 328-337, 1985.

[54] C. Lap Kin, L. Liang, and Z. Li, "Nano-Ag colloids assisted tunneling mechanism for current conduction in front contact of crystalline Si solar cells," in *Photovoltaic Specialists Conference (PVSC), 2009 34th IEEE*, 2009, pp. 002344-002348.

[55] G. Schubert, F. Huster, and P. Fath, "Physical understanding of printed thick-film front contacts of crystalline Si solar cells - Review of existing models and recent developments," *Solar energy materials and solar cells*, vol. 90, pp. 3399-3406, 2006.

[56] M. M. Hilali, "Understanding and development of manufacturable screen-printed contacts on high sheet-resistance emitters for low-cost silicon solar cells," Georgia Institute of Technology, 2005.

[57] E. Cabrera, S. Olibet, J. Glatz-Reichenbach, R. Kopecek, D. Reinke, and G. Schubert, "Experimental evidence of direct contact formation for the current transport in silver thick film metallized silicon emitters," *Journal of Applied Physics,* vol. 110, p. 114511, 2011.

[58] A. Aberle, S. Wenham, and M. Green, "A new method for accurate measurements of the lumped series resistance of solar cells," in *Photovoltaic Specialists Conference, 1993., Conference Record of the Twenty Third IEEE*, 1993, pp. 133-139.

[59] B. Thaidigsmann, A. Wolf, and D. Biro, "Accurate determination of the IQE of screen printed silicon solar cells by accounting for the finite reflectance of metal contacts," in *Proceedings of the 24th European Photovoltaic Solar Energy Conference*, 2009, pp. 2056-2059.

[60] B. Fischer, M. Keil, P. Fath, and E. Bucher, "Scanning IQE-measurement for accurate current determination on very large area solar cells," in *Photovoltaic Specialists Conference, 2002. Conference Record of the Twenty-Ninth IEEE*, 2002, pp. 454-457.

[61] R. Sinton and A. Cuevas, "A quasi-steady-state open-circuit voltage method for solar cell characterization," in *Proceedings of the 16th European Photovoltaic Solar Energy Conference*, 2000.

[62] P. Würfel, T. Trupke, T. Puzzer, E. Schäffer, W. Warta, and S. Glunz, "Diffusion lengths of silicon solar cells from luminescence images," *Journal of Applied Physics,* vol. 101, p. 123110, 2007.

[63] J. Giesecke, M. Schubert, B. Michl, F. Schindler, and W. Warta, "Minority carrier lifetime imaging of silicon wafers calibrated by quasi-steady-state photoluminescence," *Solar Energy Materials and Solar Cells,* vol. 95, pp. 1011-1018, 2011.

[64] M. Glatthaar, J. Haunschild, R. Zeidler, M. Demant, J. Greulich, B. Michl*, et al.*, "Evaluating luminescence based voltage images of silicon solar cells," *Journal of Applied Physics,* vol. 108, p. 014501, 2010.

[65] T. Trupke, E. Pink, R. Bardos, and M. Abbott, "Spatially resolved series resistance of silicon solar cells obtained from luminescence imaging," *Applied Physics Letters,* vol. 90, p. 093506, 2007.

[66] M. Glatthaar, J. Haunschild, M. Kasemann, J. Giesecke, W. Warta, and S. Rein, "Spatially resolved determination of dark saturation current and series resistance of silicon solar cells," *physica status solidi (RRL)-Rapid Research Letters,* vol. 4, pp. 13-15, 2010.

[67] V. Shanmugam, T. Mueller, A. G. Aberle, and J. Wong, "Determination of metal contact recombination parameters for silicon wafer solar cells by photoluminescence imaging," *Solar Energy*, vol. 118, pp. 20-27, 2015.

[68] E. H. Rhoderick and R. Williams, *Metal-semiconductor contacts*: Clarendon Press Oxford, 1988.

[69] M. Hörteis, "Fine-line printed contacts on Silicon Solar Cells," PhD Thesis, University of Konstanz, 2009.

[70] W. Schottky, "Semiconductor theory of the blocking layer (in German, original title : Halbleitertheorie der sperrschicht)," *Naturwissenschaften*, vol. 26, pp. 843-843, 1938.

[71] N. Mott, "Note on the contact between a metal and an insulator or semi-conductor," in *Mathematical Proceedings of the Cambridge Philosophical Society*, 1938, pp. 568-572.

[72] J. Bardeen, "Surface states and rectification at a metal semi-conductor contact," in *Electronic Structure of Metal-Semiconductor Contacts*, ed: Springer, 1990, pp. 63-73.

[73] S. M. Sze and K. K. Ng, *Physics of semiconductor devices*: John Wiley & Sons, 2006.

[74] H. A. Bethe, *Theory of the boundary layer of crystal rectifiers*: Radiation Laboratory, Massachusetts Institute of Technology, 1942.

[75] E. Cabrera Campos, "Screen Printed Silver Contacting Interface in Industrial Crystalline Silicon Solar Cells," PhD, University of Konstanz, 2013.

[76] G. Schubert, "Thick film metallisation of crystalline silicon solar cells: Mechanisms, models and applications," PhD, University of Konstanz 2006.

[77] A. Yu, "Electron tunneling and contact resistance of metal-silicon contact barriers," *Solid-State Electronics*, vol. 13, pp. 239-247, 1970.

[78] F. Padovani and R. Stratton, "Field and thermionic-field emission in Schottky barriers," *Solid-State Electronics*, vol. 9, pp. 695-707, 1966.

[79] A. W. Blakers, A. Wang, A. M. Milne, J. Zhao, and M. A. Green, "22.8% efficient silicon solar cell," *Applied Physics Letters*, vol. 55, pp. 1363-1365, 1989.

[80] J. Bartsch, A. Mondon, K. Bayer, C. Schetter, M. Hörteis, and S. Glunz, "Quick determination of copper-metallization long-term impact on silicon solar cells," *Journal of the electrochemical Society*, vol. 157, pp. H942-H946, 2010.

[81] D. Erath, "Printing techniques in the *c-Si* PV industry-a brief technological overview," *International Circular of Graphic Education and Research*, vol. 3, pp. 8-15, 2010.

[82] M. Field and L. Scudder, "Application of thick-film technology to solar cell fabrication," in *12th Photovoltaic Specialists Conference*, 1976, pp. 303-308.

[83] L. Frisson, P. Lauwers, P. Bulteel, L. De Smet, R. Mertens, R. Govaerts, *et al.*, "Screen printed contacts on silicon solar cells with low series resistance," in *13th Photovoltaic Specialists Conference*, 1978, pp. 590-592.

[84] J. Hoornstra and B. Heurtault, "Stencil print applications and progress for crystalline silicon solar cells," in *Conference Proceedings, 24th EPSEC*, 2009, pp. 989-992.

[85] M. B. Edwards, "Screen and Stencil print technologies for industrial n-type si solar cells," PhD, Centre for photovoltaic engineering, University of New South Wales, Australia, 2008.

[86] E. Van Kerschaver, P. Choulat, and J. Szlufcik, "Stable and Reliable Metallisation by Application of Electro-formed Ni Stencils," in *Proceedings of the 16th European Photovoltaic Solar Energy Conference, Glasgow, UK*, 2000, pp. 1528-1531.

[87] D. Stüwe, D. Mager, D. Biro, and J. G. Korvink, "Inkjet Technology for Crystalline Silicon Photovoltaics," *Advanced Materials*, vol. 27, pp. 599-626, 2015.

[88] K. Teng and R. Vest, "Application of ink jet technology on photovoltaic metallization," *Electron Device Letters, IEEE*, vol. 9, pp. 591-593, 1988.

[89] J. Heinzl and C. Hertz, "Ink-jet printing," *Advances in electronics and electron physics*, vol. 65, pp. 91-171, 1985.

[90] A. Ebong, B. Rounsaville, I. Cooper, K. Tate, A. Rohatgi, S. Glunz, *et al.*, "High efficiency silicon solar cells with ink jetted seed and plated grid on high sheet resistance emitter," in *Photovoltaic Specialists Conference (PVSC), 2010 35th IEEE*, 2010, pp. 001363-001367.

[91] R. Jesswein, "Process Optimization of Single Step Inkjet Printed Front Contacts for Industrially Fabricated Solar Cells Leads to an Efficiency Gain of 0.3% abs with Consumption of Less Than 60mg Silver," *Proc. of the 28th EUPVSEC, Paris,* pp. 997-1003, 2013.

[92] X. Lin, J. Kavalakkatt, M. C. Lux-Steiner, and A. Ennaoui, "Inkjet-Printed Cu2ZnSn(S, Se)4 Solar Cells," *Advanced Science,* vol. 2, 2015.

[93] V. Zöllmer, M. Müller, M. Renn, M. Busse, I. Wirth, D. Godlinski*, et al.*, "Printing with aerosols," *European coatings journal,* vol. 7, p. 46, 2006.

[94] J. W. Sears and J. Colvin, "Applying Nanoparticles via Direct-write Technology for Industrial Applications," *Advances in powder metallurgy and particulate materials,* vol. 1, p. 3, 2005.

[95] A. Lorenz, A. Senne, J. Rohde, S. Kroh, M. Wittenberg, K. Krüger*, et al.*, "Evaluation of Flexographic Printing Technology for Multi-busbar Solar Cells," *Energy Procedia,* vol. 67, pp. 126-137, 4 2015.

[96] M. Frey, F. Clement, S. Dilfer, D. Erath, and D. Biro, "Front-side metalization by means of flexographic printing," *Energy Procedia,* vol. 8, pp. 581-586, 2011.

[97] P. Hahne, E. Hirth, I. E. Reis, K. Schwichtenberg, W. Richtering, F. M. Horn*, et al.*, "Progress in thick-film pad printing technique for solar cells," *Solar energy materials and solar cells,* vol. 65, pp. 399-407, 2001.

[98] Frank Kleine Jager, Xuerong Gao, Stephan Hermes, Thomas Sauter, H. Higgen, C. Buchner*, et al.*, "BASF's Cyposol metallisation inks for newly developed Laser Transfer Printing technology," 2010.

[99] J. Lossen, M. Matusovsky, A. Noy, C. Maier, and M. Bähr, "Pattern Transfer Printing (PTPTM) for *c-Si* Solar Cell Metallization," *Energy Procedia*, vol. 67, pp. 156-162, 4// 2015.

[100] L. Mai, "Overcoming the performance and limitations of commercial screen-printed solar cells," PhD, University of New South Wales (UNSW), 2010.

[101] T. Falcon and S. Clasper, "Ultra fine line print process development for silicon solar cell metalisation," in *Microelectronics and Packaging Conference (EMPC), 2011 18th European*, 2011, pp. 1-5.

[102] M. Kamp, J. Bartsch, S. Nold, M. Retzlaff, M. Hörteis, and S. W. Glunz, "Economic Evaluation of Two-Step Metallization Processes for Silicon Solar Cells," *Energy Procedia,* vol. 8, pp. 558-564, 2011.

[103] H. Hannebauer, T. Dullweber, T. Falcon, X. Chen, and R. Brendel, "Record Low Ag Paste Consumption of 67.7 mg with Dual Print," *Energy Procedia,* vol. 43, pp. 66-71, 2013.

[104] M. Kšnig, M. Deckelmann, A. Henning, R. Hoenig, F. Clement, and M. Hšrteis, "Dual Screen Printing Featuring Novel Framed Busbar Screen Layout and Non-Contacting Ag Busbar Paste," *Energy Procedia,* vol. 27, pp. 510-515, 2012.

[105] B. H. J.Hoornstr, "Stencil print applications and progress for crystalline silicon solar cells," in *24th European Photovoltaic Solar Energy Conference*, Hanburg, Germany, 2009.

[106] M. B. Edwards, "Screen and Stencil print technologies for industrial N-type silicon solar cells," PhD, University of New South Wales, 2008.

[107] B. E. Jiménez Cisneros, T. Oki, N. W. Arnell, G. Benito, J. G. Cogley, P. Döll*, et al.*, "Freshwater resources," in *Climate Change 2014: Impacts, Adaptation, and Vulnerability. Part A: Global and Sectoral Aspects. Contribution of Working Group II to the Fifth Assessment Report of the Intergovernmental Panel of Climate Change*, C. B. Field, V. R. Barros, D. J. Dokken, K. J. Mach, M. D. Mastrandrea, T. E. Bilir*, et al.*, Eds., ed Cambridge, United Kingdom and New York, NY, USA: Cambridge University Press, 2014, pp. 229-269.

[108] A. Mette, "New concepts for front side metallisation of industrial silicon solar cells," PhD, Albert Ludwigs University, Freiburg, Germany, 2007.

[109] J. Lin, Z. Weiming, T. Guo, D. Kapp, Y. Li, and L. Wang, "An improved mathematical modeling to simulate metallization screen pattern trend for silicon solar cell," in *Photovoltaic Specialists Conference (PVSC), 2013 IEEE 39th*, 2013, pp. 2641-2645.

[110] J. Wong, "Griddler: Intelligent computer aided design of complex solar cell metallization patterns," in *Photovoltaic Specialists Conference (PVSC), 2013 IEEE 39th*, 2013, pp. 0933-0938.

[111] M. H. Kalos and P. A. Whitlock, *Monte carlo methods*: John Wiley & Sons, 2008.

[112] A. Pierpaolo and M. Bill, "Beyond Gaussian averages: redirecting international business and management research toward extreme events and power laws," *Journal of International Business Studies,* vol. 38, pp. 1212-1230, 2007.

[113] M. A. Green, *Solar cells: operating principles, technology and system applications*. Kensington: UNSW, 1998.

[114] A. W. Blakers, "Shading losses of solar‐cell metal grids," *Journal of Applied Physics,* vol. 71, pp. 5237-5241, 1992.

[115] R. Woehl, M. rteis, and S. W. Glunz, "Analysis of the Optical Properties of Screen-Printed and Aerosol-Printed and Plated Fingers of Silicon Solar Cells," *Advances in OptoElectronics,* vol. 2008, 2008.

[116] M. J. Kerr and A. Cuevas, "General parameterization of Auger recombination in crystalline silicon," *Journal of Applied Physics,* vol. 91, pp. 2473-2480, 2002.

[117] A. Cuevas and D. A. Russell, "Co-optimisation of the emitter region and the metal grid of silicon solar cells," *Progress in Photovoltaics: Research and Applications,* vol. 8, pp. 603-616, 2000.

[118] R. King, R. Sinton, and R. Swanson, "Studies of diffused phosphorus emitters: saturation current, surface recombination velocity, and quantum efficiency," *Electron Devices, IEEE Transactions on,* vol. 37, pp. 365-371, 1990.

[119] P. Vinod, "Specific contact resistance and carrier tunneling properties of the silver metal/porous silicon/p-Si ohmic contact structure," *Journal of Alloys and Compounds,* vol. 470, pp. 393-396, 2009.

[120] R. Mertens, G. Cheek, M. Eyckmans, L. Frisson, M. Honore, and B. Van Overstraeten, "Critical processing parameter optimization for screen printed semicrystalline silicon solar cells," in *Conf. Rec. IEEE Photovoltaic Spec. Conf.;(United States)*, 1984.

[121] M. M. Hilali, S. Sridharan, C. Khadilkar, A. Shaikh, A. Rohatgi, and S. Kim, "Effect of glass frit chemistry on the physical and electrical properties of thick-film Ag contacts for silicon solar cells," *Journal of electronic materials,* vol. 35, pp. 2041-2047, 2006.

[122] G. C. Cheek, R. P. Mertens, R. Van Overstraeten, and L. Frisson, "Thick-film metallization for solar cell applications," *Electron Devices, IEEE Transactions on,* vol. 31, pp. 602-609, 1984.

[123] C. Ballif, D. Huljić, G. Willeke, and A. Hessler-Wyser, "Silver thick-film contacts on highly doped n-type silicon emitters: structural and electronic properties of the interface," *Applied physics letters,* vol. 82, pp. 1878-1880, 2003.

[124] Z. Li, L. Liang, A. Ionkin, B. Fish, M. Lewittes, L. Cheng, *et al.*, "Microstructural comparison of silicon solar cells' front-side Ag contact and the evolution of current conduction mechanisms," *Journal of Applied Physics,* vol. 110, p. 074304, 2011.

[125] G. Schubert, J. Horzel, R. Kopecek, F. Huster, and P. Fath, "Silver thick film contact formation on lowly doped phosphorous emitters," in *20th European Photovoltaic Solar Energy Conference*, Barcelona, Spain, 2005, pp. 934-937.

[126] P. K. Basu, D. Sarangi, K. D. Shetty, and M. B. Boreland, "Liquid silicate additive for alkaline texturing of mono-Si wafers to improve process bath lifetime and reduce IPA consumption," *Solar Energy Materials and Solar Cells,* vol. 113, pp. 37-43, 2013.

[127] P. Basu, M. Boreland, S. Vinodh, and D. Sarangi, "Non-acidic isotropic etch-back method for silicon wafer solar cells," *US Provisional Application No.: 61,* vol. 644730, 2012.

[128] M. J. Kerr, A. Cuevas, and R. A. Sinton, "Generalized analysis of quasi-steady-state and transient decay open circuit voltage measurements," *Journal of applied physics,* vol. 91, pp. 399-404, 2002.

[129] D. Kane and R. Swanson, "Measurement of the emitter saturation current by a contactless photoconductivity decay method," in *IEEE photovoltaic specialists conference. 18*, 1985, pp. 578-583.

[130] M. M. Hilali, A. Rohatgi, and B. To, "A review and understanding of screen-printed contacts and selective-emitter formation," in *14th workshop on crystalline silicon solar cells and modules*, 2004, pp. 80401-3393.

[131] G. Grupp, D. Huljic, R. Preu, G. Willeke, and J. Luther, "Peak firing temperature dependence of the microstructure of Ag thick-film contacts on silicon solar cells–a detailed AFM study of the interface," *Proc. 20th EC PVSEC,* 2005.

[132] D. K. Schroder and D. L. Meier, "Solar cell contact resistance—a review," *Electron Devices, IEEE Transactions on,* vol. 31, pp. 637-647, 1984.

[133] R. Hoenig, A. Kalio, J. Sigwarth, F. Clement, M. Glatthaar, J. Wilde, *et al.*, "Impact of screen printing silver paste components on the space charge region recombination losses of industrial silicon solar cells," *Solar Energy Materials and Solar Cells,* vol. 106, pp. 7-10, 2012.

[134] A. Khanna, T. Mueller, R. Stangl, B. Hoex, P. K. Basu, and A. G. Aberle, "A fill factor loss analysis method for silicon wafer solar cells," *Photovoltaics, IEEE Journal of,* vol. 3, pp. 1170-1177, 2013.

[135] M. A. Green, "Accuracy of analytical expressions for solar cell fill factors," *Solar Cells,* vol. 7, pp. 337-340, 1982.

[136] C. Ballif, D. M. Huljić, G. Willeke, and A. Hessler-Wyser, "Silver thick-film contacts on highly doped n-type silicon emitters: Structural and electronic properties of the interface," *Applied Physics Letters,* vol. 82, p. 1878, 2003.

[137] I. B. Cooper, K. Tate, J. S. Renshaw, A. F. Carroll, K. R. Mikeska, R. C. Reedy, *et al.*, "Investigation of the mechanism resulting in low resistance Ag thick-film contact to Si solar cells in the context of emitter doping density and contact firing for current-generation Ag paste," *Photovoltaics, IEEE Journal of,* vol. 4, pp. 134-141, 2014.

[138] T. Fellmeth, A. Born, A. Kimmerle, F. Clement, D. Biro, and R. Preu, "Recombination at metal-emitter interfaces of front contact technologies for highly efficient silicon solar cells," *Energy Procedia,* vol. 8, pp. 115-121, 2011.

[139] R. Hoenig, M. Glatthaar, F. Clement, J. Greulich, J. Wilde, and D. Biro, "New measurement method for the investigation of space charge region recombination losses induced by the metallization of silicon solar cells," *Energy Procedia,* vol. 8, pp. 694-699, 2011.

[140] A. Edler, V. D. Mihailetchi, L. J. Koduvelikulathu, C. Comparotto, R. Kopecek, and R. Harney, "Metallization–induced recombination losses of bifacial silicon solar cells," *Progress in Photovoltaics: Research and Applications,* 2014.

[141] M. S. Helge Hannebauer, Jens Muller, Thorsten Dullweber, and Rolf Brendel, "Analysis of the emitter saturation current density of industrial type silver screen-printed front contacts," in *27th European Photovoltaic Solar Energy Conferency,* Frankfurt, Germany, 2012.

[142] T. Trupke, R. Bardos, M. Schubert, and W. Warta, "Photoluminescence imaging of silicon wafers," *Applied Physics Letters,* vol. 89, p. 044107, 2006.

[143] C. Shen, H. Kampwerth, M. Green, T. Trupke, J. Carstensen, and A. Schütt, "Spatially resolved photoluminescence imaging of essential silicon solar cell parameters and comparison with CELLO measurements," *Solar Energy Materials and Solar Cells,* vol. 109, pp. 77-81, 2013.

[144] H. Höffler, H. Al-Mohtaseb, N. Wöhrle, B. Michl, M. Kasemann, and J. Haunschild, "Spatially Resolved Determination of Junction Voltage of Silicon Solar Cells," *Energy Procedia,* vol. 55, pp. 85-93, 2014.

[145] Z. Hameiri and P. Chaturvedi, "Spatially resolved electrical parameters of silicon wafers and solar cells by contactless photoluminescence imaging," *Applied Physics Letters,* vol. 102, pp. 073502-073502-3, 2013.

[146] A. Edler, V. D. Mihailetchi, L. J. Koduvelikulathu, C. Comparotto, R. Kopecek, and R. Harney, "Metallization–induced recombination losses of bifacial silicon solar cells," *Progress in Photovoltaics: Research and Applications,* vol. 23, pp. 620-627, 2015.

[147] J. Wong, R. Sridharan, and V. Shanmugam, "Quantifying edge and peripheral recombination in industrial solar cells," *IEEE Transactions on Electron Devices,* 2015.

Publications arising from this work

The following papers were generated in the course of the research activities described in this thesis.

Journal publications

1. **V. Shanmugam**, J. Cunnusamy, A. Khanna, P.K. Basu, Y. Zhang, C. Chilong, A. Stassen, M.B. Boreland, B. Hoex, T. Mueller and A.G. Aberle, "Electrical and Microstructural analysis of the contact formation on lightly doped phosphorus emitters using thick film Ag screen printing pastes, IEEE Journal of Photovoltaics, volume 4, Issue 1, Jan (2014).

2. **V. Shanmugam**, J.K. Wong, J. Cunnusamy, M. Zahn, A. Zhou, R. Yang, X. Chen, T. Mueller and A.G. Aberle. "Analysis of fine line screen-printed and stencil-printed Ag metal contacts for silicon wafer solar cells", IEEE Journal of Photovoltaics, volume 5, Issue 2, Mar (2015)**.**

3. **V. Shanmugam**, T. Mueller, A.G. Aberle and J.K. Wong, "Determination of metal contact recombination parameters for silicon wafer solar cells by photoluminescence imaging", Solar Energy, Volume 118, pp 20-27, May (2015).

4. **V. Shanmugam,** A. Khanna, P.K. Basu, A.G. Aberle, T. Mueller and J.K. Wong, "Impact of phosphorus emitter doping profile on the metal contact recombination for silicon wafer solar cells", Solar Energy Materials and Solar cells, Volume 147, pp 171-176, Apr (2016).

5. A. Khanna, P.K. Basu, A. Filipovic, **V. Shanmugam**, C. Schmiga, A.G. Aberle, T. Mueller, “Influence of pyramidal surface texture height and uniformity on screen printed contact formation”, Solar Energy Materials & Solar Cells, volume 132, pp 589-596, (2015).

6. P.K. Basu, F. Law, **V. Shanmugam**, P. Bottari, F. Richter and B. Hoex, “0.4% absolute efficiency increase for inline diffused screen printed multi crystalline silicon wafer solar cells by non- acidic deep emitter etch back”, Solar Energy Materials and Solar Cells, volume 137, pp 193-201 (2015).

7. J.K. Wong, **V. Shanmugam**, J. Cunnusamy, M. Zahn, A. Zhou, R. Yang, X. Chen, T. Mueller and A.G. Aberle, “Influence of non-uniform fine lines in silicon solar cell front metal grid design, “Progress in Photovoltaics, June (2015), DOI:10.1002/pip.2636”.

8. L. Zhe, IM Peters, **V. Shanmugam,** Y.S. Khoo, S. Guo, R. Stangl, A.G. Aberle, and J.K. Wong, “Luminescence imaging analysis of light harvesting from inactive area in crystalline silicon PV modules”, Submitted to Solar Energy Materials and Solar Cells.

9. J.K. Wong, R. Sridharan, **V. Shanmugam**, “Quantifying Edge and peripheral recombination in industrial silicon solar cells”, Submitted to IEEE Transactions on Electron Devices.

10. P.K. Basu, Joel Li, **V. Shanmugam**, A. Khanna, “Efficiency improvement by phosphorus gettering for multicrystalline silicon wafer solar cells involving heavy diffusion and non-acidic etch-back”, Submitted to Solar Energy Journal

11. K.D. Shetty, M.B. Boreland, **V. Shanmugam**, B. Hoex, "Optimization of $POCl_3$ diffused emitters for high efficiency silicon wafer solar cells", Accepted for publication in International Journal of Photoenergy.

Conference proceedings and Workshop presentations

1. **V. Shanmugam**, J. Cunnusamy, A. Khanna, M.B. Boreland, and T. Mueller, “Optimisation of screen printed metallisation for industrial high efficiency silicon wafer solar cells”, Energy Procedia, volume 33, pp 64-69 (2013).

2. **V. Shanmugam**, J.K. Wong, J. Cunnusamy, M. Zahn, A. Zhou, R. Yang, X. Chen, T. Mueller and A.G. Aberle, “Investigation of fine line screen-printed and stencil-printed Ag metal contacts for silicon wafer solar cells”, WCPEC-06, Kyoto, Japan, Nov (2014).

3. **V. Shanmugam**, J.K. Wong, T. Mueller, and A.G. Aberle, “Overcoming the performance limitations of fine-line screen and stencil printed metal contacts for silicon wafer solar cells”, presented in PV Asia Scientific Conference, Singapore, Oct (2014).

4. **V. Shanmugam**, A.K. Khanna, T. Mueller, J.K. Wong and A.G. Aberle, “Screen printed Ag metallisation induced recombination losses in silicon wafer solar cells”, to be presented in PV Asia Scientific Conference (Oral presentation), Singapore Oct (2015).

5. K.D. Shetty, M.B. Boreland, **V. Shanmugam**, J. Cunnusamy, C.K. Wu, S. Iggo, H. Antoniadis, “Lightly doped emitters for high efficiency silicon wafer solar cells”, Energy Procedia, volume 33, pp 70-75 (2013).

6. A. Khanna, Z.P. Ling, **V. Shanmugam**, M.B. Boreland, I. Hayashi, D.J. Kirk, H. Akimoto, A.G. Aberle, T. Mueller, “Screen printed metallisation for a-Si:H/*c-Si* Heterojunction cells”, 28th EUPVSEC (2013).

7. L. Zhe, I.M. Peters, Y.S. Khoo, **V. Shanmugam**, R. Stangl, A.G. Aberle, and J.K. Wong, "Luminescence imagining analysis of light trapping in PV modules", To be submitted to EUPVSEC 2015.

8. J.K. Wong, **V. Shanmugam**, "Finite Element Model analysis of solar cell luminescence images", 42nd IEEE Photovoltaic Scientific Conference, July 2015.

Patents

1. P.K. Basu, M.B. Boreland, **V. Shanmugam** and D. Sarangi, "Non-acidic isotropic etch-back method for silicon wafer solar cells", US Patent Application US2015/0044812 A1, Feb 12, 2015.